

# Development of a high-order potential flow solver for nonlinear wave-structure interaction

Jacob Bjarke Hansen Hicks

PhD Thesis

# **Development of a potential flow solver including wave-structure interaction**

Jacob Bjarke Hansen Hicks

December 2020





## Summary (English)

Accurate modelling and evaluation of nonlinear wave loads on marine structures is of critical importance to ensure longevity in their designs. To that end, the focus of this research is the extension and subsequent application of a fully nonlinear, finite-difference based potential flow solver to nonlinear wave-structure interactions at high order. Both forced and free-body motions are considered.

The solver utilizes a sigma-transformation of the vertical coordinate, which maps the time-varying physical domain to a time-invariant computational domain. This is combined with an Immersed Boundary Method (IBM) based on Weighted Least Squares (WLS) stencils for satisfying the body boundary condition, which provides a sharp-interface method for including moving bodies in the domain. The time-stepping solution proceeds via an explicit, fourth-order Runge-Kutta scheme. The combination of an IBM with both a sigma-transformation and a multi-stage time-stepping method presents several difficulties, which are addressed in this research by the introduction of body-free-surface intersection point tracking and an acceleration potential method for the evaluation of wave loads. These improvements eliminate the spurious oscillations in the calculated force signals, reported in previous work and thought to be related to the IBM, and are implemented at flexible order. Initial testing of free-body motions indicates a weak numerical instability related to the implicit body boundary condition. However, application of a high-order filter to the free-surface variables appears to mitigate this, and allows for favourable comparison with experimental data for the free decay of a circular cylinder.

An optimization procedure is developed for the generation of stable wave fields up to second order. While the procedure is applicable to wavemakers of arbitrary shape, in this work it is applied to a heaving wedge wavemaker. Results show a significant reduction in both mean error and variation across a given test section, for waves in intermediate and deep water and up to 50% of the theoretical breaking limit.

# Summary (Danish)

Nøjagtig modellering og evaluering af ikke-lineære bølgebelastninger på maritime objekter er af afgørende betydning for et design der kan sikre lang levetid. Derfor er fokus for denne forskning en udvidelse og efterfølgende anvendelse af en fuldt ikke-lineær *finite-difference*-baseret løsningsmetode for strømningspotentialet ved ikke-lineære vekselvirkninger mellem bølger og objekter. Både tvungne og frie bevægelser undersøges.

Modellen anvender en sigmatransformation af den lodrette koordinat, som afbilder det tidsafhængige fysiske domæne på et tidsuafhængigt beregningsdomæne. Dette kombineres med en *Immersed Boundary Method* (IBM) baseret på *Weighted Least Squares* (WLS) stencils for at tilfredsstille grænsebetingelsen på legemet, hvilket giver en *sharp-interface*-metode til modellering af bevægede legemer i domænet. Løsningen integreres i tid via en eksplisit fjerde-ordens Runge-Kutta-metode. Kombinationen af en IBM med både en sigmatransformation og en flertrinsmetode til tidsintegration giver flere vanskeligheder. Disse adresseres i denne forskning ved introduktionen af et punkt, der følger skæringspunktet mellem legemet og den frie vandoverflade, samt løsningen af et grænseværdiproblem baseret på den tidsafledede af hastighedsportentialet. Det sidste giver en kobling mellem legemets og vandets bevægelser, og bruges som led i udregningen af bølgekræfter på flydende objekter. Disse forbedringer er implementeret ved fleksibel orden, og eliminerer uægte svingninger, rapporteret i tidligere arbejder, som menes at være relateret til brug af IBM. Indlendende test af frie bevægelser indikerer dog en svag numerisk ustabilitet relateret til løsning af det implicite grænseværdiproblem på legemets overflade. Dette afbødes ved brug af et højordensfilter på de frie overfladevariable, hvilket muliggør en god sammenligning med eksperimentielle data for det frie fald af en cirkulær cylinder.

En optimeringsprocedure er udviklet til generering af stabile bølgefelter op til anden orden. Proceduren kan anvendes på bølgegeneratorer af vilkårlig form, men anvendes i dette arbejde på en kileformet bølgegenerator, der kun bevæger sig i lodret retning. Resultaterne viser en signifikant reduktion i både den gennemsnitlige fejl og variationen hen over af et givent testområde, for bølger i middel- og dybt vand, samt med en hældning på op til 50% af den teoretiske bølgebrydningsgrænse.

# Preface

This thesis is submitted in partial fulfilment of the requirements for degree of Doctor of Philosophy at the Department of Mechanical Engineering, Technical University of Denmark.

The work has been carried out in the period between September 15th 2017 and December 14th 2020. The majority of the work has been carried out in the Section for Fluid Mechanics, Coastal and Maritime Engineering under the supervision of Professor Harry B. Bingham, Senior Researcher Robert Read, Associate Professor Allan P. Engsig-Karup, and Specialist Ole Lindberg. Part of the work has been carried out during a research visit of six months at the Department of Naval Architecture and Ocean Engineering, Osaka University, Japan, under the supervision of Professor Masashi Kashiwagi.

The financial support for this work was provided by the Danish Hydrocarbon Research and Technology Centre (DHRTC), as part of the Dynamics of Extreme Waves and their Interaction with Offshore Structures (DEWIOS) project.

Jacob Hicks

Lyngby, December 2020

# Acknowledgements

I would like to thank my principal supervisor Harry B. Bingham and co-supervisors Robert Read, Allan P. Engsig-Karup, and Ole Lindberg for their invaluable guidance throughout this project. Our meetings have been a constant source of inspiration, and their advice and encouragement has helped me navigate through the many challenges and frustrations that have arisen throughout this project. I would also like to thank Professor Masashi Kashiwagi for his hospitality during my research visit to Osaka University, and for sharing insights during our lab meetings.

I thank my fellow DEWIOS project members Jesper and Mathias for many interesting discussions and delicious cake-club meetings. I also thank Takahito Iida for his hospitality and advice during my research visit.

Finally, I thank Mathilde for her endless love and support, without which I could not have finished this work.

# Contents

## Summary (English)

Summary (Danish)	i
------------------	---

Preface	ii
---------	----

Acknowledgements	iii
------------------	-----

List of Figures	vi
-----------------	----

List of Tables	ix
----------------	----

List of Abbreviations	x
-----------------------	---

<b>1 Introduction</b>	<b>1</b>
-----------------------	----------

1.1 Background and motivation . . . . .	1
1.2 Research objectives and scientific contribution . . . . .	3

<b>2 Theoretical framework</b>	<b>7</b>
--------------------------------	----------

2.1 Governing equations . . . . .	7
2.2 Wavemaker theory . . . . .	9
2.3 Free-body motion . . . . .	12

<b>3 Numerical implementation</b>	<b>15</b>
-----------------------------------	-----------

3.1 Sigma-transform . . . . .	15
3.2 Finite-Difference Method . . . . .	16
3.3 Immersed Boundary Method . . . . .	16
3.4 Time integration . . . . .	18
3.5 Body-free-surface intersection point tracking . . . . .	19
3.6 Nonlinear wave loads and free-body motion . . . . .	29

<b>4 Stable waves of constant form using harmonic optimisation</b>	<b>40</b>
--	-----------

4.1 Solver validation . . . . .	40
4.2 Optimization procedure . . . . .	42

<b>5 Nonlinear wave-structure interaction</b>	<b>54</b>
---	-----------

5.1	Small-amplitude motion of a heaving cylinder . . . . .	54
5.2	Submerged surging dipole . . . . .	57
5.3	Cylinder at rest on the free surface . . . . .	59
5.4	Free-surface decay test . . . . .	60
<b>6</b>	<b>Summary and perspectives</b>	<b>65</b>
	<b>References</b>	<b>67</b>
<b>A</b>	<b>Appendix A - Matrix integration with permutation</b>	<b>81</b>
<b>B</b>	<b>Appendix B - Second-order transfer function</b>	<b>82</b>
<b>C</b>	<b>Appendix C - Numerical frameworks and techniques</b>	<b>83</b>
C.1	Numerical methods . . . . .	84
C.2	Interface capturing . . . . .	93

# List of Figures

2.1	General physical domain. Artificial interior free surface marked in red.	8
3.1	Point classification for the Immersed Boundary Method.	17
3.2	Updated point classification for the Immersed Boundary Method.	18
3.3	Free surface peeling away from body, caused when extrapolating a value for a new fluid point based on neighbouring fluid points.	20
3.4	Artificial interior free surface protruding from the body.	20
3.5	Normal distance from intersection point to piston wavemaker, for waves of varying steepness.	23
3.6	Comparison of free surface elevation after three wave periods, with and without the body-free-surface intersection point. The simulation case is a surging paddle wavemaker, with $kh = 2.27$ and $H/L = 0.06$ .	24
3.7	Comparison of wave generated by simple sinusoidal paddle motion, $kh = 2.64$ .	24
3.8	Schematic of numerical domain with piston wavemaker. Wavemaker marked in red.	25
3.9	Comparison of first- and second-order wave generation, for $kh = 2.03$ . Experimental values from Schäffer (1996).	26
3.10	Comparison of first- and second-order wave generation, for $kh = 1.41$ . Experimental values from Schäffer (1996).	27
3.11	Comparison of first- and second-order wave generation, for $kh = 0.95$ . Experimental values from Schäffer (1996).	27
3.12	Numerical domain for heaving cylinder simulations.	28
3.13	Normal distance from intersection point to heaving cylinder, for motion of increasing amplitude.	29
3.14	Random grid generation in 1D.	34
3.15	Convergence of integration by matrix-vector product in 1D for various stencil sizes, using random distribution of body points.	35
3.16	Convergence of integration by matrix-vector product in 1D for various stencil sizes, using uniform distribution of body points.	35
3.17	Convergence of integration by matrix-vector product in 2D, for various stencil sizes.	37
3.18	System matrix before and after modification for implicit integration.	38
3.19	Normal and tangential formulations for evaluating $\frac{\partial}{\partial n} \left( \frac{1}{2} (\nabla \phi)^2 \right)$ .	39
3.20	Convergence of $\frac{\partial}{\partial n} \left( \frac{1}{2} (\nabla \phi)^2 \right)$ .	39

4.1	The first-order transfer function of Wu (1988), as a function of the dimensionless wave number $kh$ . . . . .	41
4.2	Experimental setup for wedge wavemaker experiments. WG denotes wave gauge. . . . .	41
4.3	Relative mean errors before (above) and after (below) optimization. Arranged by wave steepness and coloured by dimensionless dispersion parameter $kh$ . . . . .	45
4.4	Amplitude variation across test section before (above) and after (below) optimization. Arranged by wave steepness and coloured by dimensionless dispersion parameter $kh$ . . . . .	46
4.5	Harmonic analysis of waves generated before and after amplitude optimization. . . . .	47
4.6	Relative Root Mean Square (RMS) error in numerical free surface elevation before (left) and after (right) optimization. Arranged by wave steepness and coloured by dimensionless dispersion parameter $kh$ . . . . .	47
4.7	Free surface elevation at various locations, with and without optimization. Target wave has dimensionless dispersion parameter $kh = 4.08$ and steepness $H/L = 6\%$ . . . . .	48
4.8	Relative mean error in first and second harmonics as function of second harmonic amplitude and phase, for waves of $kh = 2.33$ . . . . .	49
4.9	Maximum relative variation in first and second harmonics as function of second harmonic amplitude and phase, for waves of $kh = 2.33$ . . . . .	50
4.10	Relative mean error in first and second harmonics as function of second harmonic amplitude and phase, for waves of steepness $H/L = 4\%$ . . . . .	51
4.11	Maximum relative variation in first and second harmonics as function of second harmonic amplitude and phase, for waves of steepness $H/L = 4\%$ . . . . .	52
5.1	Gaussian movement profile and force response in shallow ( $h = 2R$ ) and deep ( $h = 6R$ ) water. . . . .	56
5.2	Comparison of numerical and analytical solutions for small-amplitude motion of a heaving cylinder. Vertical lines indicate limits of validity for shallow- and deep-water analytical solutions. . . . .	56
5.3	Comparison of calculated wave force on heaving circular cylinder, for water depth $h = 2R$ and nondimensional wave number $kR = 0.60$ . . . . .	58
5.4	Comparison of calculated wave force on heaving circular cylinder, for water depth $h = 2R$ and amplitude $A = 0.001R$ . . . . .	59
5.5	Convergence of explicit operators. . . . .	60
5.6	Convergence of horizontal and vertical velocities for a cylinder at rest on a quiescent free surface. . . . .	61
5.7	Time evolution of cylinder position, for a cylinder initially at rest on a quiescent free surface. . . . .	62
5.8	Time evolution of cylinder position over many periods, for a cylinder initially at rest on a quiescent free surface. Stencil size is $r = 7$ . . . . .	63
5.9	Time evolution of cylinder position over many periods, with a high-order Savitzky-Golay filter applied every time step. Stencil size is $r = 7$ . . . . .	63
5.10	Free decay of a circular cylinder for various stencil sizes. . . . .	64
C.1	Typical two-dimensional finite element mesh Sayma (2013). . . . .	85

C.2	Algorithm of original MPS method (Koshizuka et al. (1998)) . . . . .	91
C.3	Definition of quantities used in defining free surface pressure boundary condition (Hirt and Nichols (1981)). . . . .	94
C.4	The principle of the CIP method. (a) The solid line is the initial profile and the dashed line is an exact solution after advection, shown in (b) as discretized points. (c) When (b) is linearly interpolated, numerical diffusion appears. (d) In the CIP, the spartial derivative also propagates and the profile inside a grid cell is retrieved (Yabe et al. (2001)). . . . .	96
C.5	The Marker-and-Cell setup Chan and Street (1970). . . . .	96
C.6	One-dimensional example of Lagrangian, Eulerian and ALE mesh and particle motion Donea et al. (2004). . . . .	98
C.7	Region near floating body (GC: gravitational centre), Yan and Ma (2007a). . . . .	100

# List of Tables

1.1	Recent work in wave-structure interaction. . . . .	2
3.1	Test cases for paddle motion with body-free-surface intersection point. . . . .	22
3.2	Experimental wave data for surging piston wavemaker. . . . .	23
3.3	Comparison cases for second-order wave generation. . . . .	26
4.1	Comparison with first-order wavemaker theory: $kh$ denotes dimensional wave number; $T$ denotes wave period; $\xi$ denotes relative error. All waves have steepness $H/L = 1\%$ . . . . .	41
4.2	Experimental comparison for heaving wedge wavemaker. $\xi_2$ denotes relative 2-norm error with respect to experimentally measured amplitudes. $\xi_{RMS}$ denotes Root Mean Square error with respect to experimentally measured free surface elevation. . . . .	42
4.3	Optimization cases for heaving wedge wavemaker. . . . .	44

# List of Abbreviations

ALE	Arbitrary Lagrangian Eulerian
BC	Boundary Condition
BEM	Boundary Element Method
BVP	Boundary Value Problem
CIP	Constrained Interpolation Profile
DBEIM	Desingularized Boundary Integral Equation Method
DD	Domain Decomposition
FDM	Finite Difference Method
FEM	Finite Element Method
FFT	Fast Fourier-Transform
FNPF	Fully Nonlinear Potential Flow
HOBEM	High-Order Boundary Element Method
HPC	Harmonic Polynomial Cell
IBM	Immersed Boundary Method
IBOGM	Immersed Boundary Overset Grid Method
LBM	Lattice-Boltzman Method
MAC	Marker-And-Cell
MEL	Mixed Eulerian Lagrangian
NS	Navier-Stokes
NWT	Numerical Wave Tank
QALE	Quasi-Arbitrary Lagrangian Eulerian
SEM	Spectral Element Method
SWENSE	Spectral Wave Explicit Navier-Stokes Equations
WLS	Weighted Least Squares

# 1 | Introduction

## 1.1 Background and motivation

Quantifying wave loads on marine structures is critically important to ensure their longevity. As wind turbines and offshore platforms operate in deeper waters, accurate and reliable modelling of deep-water waves becomes crucial in understanding the wave loads such structures must withstand. The general tools for evaluating wave loads on marine structures can be broadly categorized as

1. Experiments, usually at model scale.
2. Semi-empirical methods such as the Morison equation.
3. Linear frequency-domain methods.
4. Linear and weakly-nonlinear time-domain methods.
5. Fully-nonlinear time-domain methods.

Experiments are classically regarded as the gold standard in terms of reliability, but are generally expensive, time consuming, and limited by model-scale effects that may be difficult to account for at full scale. The semi-empirical Morison equation is widely used due to its simple form, relating the force on a structure to an inertial component and a drag component each given by empirical coefficients. However, despite its simplicity, Morison's equation is limited to slender, axisymmetric bodies. Linear frequency-domain methods are typically very efficient, but are limited to small-amplitude waves and body motions, and cannot be used for transient analysis. Linear and weakly-nonlinear time-domain methods are similarly efficient, but share the same limitation regarding small-amplitude motions and waves that can be simulated. Furthermore, higher-harmonic interactions cannot be accounted for, both in terms of wave propagation and wave loading. Finally, fully-nonlinear time-domain methods can resolve both higher-harmonic interactions and transient phenomena, but this often comes at considerable computational expense and complexity.

Given the ever-increasing range of conditions that modern marine structures are exposed to, a general-purpose numerical solver is a very desirable tool for engineering analysis and design. Such a solver must satisfy four general requirements:

- Fast - the computational cost should be as low as possible.
- Fully-nonlinear - the solver should be able to capture all relevant physics.
- Wave-structure interaction,
  - With fixed structures, i.e. wave diffraction.
  - Arising from the forced motion of structures, i.e. wave radiation.
  - With freely-moving structures; i.e. coupled diffraction and radiation.

- 3D - the solver should be able to simulate three-dimensional phenomena.

A great deal of work has been done towards achieving various combinations of these objectives over the past several decades. Table 1.1 collects the most recent work that has included wave-structure interaction. With the advent of parallel computing, the criterion that a solver be “fast” can arguably encompass two non-exclusive situations. In the classical sense, the solution effort of the solver should scale linearly with the number of degrees of freedom in the system. This is typically expressed using Big-O notation as  $O(N)$ -scaling, where  $N$  is the total number of grid points or nodes. Optimal scaling has been demonstrated in a finite-difference framework, both for wave propagation and interaction, for example by Bingham and Zhang (2007), and wave-structure interaction, for example by Glimberg (2013) and Glimberg et al. (2018). Similar results have been achieved using a Spectral Element Multigrid Method by Laskowski et al. (2019) and Engsig-Karup and Laskowski (2020), for linear and nonlinear wave-structure interaction, respectively.

Fully-nonlinear solvers are necessary in order to capture high-order wave-wave interactions and high-order components of wave loading. Solution of the Navier-Stokes equations provides the highest level of detail, by including the effects of fluid viscosity, albeit at the highest computational cost. As a result, many modern solvers use a fully nonlinear potential flow (FNPF) formulation, under the assumptions of an inviscid and irrotational flow. While these assumptions are valid for a large range of situations involving wave-structure interactions, two important limitations of FNPF solvers are their inability to model wave overturning and vortical structures. Instead, wave-breaking must be approximated by numerical dissipation, or a hybrid approach involving a coupling to a viscous solver.

Group	Fast	Fully nonlinear	Wave-structure interaction			2D	3D	Notes
			Fixed	Forced	Free			
Park et al. (1999, 2001, 2003)		x	x				x	NS, MAC
Xue et al. (2001); Liu et al. (2001)		x	x				x	$\phi$ , MEL, HOBEM
Hu et al. (2006)	x		x	x		x		NS, CIP
Luquet et al. (2007)	x			x			x	NS, SWENSE
Ma and Yan (2006); Yan and Ma (2007a); Ma and Yan (2009a)	x		x	x			x	$\phi$ , QALE, FEM
Guerber et al. (2012)	x	x		x		x		$\phi$ , HOBEM
Kang et al. (2014)			x				x	NS, FDM, IBM, $\sigma$
Kontos (2016)	x	x	x			x		$\phi$ , FDM, IBM
Zhang and Kashiwagi (2017a,b)	x		x				x	$\phi$ , ALE, HOBEM
Engsig-Karup et al. (2017, 2019)	x	x	x			x		$\phi$ , MEL, SEM
Glimberg et al. (2018)	x	x	x				x	$\phi$ , FDM, $\sigma$
Harris et al. (2018)	x	x	x	x			x	$\phi$ /NS, BEM, LBM
Ma et al. (2018)	x	x	x	x		x		$\phi$ , HPC, IBM
Bosi et al. (2019)	x	x	x	x	x	x		$\phi$ , SEM
Dombre et al. (2019)	x	x	x	x			x	$\phi$ , BEM
Amini-Ashfar et al. (2019)	x		x			x		$\phi$ , FDM, DD
Hanssen (2019)	x	x	x	x	x	x		$\phi$ , HPC, IBOGM, DD
Laskowski et al. (2019)	x	x	x			x	x	$\phi$ , SEM

**Table 1.1:** Recent work in wave-structure interaction.

As indicated in Table 1.1, low computational cost and the ability to simulate free-body motions are the most elusive properties of modern, fully-nonlinear solvers. The “Notes” column of Table 1.1 contains abbreviations referring to the underlying equations and numerical methods used in each case. The former are either the Navier-Stokes (NS) equations, or a velocity potential ( $\phi$ ) formulation. With regards to the numerical methods and techniques, the reader is referred to the List of Abbreviations, and to Appendix C for a brief overview of each of these.

OceanWave3D (OW3D) is a flexible-order, finite-difference-based, fully nonlinear potential flow solver that has been developed at the Technical University of Denmark by Engsig-Karup et al. (2009). It was inspired by the work of Li and Fleming (1997), which was later extended by Bingham and Zhang (2007), and uses a  $\sigma$ -transformation of the vertical coordinate to reduce computational cost. The solution effort of the solver scales linearly with the number of degrees of freedom, and it has been implemented on massively parallel architectures by Engsig-Karup et al. (2012), Glimberg (2013), and Glimberg et al. (2018). Linear wave-structure interaction in a moving frame of reference was introduced by Lindberg et al. (2014) and Afshar (2014), and was extended to fully-nonlinear wave-structure interaction by Kontos (2016). An Immersed Boundary Method (IBM) is used to include structures in the solver, where Weighted Least Squares (WLS) approximations are used to satisfy the body boundary condition. This method allows for efficient grid generation without the need for regridding throughout the simulations, although local stencils and operators must be updated as the body moves through the grid. Finally, the free-surface variables are time-stepped using an explicit fourth-order, four-stage Runge-Kutta method.

The demonstrated capability of the OW3D solver, both in terms of computational cost and the ability to simulate wave-structure interaction, presents a solid foundation for further development.

## 1.2 Research objectives and scientific contribution

The primary motivation for this research is to address nonlinear wave-structure interaction. This is done by expanding the capabilities of an existing framework, OW3D, as well as addressing several challenges within the framework. The challenges that are addressed are as follows:

1. OW3D combines a  $\sigma$ -transformation of the vertical coordinate with an IBM for modelling structures. The former requires a  $C^2$ -continuous free surface at all times and, as the latter allows a body to move through the grid without regridding, an artificial free surface must be generated in the interior of any free-surface-piercing body after each Runge-Kutta stage. Problems can arise in the generation of the artificial interior free surface, particularly when there are large gradients in the free surface close to the body.
2. OW3D combines an IBM with a multi-stage time-stepping method. This means that computational points can enter/exit the body not only between time steps, but also between Runge-Kutta stages. These points need to be assigned appropriate values, otherwise they will introduce errors in the time-stepping. Furthermore, some modification of the Runge-Kutta summation is required when this happens.
3. OW3D previously showed spurious oscillations in the calculated force signal when considering wave-structure interaction. Many authors have reported numerical oscillations when using an IBM (Berthelsen and Faltinsen (2008); Pan and Shen (2009); Liao et al. (2010); Lee

et al. (2011); Luo et al. (2012); Hanssen et al. (2015); Kontos (2016)). This may be linked to truncation error differences between time steps, which can lead to numerical instabilities. Lee et al. (2011) and Kontos (2016) suggest that this may be mitigated by increased spatial resolution and time-step size, but the underlying problem remains. In the context of OW3D, this may also be linked to poor treatment of new computational points as they emerge from the body, as detailed above, and to inconsistent handling of the integration limits when integrating the pressure over the wetted surface. The latter could result in significant differences in the integration between time steps, as mentioned by Kontos (2016).

4. Finally, while the OW3D framework itself is flexible-order, wave-structure interaction has only been demonstrated at second-order.

There are two main research hypotheses to address these challenges. The first concerns the introduction of body-free-surface intersection tracking, which seeks to address challenges (1) and (2) outlined above. The second concerns the implementation of an acceleration potential method for calculating the force on a body, which seeks to address challenges (3) and (4) outlined above. These will be introduced below, and discussed in more detail in subsequent sections. The overall goal is to develop an efficient numerical framework capable of simulating nonlinear wave-structure interactions at arbitrary order, for both forced and free-body motion problems.

Finally, the OW3D solver is validated and applied to the problem of wave generation with a moving boundary. This will also be discussed in more detail below.

### 1.2.1 Body-free-surface intersection point tracking

As mentioned above, the introduction of body-free-surface intersection tracking seeks to address the various problems that arise from the combination of using a  $\sigma$ -transformation, an IBM, and a multi-stage time-stepping method. The central idea is to implement a semi-Lagrangian point, or points, which move freely through the fixed computational grid while at all times remaining on both the body surface and the free surface.

As described above, OW3D uses a  $\sigma$ -transformation of the vertical coordinate in combination with an IBM for modelling structures. The  $\sigma$ -transformation of the vertical coordinate (described in more detail in Section 3.1) maps the time-varying physical domain to a time-invariant computational domain, but requires that the free surface is  $C^2$ -continuous at all times. This criterion is easily satisfied in the case of pure wave propagation or wave-wave interaction, at least up to the point of wave breaking, but presents a problem when including bodies in the domain. The presence of a surface-piercing body disrupts the wave field, which entails that an artificial free surface must be constructed in the interior of the body at each Runge-Kutta stage. This process is detailed in Kontos (2016), but in short:  $C^2$ -continuity is ensured by fitting a 7th-order polynomial to points inside the body, where the derivatives of the free surface at the body-free-surface intersection points serve as boundary conditions. This means that the location and derivatives of the free surface at the body-free-surface intersection points are of paramount importance when ensuring  $C^2$ -continuity in the free-surface variable. This has been a limiting factor in previous work with the OW3D solver, as described in Kontos (2016), where the intersection point has been found by one-sided extrapolation from free-surface variables. This is particularly problematic when there

are large gradients in the free surface close to the body. Consistent knowledge of the intersection point location will provide a better basis for approximating the derivatives at this point.

Furthermore, as the time-stepping procedure used in OW3D is a four-stage Runge-Kutta method, using an IBM introduces the possibility that computational points will move into and/or out of the body not only between time steps, but also between Runge-Kutta stages. Consistent values of the free-surface variables must be extrapolated to these points when this occurs, in order to avoid introducing errors into the solution. Again, knowledge of the intersection point location and its velocity potential value will improve the extrapolation of this information to new fluid points.

Finally, evaluation of wave loads requires integration of the pressure over the wetted surface. The limits of this integration (i.e. the waterline points) must be known consistently in order to avoid spurious variations in the calculated force. One promising method to deal with these problems is the introduction of a body-free-surface intersection point, an idea that will be pursued in this thesis.

### 1.2.2 Evaluation of nonlinear wave loads when using an IBM

As mentioned above, previous methods for evaluating the wave loads on moving structures can lead to spurious oscillations of the calculated force when using an IBM (see for example Lee et al. (2011); Kontos (2016)). While this can be mitigated to some degree by increasing both the spatial resolution and time step size, a solver that must increase a discretization parameter to reduce errors does not fulfil the convergence requirement. A robust method for calculating the wave force when using an IBM is therefore desired. The wave force is calculated by integrating the pressure over the wetted surface of a body, where the pressure is dependent on the time derivative of the velocity potential. Previous work with the OW3D solver has approximated this time-derivative based on finite-differencing (Kontos (2016)). There are two key problems with this approach. Firstly, using backward-finite-differencing in time is known to be unstable when considering free-body motions (Kashiwagi (1996)), so such a method is limited to forced motions or fixed structures. Secondly, when simulating wave interaction with forced motions or fixed structures using an IBM, approximating the time derivative in post-processing, based on stored values of the velocity potential at each time step, can suffer from the spurious oscillations mentioned above. The hypothesis for the research presented here is that these oscillations stem from a combination of the way body points are treated in the IBM, and the use of finite-differencing to approximate the time derivative of the velocity potential. The hypothesis is thus that oscillations may be removed by solving a new boundary value problem for the time derivative of the velocity potential at each time step, in a way that ensures a coupling of the body and fluid motions at any given time. Therefore, in this work, an implicit boundary value problem for the time derivative of the velocity potential on the body surface is implemented based on the formulation of Tanizawa (1995). This both allows the wave force to be calculated directly at each time step, and facilitates the simulation of free-body motions. The implementation recasts the implicit problem in terms of matrix-vector products, such that it may be solved directly as a new system of coupled equations. This is tested on explicit forced-motion cases, and subsequently on the implicit solution of a submerged surging dipole, and surface-piercing circular cylinder.

### 1.2.3 Wave generation using a moving boundary

The central idea of this part of the work is the development of a numerical optimization procedure that may be used with wavemakers of arbitrary shape to generate stable waves of constant form. As has been shown in recent papers (Kontos et al. (2016), Kontos (2016)), the OW3D solver has been extended to include nonlinear wave-structure interaction in a moving frame of reference. This extension was tested against various analytical, numerical, and experimental cases, both linear and nonlinear, covering the forced motion of heaving cylinders and wedges. The goal of these cases was a comparison of the force evaluated on the body surface. Given these validations, OW3D may be considered a valid tool for the investigation of nonlinear wave-structure interaction, at least for non-breaking waves. One such avenue of research is the problem of wave generation by a moving boundary. In numerical wave tanks it is possible to specify arbitrary waves using wave-generation zones combined with high-order Stokes, cnoidal, or stream-function theories (Fenton (1988)) to specify initial/boundary conditions. This is not the case in physical wave tanks, where waves must be generated by a moving boundary. Much work has already been undertaken in developing wavemaker theory, which will be covered in more detail in Section 2.2. The current state of the art achieves first- and second-order accurate wave fields generated primarily by piston or flap-type wavemakers.

An optimization procedure to generate stable waves of constant form is of interest for experimental wave tanks, as much of the current literature is devoted to focused design waves rather than stable wave fields. Furthermore, knowledge of the exact motion required to generate a given wave field is equivalent to the knowledge of the motion required to absorb such a wave. This work is therefore also of interest for the design and testing of wave energy converters.

## 2 | Theoretical framework

This chapter introduces the theoretical basis for the solver. The first section describes the general theory regarding the solver. The second section deals more specifically with theory concerning the generation of waves in experimental and numerical wave tanks. Finally, the third section presents theory concerning free-body motion.

In the following, vector quantities will be denoted with bold variables.

### 2.1 Governing equations

A complete physical model of wave-structure interaction in numerical simulations requires solution of the Navier-Stokes equations, a task that comes at high computational cost. For many engineering applications, neglecting viscosity and vorticity and assuming a constant density can provide satisfactory results with a significant reduction in both computational cost and complexity. These assumptions essentially mean that potential flow theory is not able to provide reasonable predictions of flow regions containing wakes and boundary layers. The full theory concerning potential flow is well-described in Newman (2017); a brief overview is reproduced here.

Given the case of an incompressible flow, the continuity equation reduces to the condition that the velocity  $\mathbf{u}$  has zero divergence

$$\nabla \cdot \mathbf{u} = 0, \quad (2.1)$$

with the dot denoting the inner product. Under the additional assumptions that the flow is inviscid and irrotational, the flow velocity may be described by the gradient of a scalar velocity potential. This means the velocity potential  $\phi$  must satisfy Laplace's equation

$$\nabla^2 \phi = \Delta \phi = 0, \quad (2.2)$$

which is the governing equation at the heart of the potential flow formulation. Figure 2.1 shows the general physical domain including an arbitrary body. The free surface interior to the body is generated artificially - this will be discussed in Sections 3.1 and 3.5. A Cartesian coordinate system is positioned such that the  $x$ - and  $y$ -axes are located in the still-water plane, with the  $z$ -axis positive upwards from the still water level, where  $z = 0$ . The water depth  $h(\mathbf{x})$  and free surface elevation  $\eta(\mathbf{x}, t)$  are likewise measured from the still water level. A structure in the domain is characterized by an outward-pointing normal vector at each point on its surface, denoted by  $\mathbf{n} = (n_x, n_y, n_z)$ . In this system, the symbol  $\nabla$  is taken to mean the two-dimensional gradient operator in the  $(x, y)$  plane, i.e.  $\nabla = (\partial/\partial x, \partial/\partial y)$ . Boundary conditions are required at each of the domain boundaries

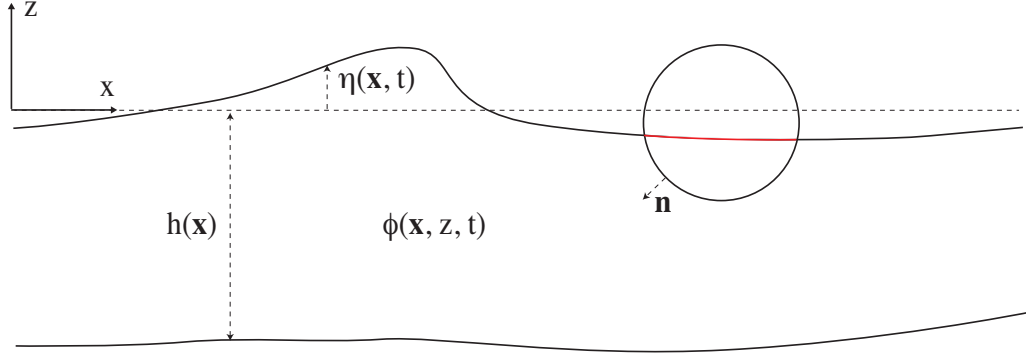


**Figure 2.1:** General physical domain. Artificial interior free surface marked in red.

in order to solve the Laplace equation. At the sea bed, the no-flux condition is expressed as

$$\frac{\partial \phi}{\partial z} + \nabla h \cdot \nabla \phi = 0. \quad (2.3)$$

On the body boundary, a similar no-flux condition equates the normal components of the fluid velocity to those of the body velocity, given by

$$\frac{\partial \phi}{\partial n} = V_n, \quad (2.4)$$

where  $V_n(\mathbf{x}, z, t)$  is the normal component of velocity of a point on the body surface,  $S_b$ .

At the free surface, the kinematic and dynamic boundary conditions require that the vertical velocity of the free surface and fluid particles are equal (a particle on the free surface stays on the free surface), and that the pressure is equal to atmospheric pressure, respectively. The former can be derived by requiring that the material derivative of the quantity  $z - \eta$  must vanish on the free surface. Therefore, on  $z = \eta$

$$\frac{D}{Dt}(z - \eta) = \frac{\partial \phi}{\partial z} - \frac{\partial \eta}{\partial t} - \frac{\partial \phi}{\partial x} \frac{\partial \eta}{\partial x} - \frac{\partial \phi}{\partial y} \frac{\partial \eta}{\partial y} = 0 \quad (2.5)$$

$$\frac{\partial \eta}{\partial t} = \frac{\partial \phi}{\partial z} - \nabla \phi \cdot \nabla \eta \quad (2.6)$$

The dynamic boundary condition is obtained from Bernoulli's equation. Assuming the atmospheric pressure  $p_a$  is independent of position on the free surface and choosing the constant of integration  $C(t)$  suitably, the exact condition to be satisfied on the free surface is

$$-\frac{1}{\rho}(p - p_a) = \frac{\partial \phi}{\partial t} + \frac{1}{2}\nabla \phi \cdot \nabla \phi + gz = 0. \quad (2.7)$$

Substituting the free surface elevation  $\eta$  for  $z$  and rearranging:

$$\frac{\partial \phi}{\partial t} = -g\eta - \left( \frac{1}{2}\nabla \phi \cdot \nabla \phi \right). \quad (2.8)$$

The free surface boundary conditions may also be written in the Zakharov form, where they are defined exclusively in terms of free-surface variables, Zakharov (1968)

$$\frac{\partial \eta}{\partial t} = -\nabla \eta \cdot \nabla \tilde{\phi} + \tilde{w}(1 + \nabla \eta \cdot \nabla \eta) \quad (2.9)$$

$$\frac{\partial \phi}{\partial t} = -g\eta - \frac{1}{2}(\nabla \tilde{\phi} \cdot \nabla \tilde{\phi} - \tilde{w}^2(1 + \nabla \eta \cdot \nabla \eta)), \quad (2.10)$$

where  $\tilde{\phi} = \phi(\mathbf{x}, \eta, t)$  and  $\tilde{w} = \frac{\partial \phi}{\partial z}|_{z=\eta}$  are the velocity potential and vertical component of velocity evaluated directly on the free surface.

These equations, together with prescribed initial conditions at the free surface, describe the full initial boundary value problem for  $\phi$ ,

$$\nabla^2 \phi + \phi_{zz} = 0, \quad \text{in } -h < z < \eta, \quad (2.11a)$$

$$\eta_t + \nabla \eta \cdot (\nabla \tilde{\phi} - \tilde{w} \nabla \eta) = \tilde{w}, \quad \text{on } z = \eta, \quad (2.11b)$$

$$\tilde{\phi}_t + \frac{1}{2} \nabla \tilde{\phi} \nabla \tilde{\phi} - \frac{1}{2} \tilde{w}^2 (1 + \nabla \eta \nabla \eta) = -g \eta, \quad \text{on } z = \eta, \quad (2.11c)$$

$$\phi_z + \nabla h \cdot \nabla \phi = 0, \quad \text{on } z = -h, \quad (2.11d)$$

$$\phi_n = V_n, \quad \text{on } \mathbf{S}_b, \quad (2.11e)$$

$$\eta(\mathbf{x}, 0), \tilde{\phi}(\mathbf{x}, 0) \quad \text{given.} \quad (2.11f)$$

Here the subscripts denote partial derivatives with respect to the subscripted variable.

## 2.2 Wavemaker theory

The field of wavemaker theory seeks to relate the motion of wavemakers to the far-field waves that they generate using some form of transfer function. The first effort in this respect was presented by Havelock (1929), based on a linearized version of the wave theory developed by Stokes (1847). This first-order theory was implemented and further developed for paddle-type wavemakers by Bi  sel and Suquet (1951a,b)<sup>1</sup>, and for both paddle- and piston-type wavemakers by Ursell et al. (1960). These articles also identified the presence of higher harmonic and evanescent modes in the waves generated by first-order theory. Here, a paddle-type wavemaker is a planar surface usually hinged at or above the bottom of a wave tank, oscillating around the hinge point, and a piston-type wavemaker is a planar surface with a surging oscillatory motion. A third type of wavemaker, referred to as a plunger, operates with a heaving oscillatory motion. This was first studied by Ursell (1949), for a heaving circular cylinder, and generalized to plungers of more general shape by Wang (1974) through the use of a conformal mapping. Ellix and Arumugam (1984) conducted experiments with a heaving wedge, and measured both first and second-order components of the generated waves. Wu (1988) developed a more general approach for wedge-shaped wavemakers, removing the assumption of deep water from the work of Wang (1974).

The first second-order theory was proposed by Fontanet (1961a,b)<sup>2</sup>, who included a second-order superharmonic term in the wavemaker control signal in order to suppress the spurious superharmonics identified previously. However, the choice of a Lagrangian coordinate system made this solution complicated to apply. An alternate second-order theory was developed by Madsen (1970, 1971), using a Stokes-like expansion, but this was limited to relatively long waves. Hansen and Svendsen (1975) used an empirical, experimental process to derive second-order control signals for a piston-type wavemaker. This was done by measuring the magnitude of the spurious, free second harmonic when using a first-order signal, and then including a second-order term to

<sup>1</sup>Papers written in French.

<sup>2</sup>Papers written in French.

suppress this. Flick and Guza (1980) further investigated the second-order wave field generated by first-order control signals.

A complete second-order theory for monochromatic wavemaker motion was derived by Hudspeth and Sulisz (1991), using an eigenfunction expansion approach. This was extended by Moubayed and Williams (1994) to include bichromatic wavemaker motions. The complete second-order theory for irregular wave fields was presented by Schäffer (1996), using a complex representation. The key result of this work is a complex transfer function which is applied to the second-order control signal, ensuring that spurious free waves are suppressed. The work was validated experimentally, and included in a numerical wave tank (NWT) by Skourup and Schäffer (1997). Schäffer and Steenberg (2003) extended this to multidirectional waves in three dimensions. Zhang and Schäffer (2007) presented a new second-order method based on stream function theory, which combined linear fully-dispersive wavemaker theory with wave generation for nonlinear shallow water waves.

Despite these theoretical advances, Masterton and Swan (2008) suggested that an empirical calibration approach is still necessary in experimental wave tanks, and presented such a calibration of a linear transfer function for paddle-type wavemakers. The ad hoc unified wave generation approach of Zhang and Schäffer (2007) was extended by Yang et al. (2013, 2014a,b), who included a second-order dispersive correction and provided both numerical and experimental validation for regular and irregular waves. Thus, while theoretical solutions exist for stable wave fields accurate to second order, these may not transfer directly to experimental wave tanks.

### 2.2.1 Schäffer's second-order wavemaker theory

The full second-order theory presented in Schäffer (1996) is based on a complex representation, and separates the second-order problem into three contributions. The free-surface elevation and velocity potential accurate to second order may thus be represented by

$$\begin{aligned}\eta &= \eta^{(1)} + \eta^{(2)} \\ \eta &= \eta^{(1)} + \eta^{(21)} + \eta^{(22)} + \eta^{(23)} \\ \phi &= \phi^{(1)} + \phi^{(2)} \\ \phi &= \phi^{(1)} + \phi^{(21)} + \phi^{(22)} + \phi^{(23)},\end{aligned}\tag{2.12}$$

where  $\phi^{(21)}$  describes the bound waves due to interaction between first-order wave components,  $\phi^{(22)}$  describes the free waves due to both the wavemaker leaving its mean position and  $\phi^{(21)}$  mismatching the boundary condition at the wavemaker, and  $\phi^{(23)}$  describes the free waves generated by the second-order wavemaker motion (Schäffer (1996)). The goal of second-order theory is therefore to determine the second-order wavemaker control signal that will produce free waves  $\eta^{(23)}$  that exactly cancel the spurious free waves  $\eta^{(22)}$ ; i.e.

$$\eta^{(22)} + \eta^{(23)} = 0.\tag{2.13}$$

This will, theoretically at least, result in a wave field composed solely of bound components, and is achieved through the second-order transfer function  $\mathcal{F}^\pm$ , which is the main result of Schäffer

(1996). Using this second-order transfer function, the wavemaker control signal is defined as

$$\begin{aligned} X_0 &= X_0^{(1)} + X_0^{(2)\pm} \\ &= \frac{1}{2} \left\{ -iX_a e^{i\omega t} + c.c. \right\} + \frac{1}{2} \left\{ -i\mathcal{F}^\pm \frac{A_n A_m^{-: *}}{h} e^{i(\omega_n \pm \omega_m)t} + c.c. \right\}. \end{aligned} \quad (2.14)$$

Here  $X_a$  is the constant complex first-order wavemaker amplitude, which is related to the complex amplitude  $A$  of the progressive part of the first-order wavefield through

$$A = c_0 X_a, \quad (2.15)$$

where  $c_0$  is the first-order transfer function of Bi  sel and Suquet (1951a,b). Furthermore, in Eq. (2.14), c.c. refers to the complex conjugate of the preceding term, the subscripts  $n$  and  $m$  refer to the two wave components comprising the second-order spectrum, which contains both superharmonic and subharmonic interaction terms (sum and difference frequencies, respectively), and the notation  $- : *$  is defined by Sch  ffer (1996) as

$$Z^{-: *} = \begin{cases} Z & \text{for superharmonics} \\ Z^* & \text{for subharmonics,} \end{cases} \quad (2.16)$$

where  $*$  denotes the complex conjugate. The full definition of the second-order transfer function is shown in Appendix B.

### 2.2.2 Wave field stability

The stability of a wave field may be characterized by the variation in its constituent harmonic components across a given test section. A given time series of the free surface elevation,  $\eta(t)$ , can be decomposed using a least-squares fit of sinusoids at predefined frequencies. When the frequencies are harmonic, i.e. integer multiples of the fundamental frequency, the result may be expressed as

$$f(t) = \bar{a} + \sum_{n=1}^N a_n \cos(2\pi\omega_n(t - \delta_n)), \quad (2.17)$$

where  $f(t)$  is the fitted function,  $\bar{a}$  is a mean value,  $a_n$  are the harmonic amplitudes,  $\omega_n$  the harmonic frequencies, and  $\delta_n$  the associated phases. The accuracy of such a fit is quantified by the mean squared residual

$$\kappa = \sqrt{\frac{\sum(\eta(t) - f(t))^2}{\|\eta(t)\|_2}}, \quad (2.18)$$

where  $\|\eta(t)\|_2$  represents the 2-norm (Euclidean norm) of the time series. While a similar result may be achieved using Fourier analysis, harmonic analysis is more robust, as it does not require an exact number of periods to avoid aliasing when converting a time series to the frequency domain. Furthermore, as the desired wave fields will be expressed in terms of harmonic amplitudes, based on stream function theory, using a similar summation of cosines to determine the error is straightforward. For a wave field to be considered stable, the amplitudes,  $a_n$ , must not vary with position.

The potential instability of periodic wave trains in deep water was demonstrated in Benjamin and Feir (1967) and Benjamin and Hasselmann (1967), who described a gradual disintegration

due to side-band instabilities. Referred to as the Benjamin-Feir instability, this occurs when the energy contained in waves of moderate amplitude (below the breaking limit) is gradually lost to other waves of similar frequency and direction. The amplitudes of these other waves increase exponentially over distance. Given a wave train with fundamental frequency  $\omega$ , wave number  $k$ , and amplitude  $a$ , the amplitude of side-band modes at frequency  $\omega(1 \pm \delta)$  increases by

$$\varepsilon = e^{\delta(2k^2a^2-\delta^2)^{\frac{1}{2}}kx}. \quad (2.19)$$

The presence of such an instability does not, however, invalidate attempts at generating a stable wave field. Rather it presents an upper limit to the position of a test section in a wave tank, beyond which the magnitude of the side-band amplitudes will become too large. Furthermore, later work by Segur et al. (2005) indicates that the presence of dissipation can limit the growth of side-band amplitudes to such an extent that nonlinear interaction with the travelling wave becomes negligible.

### 2.3 Free-body motion

The problem of free-body motion in maritime applications has been studied extensively, starting with Froude (1861). Much of the early work was based on linear theories, such as the strip theory presented in Salvesen et al. (1970), and the unified slender-body theory of Newman (1978), which was further developed in Newman and Sclavounos (1980), Sclavounos (1984), and Kashiwagi et al. (2000). These theories relied on an assumption of small amplitude waves and correspondingly small motions of the floating body. The use of perturbation theories could allow weakly nonlinear problems to be treated, but this quickly becomes very complicated. The extension to fully nonlinear free-body motion is also complicated, and care must be taken due to the coupling of wave and body motion through the kinematic body boundary condition. The key issue is to calculate the fluid force acting on the body at each time level. This force is obtained by integrating the pressure over the wetted body surface, where the pressure is given by Bernoulli's equation,

$$p = -\left(\phi_t + \frac{1}{2}(\nabla\phi \cdot \nabla\phi) + gz\right). \quad (2.20)$$

Here  $z = 0$  at the mean water level, and  $p = 0$  on the free surface. While  $\phi$  and  $\eta$  are assumed to be known at a given time level, Eq. (2.20) also requires knowledge of  $\phi_t$  on the body surface. The simplest approach is a backward finite difference scheme using  $\phi$  from previous time levels, but this does not ensure hydrodynamic equilibrium at the current time level and can thus lead to instabilities (Tanizawa (1995)). Essentially, each time level must be treated as a new initial-boundary-value problem and must not depend on previous levels. There are four known methods for treating this problem: the modal decomposition method first presented in Vinje and Brevig (1981); the implicit boundary condition method of Tanizawa and Sawada (1990); the iterative method developed by Cao et al. (1994); and the indirect method of Wu and Taylor (1996). A brief overview of each method will be presented below. A detailed review of the different formulations for the body boundary condition may be found in Letournel et al. (2017).

### 2.3.1 Modal decomposition method

The first consistent treatment of the free-body problem in the two dimensional case was presented in Vinje and Brevig (1981), who demonstrated a modal decomposition method for the acceleration field. This was derived in terms of the complex potential and stream function, and decomposed the acceleration field into four modes: unit acceleration of the three body modes (surge, heave, and pitch), and other accelerations arising from the velocity field. The boundary value problem corresponding to each of these modes was then solved, and combined with the equation of body motion to retrieve the body accelerations. This method was subsequently used in Cointe (1989)<sup>3</sup>, Cointe et al. (1991), and Tanizawa and Minami (2001), the latter implementing it as part of a three-dimensional BEM solver. It was further developed by Koo and Kim (2004) and Koo and Kim (2006), who combined it with the acceleration potential method of Tanizawa (1995) and showed that the modal decomposition method is mathematically identical to the indirect method.

### 2.3.2 Implicit boundary condition method

The implicit boundary condition method was first proposed in Tanizawa and Sawada (1990)<sup>4</sup>. The fully consistent formulation was further developed in two dimensions by Tanizawa (1995), although it was also developed independently by van Dalen (1993), who extended it to three dimensions. The principle of the method is to develop an exact implicit body boundary condition for  $\phi_t$ , which is found after solving the boundary value problem for  $\phi$ . This has been implemented in several BEM solvers (Tanizawa (1996), Tanizawa (1998), Shirakura et al. (2000), Guerber et al. (2012)), as well as in a three-dimensional panel method by Berkvens (1998), who made the method more general by allowing for deformable bodies and mass distribution changes.

### 2.3.3 Iterative method

The iterative method of Cao et al. (1994) establishes an expression for the normal derivative of  $\phi_t$  on the body surface, which includes both the body velocity and acceleration ( $\vec{V}_b$  and  $\frac{\partial \vec{V}_b}{\partial t}$ , respectively). This is used in combination with a system of first-order ordinary differential equations describing the free surface and body boundary conditions, where the acceleration of the body surface depends implicitly on the force acting on the body. Their iterative procedure starts by solving the boundary value problem for  $\phi$ , then estimating an initial value of  $\frac{\partial \vec{V}_b}{\partial t}$  based on the previous time level and iterating towards a solution of the boundary value problem for  $\phi_t$  on the body surface. This principal was further developed in Yan and Ma (2007a), Yan and Ma (2007b), and Ma and Yan (2009b), who proposed a new method named ISITIMFB (Iterative Semi Implicit Time Integration Method for Floating Bodies) in both a two-dimensional and three-dimensional QALE-FEM solver. In these latter works, both the body velocity and acceleration are estimated implicitly.

---

<sup>3</sup>Paper written in French.

<sup>4</sup>Paper written in Japanese.

### 2.3.4 Indirect method

The indirect method was proposed by Wu and Taylor (1996), and is based on the same principle as the implicit boundary condition method. However, instead of solving an implicit equation for  $\phi_t$ , this method defines an artificial function such that the velocity and acceleration fields may be solved simultaneously. This allows the force on the body to be calculated directly, albeit without retrieving the pressure distribution on the body explicitly. This method was implemented in a Higher Order BEM by Kashiwagi (1998) and Kashiwagi (2000), and a coupled FEM/BEM solver by Wu and Taylor (2003).

### 2.3.5 Concluding remarks

Of the four methods, the implicit body boundary condition method of Tanizawa (1995) is thought to be the most promising for implementation in OW3D when considering nonlinear wave-structure interaction using an IBM. The method provides a fully consistent coupling between body and fluid motions with no need for iteration, and allows the pressure distribution to be calculated rather than just the force on the body. Furthermore, as the implicit body boundary condition is expressed in terms of the normal derivative on the body surface, the system matrix used to solve the velocity potential problem can be re-used with some modifications. Details of the implementation will be presented in Section 3.6.

# 3 | Numerical implementation

This chapter describes the various methods and techniques that make up the OW3D solver: how the governing equations are discretized, how bodies are introduced into the simulations, and how wave loading is calculated for both forced and free motion.

## 3.1 Sigma-transform

Free-surface flows are characterised by a time-dependent free surface, the position of which is unknown *a priori*. As the boundary conditions must be satisfied exactly at the free surface, some method of tracking the time-evolution of the free surface is required. This typically either involves an interface-capturing scheme (see Appendix C for some examples), or regressing the computational domain at each time-step. These procedures can introduce a significant computational expense, which may be avoided by mapping the physical domain to a time-invariant computational domain. This has the double benefit of removing the need for regressing and allowing the derivative operators to be calculated once, at the beginning of simulations. The mapping is done by a non-conformal transformation of the vertical coordinate, defined by

$$\sigma(\mathbf{x}, z, t) = \frac{z + h(\mathbf{x})}{\eta(\mathbf{x}, t) + h(\mathbf{x})} = \frac{z + h(\mathbf{x})}{d(\mathbf{x}, t)}, \quad (3.1)$$

where  $d = \eta + h$  is the total thickness of the fluid. The  $\sigma$ -coordinate therefore runs from zero at the sea bed to one on the free surface. This change of coordinate means the Laplace problem must be adjusted in the computational domain, to

$$\nabla^2 \phi + \nabla^2 \sigma \phi_\sigma + 2 \nabla \sigma \cdot \nabla \phi_\sigma + (\nabla \sigma \cdot \nabla \sigma + \sigma_z^2) \phi_{\sigma\sigma} = 0, \quad 0 \leq \sigma < 1 \quad (3.2a)$$

$$(\sigma_z + \nabla h \cdot \nabla \sigma) \phi_\sigma + \nabla h \cdot \nabla \phi = 0, \quad \sigma = 0. \quad (3.2b)$$

The derivatives of  $\sigma$  are given by

$$\begin{aligned} \nabla \sigma &= (1 - \sigma) \frac{\nabla h}{d} - \sigma \frac{\nabla \eta}{d}, \\ \nabla^2 \sigma &= \frac{1 - \sigma}{d} \left( \nabla^2 h - \frac{\nabla h \cdot \nabla h}{d} \right) - \frac{\sigma}{d} \left( \nabla^2 \eta - \frac{\nabla \eta \cdot \nabla \eta}{d} \right) \\ &\quad - \frac{1 - 2\sigma}{d^2} \nabla h \cdot \nabla \eta - \frac{\nabla \sigma}{d} \cdot (\nabla h + \nabla \eta), \\ \sigma_z &= \frac{1}{d}. \end{aligned} \quad (3.3)$$

The flow velocities are obtained by the chain rule,

$$\begin{aligned} \mathbf{u}(\mathbf{x}, z) &= \nabla \phi(\mathbf{x}, z) = \nabla \phi(\mathbf{x}, \sigma) + \nabla \sigma \phi_\sigma(\mathbf{x}, \sigma), \\ w(\mathbf{x}, z) &= \phi_z(\mathbf{x}, z) = \phi_\sigma(\mathbf{x}, \sigma) \sigma_z. \end{aligned} \quad (3.4)$$

One important caveat of the  $\sigma$ -transform is that the free surface must always be  $C^2$ -continuous. This will be discussed further in Section 3.5.1, but the main effect this has on simulations is that an artificial free surface must be constructed in the interior of any surface-piercing bodies included in the domain.

## 3.2 Finite-Difference Method

The governing equations (3.2) are discretized using the Finite-Difference Method (FDM). The FDM has been widely used over the past five decades due to its ease of implementation and low computational cost. In this method, derivatives in a differential equation are approximated using a truncated Taylor series

$$f(x + \Delta x) = f(x)^{(0)} + \Delta x f^{(1)}(x) + \Delta x^2 \frac{f^{(2)}(x)}{2!} + \dots + \Delta x^{n-1} \frac{f^{(n-1)}(x)}{(n-1)!} + O(\Delta x^n), \quad (3.5)$$

where the superscript  $(n)$  indicates the  $n$ -th derivative. In this work, finite-difference derivative operators are built as sparse matrices on a logically structured grid, with a small linear system being inverted at each grid point to find the appropriate coefficients. The first and second derivatives in the horizontal and vertical directions are approximated using stencils of  $r = a + b + 1$  neighbouring points, where  $a$  indicates the number of points to the left/bottom and  $b$  indicates the number of points to the right/top of the point of interest. Mixed derivatives are discretized using a square stencil of  $r^2$  points. Interior points are discretized with central-differencing, where  $a = b$ , and off-centred stencils are used near non-periodic domain boundaries. The formal accuracy of first-derivatives is  $O(\Delta x_{max}^{r-1})$ , where  $\Delta x_{max}$  is the maximum overall grid spacing. One layer of ghost points is distributed along the bottom and side walls, which ensures that the Laplace equation and Neumann boundary conditions are satisfied at all boundary points. The free surface is treated as a Dirichlet boundary, where the known solution from the previous time level is specified.

The full discretization of the governing equations (3.2) leads to a linear system of equations

$$\mathbf{A}\phi = b, \quad (3.6)$$

where  $\mathbf{A}$  is the finite difference coefficient matrix,  $\phi$  is a vector of the unknown velocity potential values at each grid point, and  $b$  is a vector holding the right-hand-side values of the equations. These are generally zero, corresponding to the Laplace equation, except at domain boundaries with inhomogeneous conditions.

## 3.3 Immersed Boundary Method

The Immersed Boundary Method (IBM) presented in Lindberg et al. (2014) and Kontos (2016) is used to simulate structures moving through the fixed computational domain. This method uses Weighted Least Squares (WLS) stencils of points to approximate the normal derivative in the body boundary condition, resulting in a sharp interface between the body and surrounding fluid. The reader is referred to Kontos (2016) for a detailed discussion of the WLS approximations, which shows that the order of approximation of the  $n$ -th derivative is at least  $p \geq r - n$ . Figure 3.1

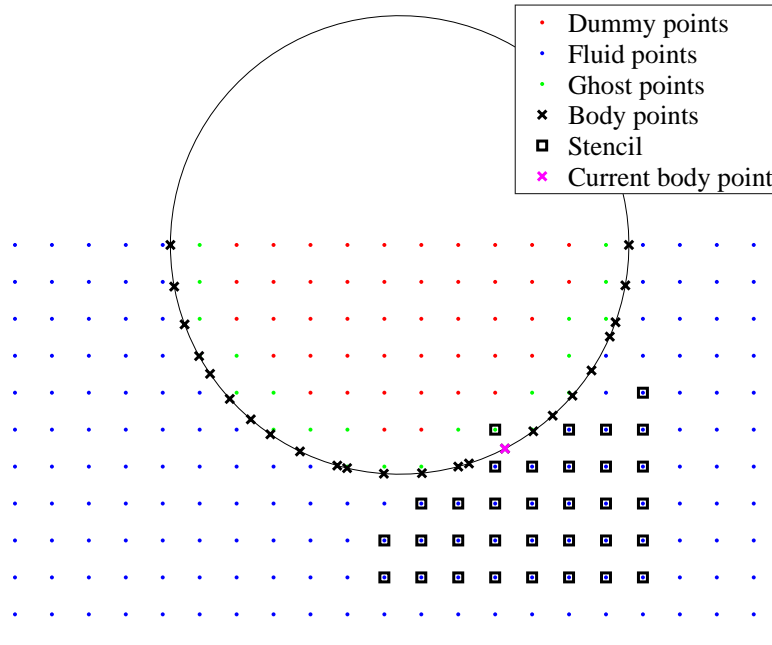


**Figure 3.1:** Point classification for the Immersed Boundary Method.

shows an example of the point classification that is part of the IBM. Points external to the body are classified as fluid points, where the Laplace equation is solved. Points interior to the body which are incorporated in the WLS stencils are classified as ghost points. Other points interior to the body are classified as dummy points, and their corresponding  $\phi$  value is set to zero. Finally, body points are found by the normal projection of ghost points onto the body surface, and are the locations where the body boundary condition is satisfied.

However, as will be demonstrated in Section 3.6.2, distributing the body points in this manner can lead to instabilities when integrating over the wetted surface of the body. These instabilities occur when there is a large difference in the maximum and minimum arc lengths between body points. The method for finding body and ghost points is therefore updated, using the following algorithm:

1. Find ghost points based on their distance to the body surface. In the current work, this is done in the following steps:
  - Find all points inside the body.
  - Compute the local minimum grid spacing close to the body,  $\Delta x_{min}$  and  $\Delta z_{min}$ .
  - Compute the corresponding diagonal distance,  $d_{min} = \sqrt{\Delta x_{min}^2 + \Delta z_{min}^2}$ .
  - Designate all points within  $d_{min}$  of the body surface as ghost points. For a circle of radius  $R$  and center  $(x_0, z_0)$ , ghost points will have coordinates  $(x, z)$  where  $R - \sqrt{(x - x_0)^2 + (z - z_0)^2} < d_{min}$ .
2. Find waterline points, at the body-free-surface intersections.
3. Distribute  $n_g$  body points uniformly from waterline to waterline, where  $n_g$  is the number of

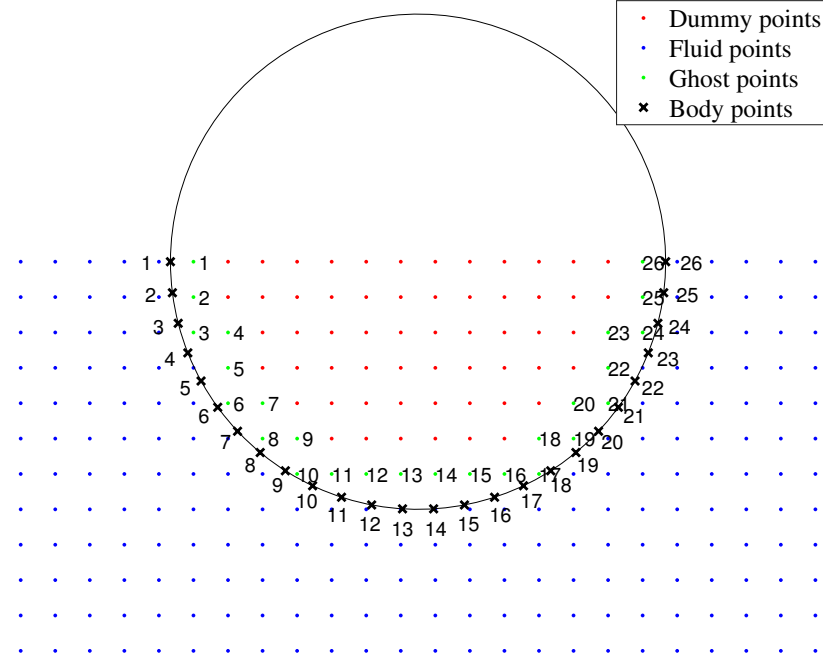


**Figure 3.2:** Updated point classification for the Immersed Boundary Method.

ghost points.

Figure 3.2 shows the distribution of ghost and body points following the new algorithm. Here ghost points are labelled inside the circle, and their corresponding body points are labelled outside the circle. While the distance  $d_{min}$  is somewhat arbitrary, setting it based on the local minimum grid spacing means that the number of body points scales with increasing resolution. Furthermore, the distance may be adjusted in the interests of a finer discretization of the body surface for a given number of grid points, although this has not been investigated in the present work.

### 3.4 Time integration

The fully nonlinear free surface boundary conditions (2.11b) and (2.11c) are time-stepped using an explicit fourth-order, four-stage Runge-Kutta method. This expresses the time derivative of a first-order differential equation

$$\frac{dy(t)}{dt} = f(y, t) \quad (3.7)$$

as

$$y^{n+1} = y^n + \frac{1}{6}k_1 + \frac{1}{3}k_2 + \frac{1}{3}k_3 + \frac{1}{6}k_4, \quad (3.8)$$

where

$$\begin{aligned}
 k1 &= \Delta t f(t^n, y^n) \\
 k2 &= \Delta t f\left(t^n + \frac{\Delta t}{2}, y^n + \frac{k_1}{2}\right) \\
 k3 &= \Delta t f\left(t^n + \frac{\Delta t}{2}, y^n + \frac{k_2}{2}\right) \\
 k4 &= \Delta t f(t^n + \Delta t, y^n + k_3).
 \end{aligned} \tag{3.9}$$

Here the superscript  $n$  denotes the time level. See Iserles (2009) for a more detailed discussion of the method. One important limitation of using a multi-stage time-stepping method in combination with an IBM is that computational points can move into or out of the body between stages. Points that start inside the body have unphysical values, which will introduce errors in the final summation, Eq. (3.8). The current method for dealing with this is as follows:

1. When a free-surface point emerges from the body, its elevation and velocity potential are extrapolated using a stencil of neighbouring fluid points and the body-free-surface intersection point (see Section 3.5 below for a discussion of the intersection point).
2. This value is used normally during the remainder of the Runge-Kutta stages.
3. After the final evaluation of Eq. (3.8), the value of the “new” fluid point is again extrapolated, using the same points described above.

While this may affect the quality of the temporal derivative, the values are extrapolated using stencils at the same order as those used for spatial derivatives.

## 3.5 Body-free-surface intersection point tracking

This section details the implementation of a semi-Lagrangian body-free-surface intersection point into the OW3D solver. As described in the Introduction, this addition has the goal of addressing various problems that arise when combining a  $\sigma$ -transformation of the vertical coordinate, an IBM for modelling structures, and a multi-stage time-stepping method. The main aim of this addition is thus to improve the generation of the artificial interior free surface and to provide a more consistent method for assigning values to new fluid points that emerge from a moving body, thereby improving the robustness of the solver. Section 3.5.1 discusses the motivation for this addition, Section 3.5.2 details the implementation, and Section 3.5.3 presents various test cases. The reader may also refer to the conference paper from the proceedings of the 35th International Conference on Water Waves and Floating Bodies:

*“Incorporating a semi-Lagrangian body-free-surface intersection point in a fully nonlinear potential flow model”*, Jacob Hicks, Harry Bingham, Robert Read, Allan P. Engsig-Karup

### 3.5.1 Motivation

Two key situations have been identified that cause difficulties in simulations, both of which relate to high gradients of the free surface close to the body-free-surface intersection. In the first case, the free surface begins to peel away from the body. This typically occurs when a new fluid

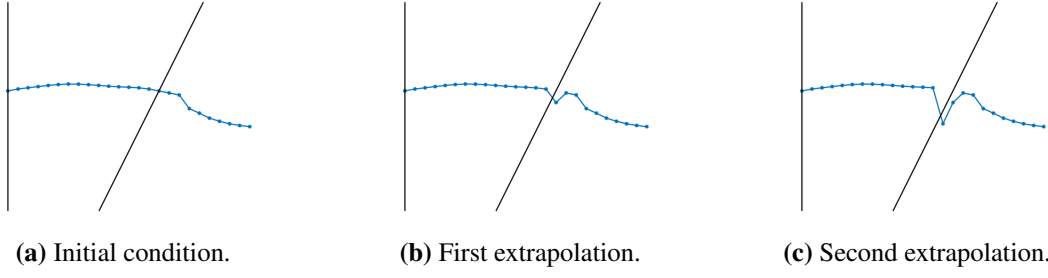


**Figure 3.3:** Free surface peeling away from body, caused when extrapolating a value for a new fluid point based on neighbouring fluid points.

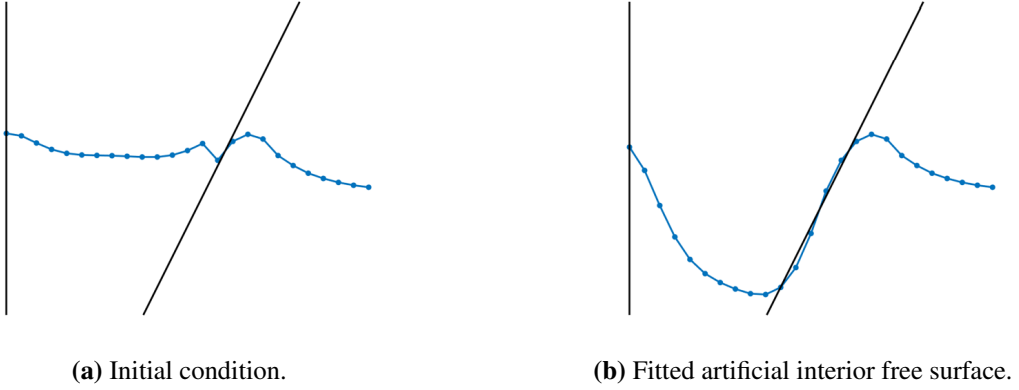


**Figure 3.4:** Artificial interior free surface protruding from the body.

point emerges from the body as it moves through the domain. Extrapolating a value to this new point, using only neighbouring fluid points, leads to it peeling away from the body. In the second case, the artificial interior free surface protrudes from the body. Both cases immediately lead to a breakdown in simulations. Figure 3.3 shows an example of the first case, which occurs when a new computational point emerges from the body. Figure 3.4 shows an example of the second case. Some method of treating these problems is required. One approach is to apply a filter to the free surface, but this essentially removes energy from the wave field which may influence nonlinear interactions. A promising alternative is the introduction of a body-free-surface intersection point.

### 3.5.2 Body-free-surface intersection point

The idea of a semi-Lagrangian intersection point has been formulated in Liu et al. (2001), who specify two criteria that such a point must satisfy at all time steps:

1. It must remain on the body surface.
2. It must remain on the free surface.

The authors suggest that the first condition is satisfied by imposing that the velocity,  $\mathbf{V}_P$ , of an intersection point,  $P$ , be directed along the local tangential direction,  $\mathbf{e}_\tau$ . The second condition is satisfied by calculating the magnitude of  $\mathbf{V}_P$  according to,

$$\mathbf{V}_P = \frac{\nabla \phi_P \cdot \mathbf{n}_{FS}}{\mathbf{e}_\tau \cdot \mathbf{n}_{FS}} \mathbf{e}_\tau, \quad (3.10)$$

where  $\mathbf{n}_{FS}$  is the outward-pointing free surface normal. If the body is in motion,  $\mathbf{V}_P$  may be calculated by

$$\mathbf{V}_P = \frac{(\nabla\phi - \mathbf{U}) \cdot \mathbf{n}_{FS}}{\mathbf{e}_\tau \cdot \mathbf{n}_{FS}} \mathbf{e}_\tau + \mathbf{U}, \quad (3.11)$$

where  $\mathbf{U}$  is the body velocity evaluated at  $P$ . The location of the intersection point is then simply updated by

$$\frac{d\mathbf{x}}{dt} = \mathbf{V}_P. \quad (3.12)$$

The velocity potential at the intersection point is updated by

$$\begin{aligned} \frac{d\phi}{dt} &= \frac{\partial\phi}{\partial t} + \mathbf{V}_P \cdot \nabla\phi \\ &= -g\eta - \frac{1}{2}(\nabla\phi)^2 + \mathbf{V}_P \cdot \nabla\phi, \end{aligned} \quad (3.13)$$

which is the dynamic free surface boundary condition supplemented by an additional term relating to the intersection point velocity. These equations may be included in the Runge-Kutta updating steps, and are evaluated after solving the velocity potential problem at the current time level. When using the intersection point the solution steps are as follows:

1. Solve boundary value problem for  $\phi$ .
2. Time-step the nonlinear free surface boundary conditions.
3. Time-step the position of the body-free-surface intersection point.

For clarity, the intersection point position, velocity, and velocity potential are not *solved for*, but rather *calculated from* the known values of the velocity potential in the fluid and the velocity of the body. This avoids the singularity that would otherwise arise due to the confluence of boundary conditions at the intersection point, as detailed in depth in Greenhow and Lin (1983); Lin et al. (1984); Lin (1984). The flow of information is reciprocal - the fluid and body motion define the position and velocity potential of the intersection point, which is subsequently used for two purposes:

- Between each Runge-Kutta step, the intersection point is used while constructing the artificial interior free surface. This process involves the derivatives at the intersection; knowing the location of the intersection accurately improves the approximation of the derivatives.
- When new free-surface fluid points emerge from the body, their elevation and velocity potential are extrapolated using a combination of the intersection point and neighbouring free surface values.

### 3.5.3 Test cases

#### Piston wavemaker, simple sinusoidal motion

The implementation is first tested on a surging piston wavemaker. Here the fundamental criterion is simply that the point must remain on the wavemaker surface throughout the simulation. The wavemaker is moved by a simple sinusoidal motion, given by

$$X(t) = s \cos(\omega t), \quad (3.14)$$

Dimensionless water depth	$kh$	[-]	2.21	2.22	2.23	2.25	2.27	2.30
Steepness	$H/L$	[-]	0.02	0.03	0.04	0.05	0.06	0.07
Target wave amplitude	$a$	$10^{-2}[\text{m}]$	2.00	3.00	4.00	4.99	5.98	6.96
Stroke amplitude	$s$	$10^{-2}[\text{m}]$	1.13	1.70	2.26	2.81	3.35	3.88

**Table 3.1:** Test cases for paddle motion with body-free-surface intersection point.

with the motion being ramped from zero to full amplitude over two wave periods. The time ramping is given by

$$\gamma(t) = \frac{1}{2} + \frac{1}{2} \tanh\left(10 \frac{t - \frac{t_R}{2}}{t_R}\right), \quad (3.15)$$

where  $t_R = 2T$  in this case. Time ramping is used to avoid an impulsive start, which is problematic both numerically and physically as it can cause jets or wave-breaking at the wavemaker. The full wavemaker motion is thus given by

$$\begin{aligned} X_R(t) &= X(t)\gamma(t) \\ &= s \cos(\omega t) \left( \frac{1}{2} + \frac{1}{2} \tanh\left(10 \frac{t - \frac{t_R}{2}}{t_R}\right) \right). \end{aligned} \quad (3.16)$$

The time ramping must also be included in the wavemaker velocity, which is used to calculate the intersection point velocity in Eq. (3.11). For simple sinusoidal motion this is straightforward;

$$\begin{aligned} U(t) &= X'_R(t) \\ &= X'(t)\gamma(t) + X(t)\gamma'(t) \\ &= -s\omega \sin(\omega t) \cdot \left( \frac{1}{2} + \frac{1}{2} \tanh\left(10 \frac{t - \frac{t_R}{2}}{t_R}\right) \right) + s \cos(\omega t) \cdot \frac{5}{t_R} \left( 1 - \tanh^2\left(10 \frac{t - \frac{t_R}{2}}{t_R}\right) \right). \end{aligned} \quad (3.17)$$

However, if the wavemaker motion consists of  $N$  harmonic cosine components (e.g. Eq. (4.12)), the velocity may be calculated by

$$\begin{aligned} U(t) &= \sum_{i=1}^N \left( -\frac{1}{2} s_i i \omega \sin(\omega_i t + \delta_i) \right) + \dots \\ &\quad \left( -\frac{1}{2} \tanh\left(10 \frac{t - \frac{t_R}{2}}{t_R}\right) s_i i \omega \sin(\omega_i t + \delta_i) \right) + \dots \\ &\quad \left( \frac{5}{t_R} \left( 1 - \tanh\left(10 \frac{t - \frac{t_R}{2}}{t_R}\right)^2 \right) s_i \cos(\omega_i t + \delta_i) \right). \end{aligned} \quad (3.18)$$

Here the index  $i$  refers to each harmonic component, and is not to be mistaken for the imaginary unit.

The test cases are in the intermediate water depth range, and are collected in Table 3.1. No smoothing is applied to the free surface during these simulations, nor is the intersection point artificially "re-attached" to the body surface. A uniform grid of 60 points per wavelength is used in the horizontal direction, with 23 points in the vertical direction. For all cases the stencil size is  $r = 3$ .

Figure 3.5 shows the normal distance from the intersection point to the paddle wavemaker over three wave periods, for each of the cases shown in Table 3.1. While this distance is close to

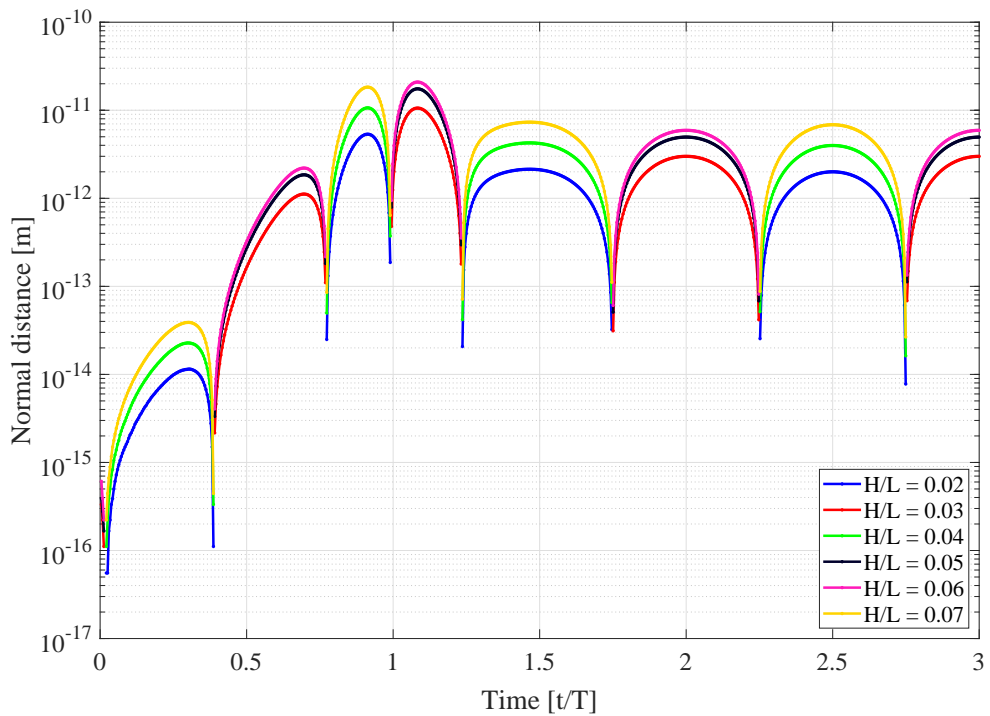


**Figure 3.5:** Normal distance from intersection point to piston wavemaker, for waves of varying steepness.

Water depth $h$ [m]	Wave height $H$ [m]	Wave period $T$ [s]	Wave number $kh$ [-]
0.55	0.05	1.0	2.64

**Table 3.2:** Experimental wave data for surging piston wavemaker.

machine precision for all cases, there is some degree of oscillation following the body position. The reason for this oscillation is unknown. Using the intersection point allows waves of steepness  $H/L \leq 0.07$  to be simulated; without the intersection point this limit is  $H/L \leq 0.06$ . Figure 3.6 shows a comparison of the free surface elevation after three wave periods, with and without using the body-free-surface intersection point, for a wave of  $kh = 2.27$  and  $H/L = 0.06$ . As shown in the figure, when simulating without the intersection point the free surface shows spurious “ripples” or jets close to the wavemaker, leading to extreme gradients that the internal free surface must satisfy.

## Piston wavemaker, experimental data

The implementation is also compared to experimental data obtained at DTU, again for the first-order motion of a surging piston wavemaker. The wave parameters of the case studied are presented in Table 3.2. The desired wavemaker stroke is calculated based on the first-order transfer function of Bi  sel and Suquet (1951a,b). In order to avoid an impulsive start, as before, the control signal is gradually increased from zero to maximum amplitude over five wave periods. During the experiments the wavemaker position is measured, and this time series is used as input to the OW3D simulations. This ensures that any deviations in the experimental control signal are reproduced in

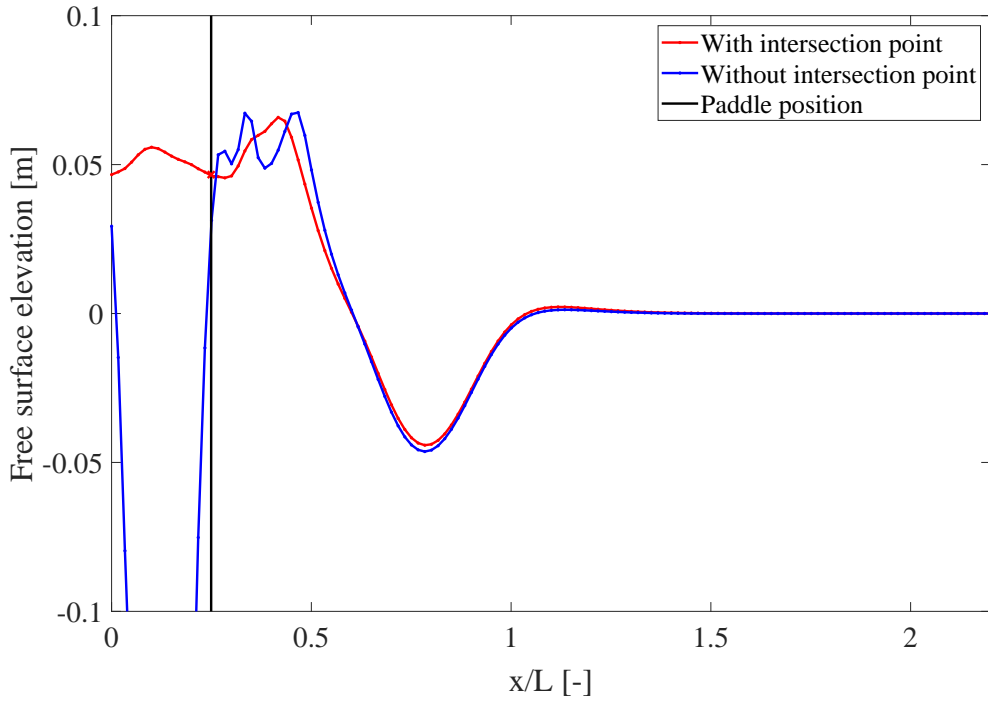


**Figure 3.6:** Comparison of free surface elevation after three wave periods, with and without the body-free-surface intersection point. The simulation case is a surging paddle wavemaker, with  $kh = 2.27$  and  $H/L = 0.06$ .

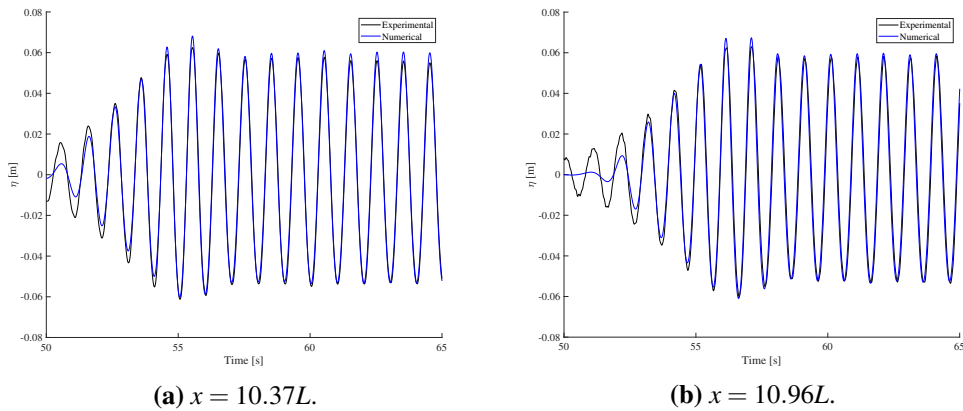


**Figure 3.7:** Comparison of wave generated by simple sinusoidal paddle motion,  $kh = 2.64$ .

the numerical simulations. As the body motion is defined discretely, the velocity is approximated by differentiation of the discrete motion signal using second-order finite-difference stencils.

The experimental free surface elevation is measured at various points in the wave tank by parallel-wire resistance wave gauges. Figure 3.7 shows a comparison of the time series of the free surface elevation at two locations. The numerical data compares favourably to the experimental data, matching the initial surge in amplitude even after many wavelengths.

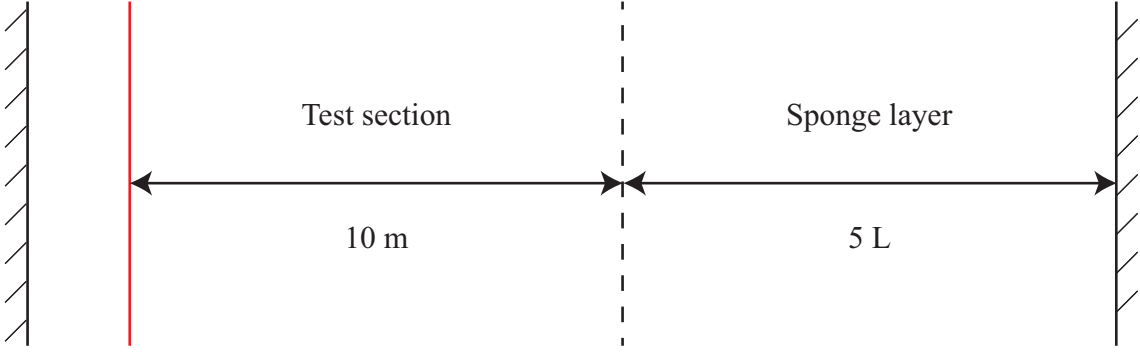


**Figure 3.8:** Schematic of numerical domain with piston wavemaker. Wavemaker marked in red.

### Comparison with Schäffer's second-order wavemaker theory

Numerical simulations using the intersection point are also compared with the second-order wavemaker theory of Schäffer (1996). Eq. (2.14) forms the basis of the numerical comparison with second-order theory. As with the simple sinusoidal motion, the wavemaker motion is gradually ramped up from zero to maximum amplitude. Given that the motion is now defined by the second-order theory; i.e.

$$X_R(t) = \left( \frac{1}{2} \left\{ -iX_a e^{i\omega t} + c.c. \right\} + \frac{1}{2} \left\{ -i\mathcal{F}^\pm \frac{A_n A_m^{-*}}{h} e^{i(\omega_n \pm \omega_m)t} + c.c. \right\} \right) \left( \frac{1}{2} + \frac{1}{2} \tanh \left( 10 \frac{t - \frac{t_R}{2}}{t_R} \right) \right) \quad (3.19)$$

the body velocity is thus given by

$$U(t) = \Re \left( -iA e^{i\omega t} - i \frac{A^2}{h} \mathcal{F}^+ e^{2i\omega t} \right) \frac{5}{t_R} \left( 1 - \tanh \left( 10 \frac{t - \frac{t_R}{2}}{t_R} \right) \right)^2 + \dots \\ \Re \left( \omega A e^{i\omega t} + 2\omega \frac{A^2}{h} \mathcal{F}^+ e^{2i\omega t} \right) \left( \frac{1}{2} + \frac{1}{2} \tanh \left( 10 \frac{t - \frac{t_R}{2}}{t_R} \right) \right), \quad (3.20)$$

where

$$A = \frac{h}{2} \left( \sqrt{1 + 2 \frac{H}{h}} - 1 \right). \quad (3.21)$$

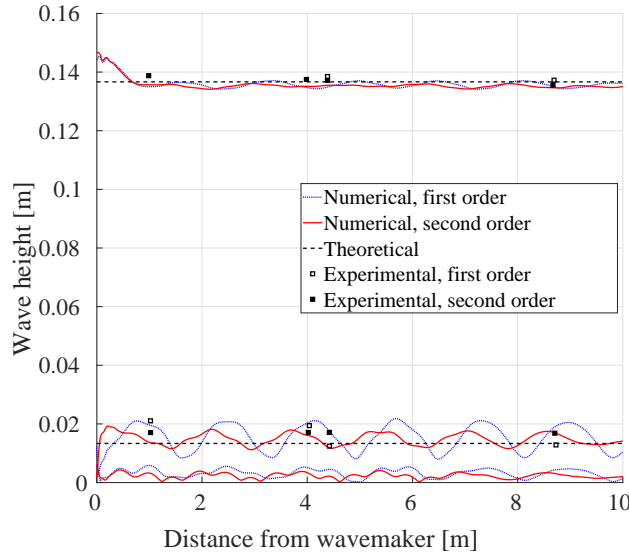
Here  $h$  is the water depth, and  $H$  the wave height.

Three cases are tested, with relevant characteristics described in Table 3.3. These cases cover shallow to intermediate depths, which is where piston wavemakers are expected to perform best. Two simulations are carried out for each set of characteristics: one using a first-order wavemaker control signal, and one using a second-order control signal. Figure 3.8 shows a schematic of the domain used in the numerical simulations. The gap between the wavemaker and left boundary is changed for each case based on the magnitude of the wavemaker stroke. As the artificial interior free surface is a 7th-order polynomial, the mean position of the wavemaker is set to ensure that there are sufficient interior points at the extremum of the stroke.

While the sponge layer is effective in absorbing the propagating wave, simulations are stopped before any reflection can return to the test section, as this would contaminate the results. The simulations are carried out with a stencil size of  $r = 3$  and a horizontal resolution of 60 points per wavelength, using a uniform grid in both the horizontal and vertical directions.

The results are presented in Figures 3.9, 3.10, and 3.11. These figures show a harmonic analysis across the test section, as described in Section 2.2.2, where the third harmonic is included. The

Water depth $h$ [m]	Period $T$ [s]	Wave height $H$ [m]	Wave number $kh$ [-]
0.7	1.2	0.15	2.03
0.7	1.5	0.155	1.41
0.7	2.0	0.12	0.95

**Table 3.3:** Comparison cases for second-order wave generation.**Figure 3.9:** Comparison of first- and second-order wave generation, for  $kh = 2.03$ . Experimental values from Schäffer (1996).

theoretical values correspond to  $A$  and  $A^2/h$ , and the experimental values are taken from Figure 10 of Schäffer (1996). The shallower cases, shown in Figures 3.10 and 3.11, show good agreement with the theoretical solutions, and a significant difference between first and second-order control signals. The first-order control signal produces a clear unbound second harmonic, evident by the oscillation of the second harmonic amplitude across the test section. In both cases, the third-order harmonic appears to be bound to the second-order harmonic, both of which are in anti-phase with the first-order harmonic. Using the second-order control signal shows a marked improvement, with both the first- and second-order harmonics being relatively stable across the test section. These results generally agree with the experimental data, although the poor resolution of the latter, and lack of error bars in the experimental measurements, preclude any conclusive comparisons.

### Heaving cylinder

A similar set of tests with simple sinusoidal motion are carried out for a heaving cylinder. In these cases, the dimensionless dispersion parameter is kept constant, at  $kh = 4.50$ , and the motion amplitude is increased from  $A = 0.01R$  to  $A = 0.09R$ , with  $R = 1$  being the cylinder radius. The cylinder is positioned in the centre of the domain, with a uniform grid of 60 points per wavelength close to the cylinder gradually stretching to 40 points per wavelength at the boundaries. The domain is shown in Figure 3.12. In these cases there are two intersection points; both are updated

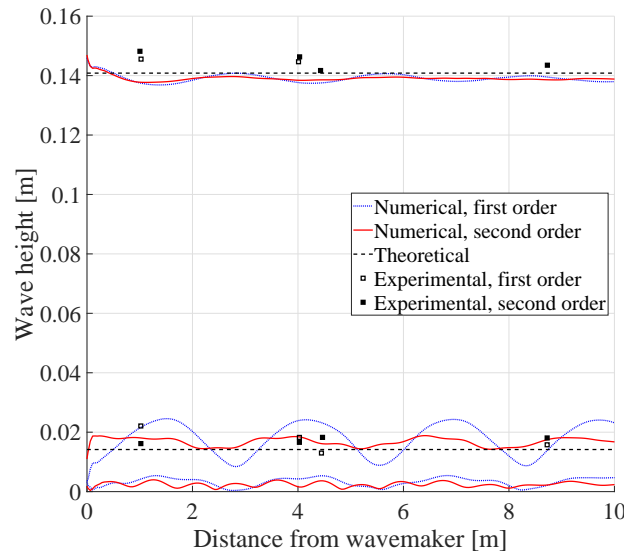


**Figure 3.10:** Comparison of first- and second-order wave generation, for  $kh = 1.41$ . Experimental values from Schäffer (1996).

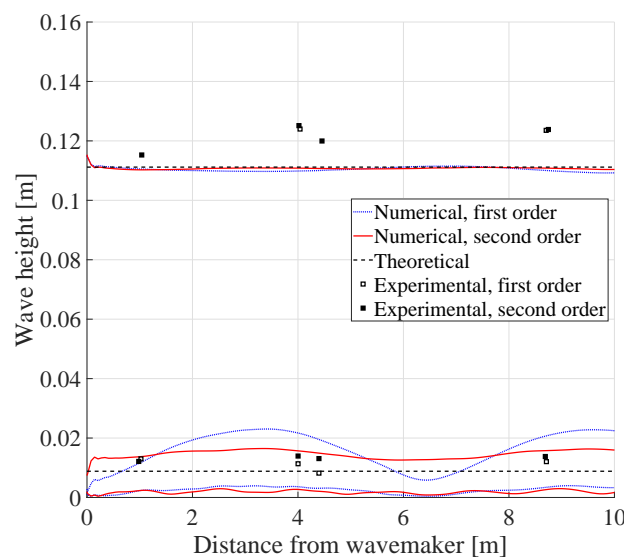


**Figure 3.11:** Comparison of first- and second-order wave generation, for  $kh = 0.95$ . Experimental values from Schäffer (1996).

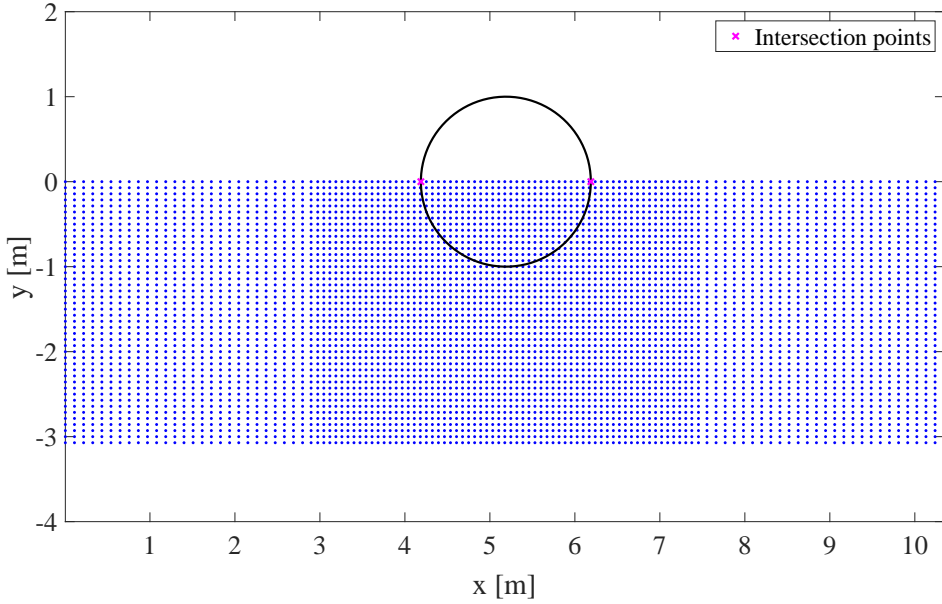


**Figure 3.12:** Numerical domain for heaving cylinder simulations.

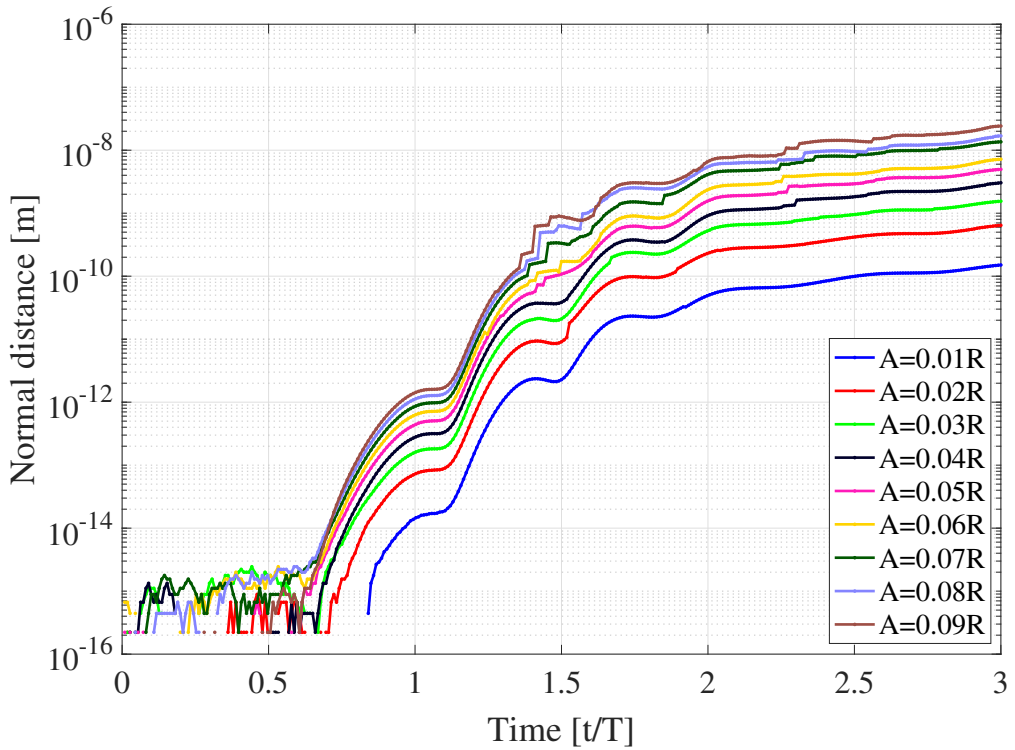
in the manner outlined above.

Figure 3.13 shows the normal distance from the intersection points to the cylinder over three wave periods. Here the points gradually detach from the body surface. For large-amplitude motion the simulations eventually break down, although this is primarily due to jets forming at the intersection point.

### 3.5.4 Concluding remarks

A semi-Lagrangian body-free-surface intersection point has been implemented in the OW3D solver, following the formulation of Liu et al. (2001). Testing with a surging piston wavemaker showed satisfactory agreement between both experimental and theoretical solutions. However, simulating small-amplitude motions of a heaving cylinder showed that the semi-Lagrangian point gradually detaches from the body. This may be due to the formulation of the intersection point velocity given by Liu et al. (2001), where the velocity vector is projected onto the local body surface tangent,  $\mathbf{e}_\tau$ . While this may be sufficient when simulating small body motions, or when the local body curvature is sufficiently small; in the general case this does not in fact ensure that the point remains on the body surface. Re-attaching the intersection point whenever its distance from the body exceeds some tolerance is one possible way forward; preliminary testing with the cylinder appears to support this approach. This is, however, unsatisfactory, as the method is rather ad-hoc. Another alternative is to recast Eq. (3.12) in curvilinear coordinates following the body surface. This should effectively constrain the intersection point to the body surface.

However, the problems that the intersection point is supposed to solve may be due to unavoidable physical factors. Experimental observations have shown that some wave breaking begins to occur directly at the wavemaker, even when the far-field waves corresponding to the wavemaker



**Figure 3.13:** Normal distance from intersection point to heaving cylinder, for motion of increasing amplitude.

motion are below the breaking limit. As a pure potential flow solver, OW3D is not equipped to deal with wave breaking, so the cases studied here may be the upper limit in terms of wave steepness that can be simulated. The addition of a wave-breaking model would therefore be very pertinent for further research. This could initially take the form of a selective filter that activates when vertical particle velocities exceed some limiting factor.

## 3.6 Nonlinear wave loads and free-body motion

This section presents an extension to the OW3D solver that both improves calculation of nonlinear wave loads and allows for simulation of free-body motion.

### 3.6.1 Formulation

The OW3D solver is extended to include free-body motion by adapting the method presented in Tanizawa (1995), parts of which are included here for clarity. The central idea of Tanizawa (1995) is to couple Euler's equation of ideal fluid motion with the equation of solid body motions, ensuring equilibrium of forces between the ideal fluid and solid body at all times. This is done by introducing Prandtl's nonlinear acceleration potential, defined as

$$\Phi = \phi_t + \frac{1}{2}(\nabla\phi)^2. \quad (3.22)$$

As with the velocity potential, the acceleration potential must satisfy an equivalent kinematic boundary condition on the body surface, namely

$$\frac{\partial \Phi}{\partial n} = \mathbf{n} \cdot \nabla \Phi = \mathbf{n} \cdot \mathbf{a}. \quad (3.23)$$

Here  $\mathbf{a}$  denotes the acceleration of a fluid particle sliding on the body surface, and  $\mathbf{n}$  denotes the unit normal vector of the body surface. In a space-fixed reference frame, the kinematic body boundary condition becomes

$$\begin{aligned} \frac{\partial \Phi}{\partial n} = & \mathbf{n} \cdot (\mathbf{a}_0 + \dot{\boldsymbol{\omega}} \times \mathbf{r}) + \mathbf{n} \cdot \boldsymbol{\omega} \times (\boldsymbol{\omega} \times \mathbf{r}) \\ & - k_n (\nabla \phi - \mathbf{v}_0 - \boldsymbol{\omega} \times \mathbf{r})^2 + \\ & \mathbf{n} \cdot 2\boldsymbol{\omega} \times (\nabla \phi - \mathbf{v}_0 - \boldsymbol{\omega} \times \mathbf{r}), \end{aligned} \quad (3.24)$$

where  $\mathbf{a}_0$  is the translational acceleration of the body,  $\boldsymbol{\omega}$  is the angular velocity of the body,  $\mathbf{r}$  is the vector from the body centre of gravity to the fluid point sliding on the body surface, and  $\mathbf{v}_0$  is the translational velocity of the body. As the body translational and angular acceleration,  $\mathbf{a}_0$  and  $\dot{\boldsymbol{\omega}}$  respectively, are unknown before the acceleration field is solved, the equation of body motion is used to eliminate the unknown body accelerations from Eq. (3.24). Using generalized values for the body inertia tensor  $\mathbf{M}_{ij}$ , acceleration  $\boldsymbol{\alpha}_j$ , and force  $\mathbf{F}_i$ , the equation of body motion is given by

$$\mathbf{M}_{ij} \boldsymbol{\alpha}_j + \boldsymbol{\beta}_j = \mathbf{F}_i, \quad (3.25)$$

where  $\boldsymbol{\beta}_i$  appears because the body reference frame has angular velocity. The generalized acceleration is defined as

$$\boldsymbol{\alpha}_i = \begin{bmatrix} a_{0x} \\ a_{0y} \\ a_{0z} \\ \dot{\omega}_x \\ \dot{\omega}_y \\ \dot{\omega}_z \end{bmatrix}, \quad (3.26)$$

and  $\boldsymbol{\beta}_i$  is defined as

$$\boldsymbol{\beta}_i = \begin{bmatrix} 0 \\ 0 \\ 0 \\ (I_{zz} - I_{yy})\omega_y\omega_z - I_{xy}\omega_z\omega_x + I_{zx}\omega_x\omega_y + I_{yz}(\omega_y^2 - \omega_z^2) \\ (I_{xx} - I_{zz})\omega_z\omega_x - I_{yz}\omega_x\omega_y + I_{xy}\omega_y\omega_z + I_{zx}(\omega_z^2 - \omega_x^2) \\ (I_{yy} - I_{xx})\omega_x\omega_y - I_{zx}\omega_y\omega_z + I_{yz}\omega_z\omega_x + I_{xy}(\omega_x^2 - \omega_y^2) \end{bmatrix}, \quad (3.27)$$

where  $I_{ij}$  are components of the inertia tensor and  $\omega_i$  the corresponding angular frequencies. Working non-dimensionally, with the fluid density and gravitational acceleration set to  $\rho = 1$  and  $g = 1$ , respectively, the generalized hydraulic force acting on the body is given by

$$\mathbf{F}_i^f = \int_{S_B} (-\Phi - Z) \mathbf{N}_i ds, \quad (3.28)$$

where  $Z$  is the vertical coordinate, being zero on the mean free surface, and  $\mathbf{N}_i$  is the generalized normal vector, defined as

$$\begin{aligned}\mathbf{N}_i &= (\mathbf{n}, \mathbf{n} \times \mathbf{r}) \\ &= (n_x \mathbf{i} + n_y \mathbf{j} + n_z \mathbf{k}, \\ &\quad (n_y z - n_z y) \mathbf{i} + (n_z x - n_x z) \mathbf{j} + (n_x y - n_y x) \mathbf{k}).\end{aligned}\tag{3.29}$$

Including other forces acting on the body (gravity, thrust etc.) as  $\mathbf{F}_i^g$ , the generalized total force acting on the body is given by

$$\mathbf{F}_i = \mathbf{F}_i^f + \mathbf{F}_i^g = \int_{S_B} (-\Phi - Z) \mathbf{N}_i ds + \mathbf{F}_i^g,\tag{3.30}$$

Combining Eq. (3.30) with Eq. (3.25) gives the generalized Euler's equation of three dimensional body motions coupled with fluid motion; namely

$$\mathbf{M}_{ij} \boldsymbol{\alpha}_j + \boldsymbol{\beta}_j = \int_{S_B} (-\Phi - Z) \mathbf{N}_i ds + \mathbf{F}_i^g.\tag{3.31}$$

Using the generalized values, Eq. (3.24) is rewritten as

$$\frac{\partial \Phi}{\partial n} = \mathbf{N}_i \cdot \boldsymbol{\alpha}_i + q,\tag{3.32}$$

where  $q$  represents the values that can be calculated from the known velocity potential field; i.e.

$$\begin{aligned}q &= \mathbf{n} \cdot \boldsymbol{\omega} \times (\boldsymbol{\omega} \times \mathbf{r}) \\ &\quad - k_n (\nabla \phi - \mathbf{v}_0 - \boldsymbol{\omega} \times \mathbf{r})^2 + \\ &\quad \mathbf{n} \cdot 2\boldsymbol{\omega} \times (\nabla \phi - \mathbf{v}_0 - \boldsymbol{\omega} \times \mathbf{r}).\end{aligned}\tag{3.33}$$

The generalized acceleration is eliminated by substitution of Eq. (3.31) into Eq. (3.32)

$$\frac{\partial \Phi}{\partial n} = \mathbf{N}_i \cdot \mathbf{M}_{ij}^{-1} \left\{ \int_{S_B} (-\Phi - Z) \mathbf{N}_j ds + \mathbf{F}_i^g - \boldsymbol{\beta}_j \right\} + q.\tag{3.34}$$

Splitting the integral term of the right-hand side gives

$$\begin{aligned}\frac{\partial \Phi}{\partial n} &= \mathbf{N}_i \cdot \mathbf{M}_{ij}^{-1} \int_{S_B} -\Phi \mathbf{N}_j ds \\ &\quad + \mathbf{N}_j \cdot \mathbf{M}_{ij}^{-1} \left\{ \int_{S_B} -Z \mathbf{N}_i ds + \mathbf{F}_i^g - \boldsymbol{\beta}_j \right\} + q.\end{aligned}\tag{3.35}$$

This is the key result of Tanizawa (1995): an implicit boundary condition giving the relationship between the acceleration potential and its flux on the body surface. As the acceleration potential does not satisfy Laplace's equation (due to the nonlinear velocity potential term), Eq. (3.35) is rewritten by substituting Eq. 3.22, giving

$$\begin{aligned}\frac{\partial \phi_t}{\partial n} &= \mathbf{N}_i \mathbf{M}_{ij}^{-1} \int_{S_B} -\phi_t \mathbf{N}_i ds \\ &\quad + \mathbf{N}_i \mathbf{M}_{ij}^{-1} \left\{ \int_{S_B} \left( -Z - \frac{1}{2} (\nabla \phi)^2 \right) \mathbf{N}_i ds + \mathbf{F}_g - \boldsymbol{\beta}_i \right\} \\ &\quad + q - \frac{\partial}{\partial n} \left( \frac{1}{2} (\nabla \phi)^2 \right).\end{aligned}\tag{3.36}$$

This is coupled with the dynamic free surface boundary condition for  $\phi_t$ ,

$$\phi_t = -Z - \frac{1}{2}(\nabla\phi)^2. \quad (3.37)$$

Finally, with homogeneous Neumann conditions at the other domain boundaries, and the Laplace equation throughout the domain, the boundary value problem for  $\phi_t$  is fully defined.

### 3.6.2 Implementation in OW3D

Tanizawa's method is adapted to the OW3D solver by rewriting the implicit body boundary condition Eq. (3.36) so that the integral of  $\phi_t$  over the body surface is expressed as a series of matrix-vector operations. In matrix notation, Eq. (3.36) can be written as

$$\mathbf{A}_N\phi_t = \mathbf{A}_I\phi_t + b. \quad (3.38)$$

Here  $\mathbf{A}_N$  is a matrix operator that approximates the normal derivative on the body, the Laplace equation throughout the domain, and the appropriate boundary conditions on the free surface and domain boundaries. This is the same operator that is used to solve the velocity potential problem. The operator  $\mathbf{A}_I$  is the ‘integration matrix’, defined as

$$\mathbf{A}_I\phi_t = \mathbf{NM}^{-1} \int_{S_B} -\phi_t \mathbf{N} ds. \quad (3.39)$$

The variable  $b$  in Eq. (3.38) represents the remaining values from Eq. (3.36), which can be calculated from the known velocity potential field. The goal is to collect the implicit terms of Eq. (3.36) into a single matrix operator acting on  $\phi_t$ , such that the system can be solved directly,

$$\phi_t = (\mathbf{A}_N - \mathbf{A}_I)^{-1}b. \quad (3.40)$$

Having solved for  $\phi_t$ , the full acceleration potential  $\Phi$  can be computed from Eq. (3.22). This is then used to solve for the generalized body acceleration  $\boldsymbol{\alpha}$  by

$$\boldsymbol{\alpha} = \mathbf{M}^{-1} \left[ \int_{S_B} (-\Phi - Z) \mathbf{N} ds + \mathbf{F}^g - \boldsymbol{\beta} \right]. \quad (3.41)$$

This information is included in the time-stepping right-hand-side as part of the Runge-Kutta procedure. The Runge-Kutta solution vector  $f(t)$ , which normally holds the values of the free-surface elevation and velocity potential, is extended to include the body position and velocity,

$$f(t) = \begin{bmatrix} \eta(t) \\ \phi(t) \\ \gamma(t) \end{bmatrix}, \quad (3.42)$$

where  $\gamma(t)$  holds the body position and velocity. Describing the generalized body position by  $\mathbf{B}_X$  and velocity by  $\mathbf{B}_V$ ,  $\gamma(t)$  has the form

$$\gamma(t) = \begin{bmatrix} \mathbf{B}_X \\ \mathbf{B}_V. \end{bmatrix} \quad (3.43)$$

These variables are time-stepped by

$$\frac{d}{dt} \begin{bmatrix} \mathbf{B}_X \\ \mathbf{B}_V \end{bmatrix} = \begin{bmatrix} \mathbf{B}_V \\ \boldsymbol{\alpha} \end{bmatrix}, \quad (3.44)$$

where  $\boldsymbol{\alpha}$  is the solution to Eq. (3.41). Finally, in terms of program flow, the acceleration potential problem is solved after time-stepping the free-surface variables. So, for a given Runge-Kutta stage, the solution proceeds as

1. Solve the boundary value problem for  $\phi$ .
2. Calculate the time-stepping right-hand-side for the free-surface variables,  $\eta_t$  and  $\phi_t$ .
3. Solve the acceleration potential problem.
4. Calculate the time-stepping right-hand-side for the body position and velocity.
5. Update the intersection point/s.
6. Construct the artificial interior free surface.

As the acceleration potential problem is solved after calculating the time-stepping right-hand-side of the free-surface variables, the free surface boundary condition in the acceleration potential problem, given by Eq. (3.37), is replaced by the newly-calculated time-stepping value for  $\phi_t$  on the free surface.

The following sub-sections will detail the creation of the new integration matrix  $\mathbf{A}_I$ .

### Integration by matrix-vector product

The essential idea is to use Taylor integration to approximate the integral of  $\phi_t$  along the body surface. Given the classic Taylor series expansion

$$f(x) = \sum_{n=0}^{r-1} \frac{(x-x_0)^n}{n!} f_0^{(n)} + O(r), \quad (3.45)$$

where  $r$  is the size of the finite difference stencil,  $x$  is the evaluation point and  $x_0$  is the expansion point, integrating both sides gives

$$\int f(x) dx = \int \left( \sum_{n=0}^{r-1} \frac{(x-x_0)^n}{n!} f_0^{(n)} \right) dx + \int O(r) dx \quad (3.46)$$

$$= \sum_{n=0}^{r-1} \frac{(x-x_0)^{n+1}}{(n+1)n!} f_0^{(n)} + O(r+1) \quad (3.47)$$

$$= \sum_{n=0}^{r-1} \frac{(x-x_0)^{n+1}}{(n+1)!} f_0^{(n)} + O(r+1). \quad (3.48)$$

As the leading-order error term is proportional to  $(x-x_0)^{r+1}$ , this method is  $O(r+1)$  accurate so long as  $f_0^{(n)}$  are known exactly. Otherwise, the order of accuracy is determined by the method used to approximate  $f_0^{(n)}$ . To put Eq. (3.46) into the context of the body surface, the integral over a given segment of the body, running from  $s_j$  to  $s_{j+1}$  with arc length  $ds_j$ , may be approximated by a sum of the derivatives of the function values evaluated at  $s_j$ , so that

$$\int_{s_j}^{s_{j+1}} f(s) ds = \sum_{n=0}^{r-1} \frac{ds_j^{n+1}}{(n+1)!} f_j^{(n)}. \quad (3.49)$$

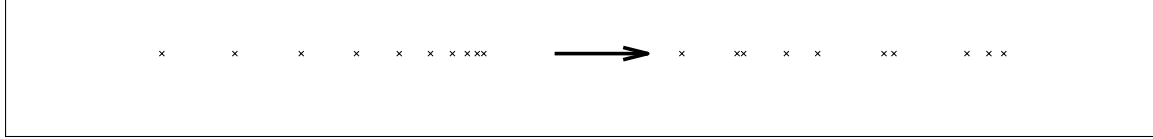


**Figure 3.14:** Random grid generation in 1D.

For  $n_p$  body points, the total integral is evaluated by summing the  $n_p - 1$  contributions

$$\int_{S_B} f(s) ds = \sum_{j=1}^{n_p-1} \sum_{n=0}^{r-1} \frac{ds_j^{n+1}}{(n+1)!} f_j^{(n)}. \quad (3.50)$$

In matrix notation, the right-hand side of Eq. (3.50) can be written as a set of matrix-vector products

$$\int_{S_B} f(s) ds = \vec{\mathbf{1}} \mathbf{A}_T \vec{f}, \quad (3.51)$$

where  $\vec{\mathbf{1}}$  denotes a row vector of  $n_p - 1$  ones, i.e.  $\vec{\mathbf{1}} = [1 \ 1 \ \dots \ 1]$ , which act as the outer summation of Eq. (3.50),  $\mathbf{A}_T$  is a matrix of finite-difference operators corresponding to the inner summation of Eq. (3.50), and  $\vec{f}$  is a column vector of the values to be integrated. The combined operator  $\vec{\mathbf{1}} \mathbf{A}_T$  will subsequently be referred to as the integration vector, denoted by  $\mathbf{I}_V$ .

### Test case: 1D

A simple case is set up to test the procedure with known function values. As mentioned in Section 3.3, the initial method for distributing body points in the IBM resulted in quasi-random spacing. To emulate this, a 1D set of points with random non-uniform spacing is generated on the interval  $x \in [0, \pi]$ , by first generating a stretched grid with the function

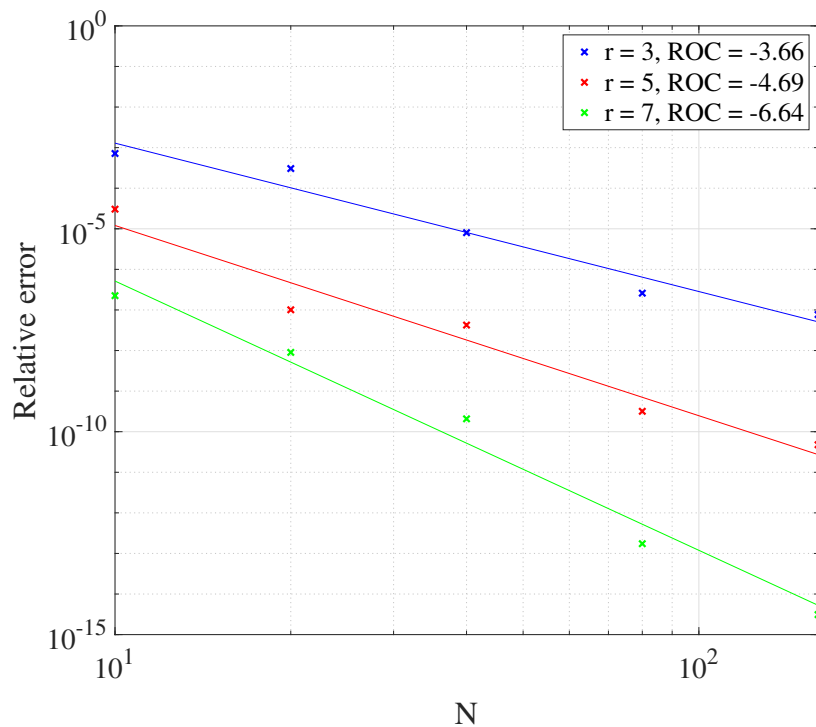
$$x_G = \frac{\tanh(\alpha x)}{\tanh(\alpha)}, \quad (3.52)$$

where  $x$  is a grid of uniformly distributed points and  $\alpha$  is a stretching factor ( $\alpha = 1$  corresponds to a uniform grid). The grid spacings  $\Delta x_G$  are then randomly shuffled and  $x_G$  is rebuilt. This procedure is visualized in Figure 3.14. The test function  $\sin(x)$  is integrated along  $x_G$ , with the analytic target

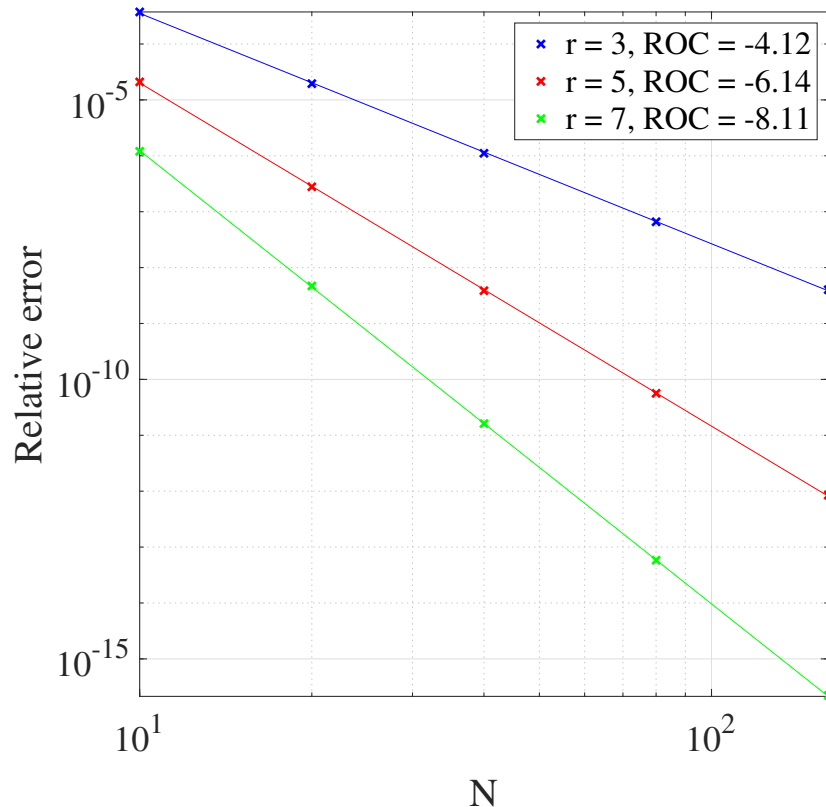
$$\int_0^\pi \sin(x) dx = 2. \quad (3.53)$$

Figure 3.15 shows the convergence of the 1D integration operator for various stencil sizes when using a random distribution of body points. While generally between  $O(r)$  and  $O(r - 1)$ , it falls short of the expected  $O(r + 1)$ . As mentioned in Section 3.3, this is thought to be due to large differences in arc lengths between body points, essentially leading to a poorly-conditioned integration matrix.

The situation is improved when using a uniform distribution of points, as shown in Figure 3.16. Here each stencil size shows convergence at  $O(r + 1)$ , as expected from the theory. This finding led to the updated procedure for allocating ghost and body points, as described in Section 3.3.



**Figure 3.15:** Convergence of integration by matrix-vector product in 1D for various stencil sizes, using random distribution of body points.



**Figure 3.16:** Convergence of integration by matrix-vector product in 1D for various stencil sizes, using uniform distribution of body points.

## Integration and interpolation

In general, the function values on the body are not known a priori, and so are approximated by an interpolation matrix. Such a matrix will subsequently be referred to as  $\mathbf{D}_0$ , where the subscript 0 denotes interpolation of the zeroth derivative. Each row in the interpolation matrix contains a stencil of Weighted Least Squares coefficients that approximate the function value on the body based on neighbouring points. The order of approximation of this method is  $p \geq r - a$ , as detailed in Kontos (2016), where  $a$  is the function derivative to be approximated. For this case  $a = 0$ , so the interpolation matrix is at least of order  $r$ . Expanding the matrix integration procedure to two dimensions requires a combination of the integration vector  $\mathbf{I}_V$  and interpolation matrix  $\mathbf{D}_0$ , and Eq. (3.51) becomes

$$\int_{S_B} f(s) ds = \mathbf{I}_V \mathbf{D}_0 \vec{f}, \quad (3.54)$$

where  $\vec{f}$  is now a vector of field points.

### Test case: 2D

Another simple case is created to test the procedure with known values. A uniform grid is set up with  $n_x$  points in the horizontal and  $n_y$  points in the vertical. A cylindrical body is placed at some arbitrary position, either fully or partially submerged, and a set of  $n_p$  body points is defined on the body surface. Finally, the integral of a field function over the submerged surface is evaluated. For this test case, the function  $f(x, y) = xy^4$  is defined throughout the domain, with the analytic target

$$\begin{aligned} \int_{S_B} xy^4 dS = & \left[ xy^4 \theta + Ry^3 (y \sin(\theta) - 4x \cos(\theta)) + \right. \\ & R^2 y^2 (3x(-\cos(\theta) \sin(\theta) + \theta) - 2y \cos(\theta)^2) + R^3 y \left( 2y \sin(\theta)^3 - \frac{4}{3} x \cos(\theta) (2 + \sin(\theta)^2) \right) + \\ & \left. R^4 \left( y \sin(\theta)^4 + x \left( -\frac{1}{4} \cos(\theta) \left( \sin(\theta)^3 + \frac{3}{2} \sin(\theta) \right) + \frac{3}{8} \theta \right) \right) + R^5 \frac{\sin(\theta)^5}{5} \right]_{\theta_1}^{\theta_2}. \end{aligned} \quad (3.55)$$

Here,  $\theta$  corresponds to the limits of integration. For a cylinder at rest on a flat free surface,  $\theta_1 = -\pi$  and  $\theta_2 = 0$ . Figure 3.17 shows the convergence for various stencil sizes.

### Full implicit representation

Having established the convergence of the integration procedure in both 1D and 2D, the full implicit body boundary condition, Eq. (3.36), can now be implemented in matrix-vector form so that  $\mathbf{A}_N \phi_t = \mathbf{A}_I \phi_t + b$ . As mentioned previously, the operator  $\mathbf{A}_N$  is the same as that used when solving for the velocity potential problem, so what remains is to build  $\mathbf{A}_I$  such that it has the same dimensions as  $\mathbf{A}_N$ , and evaluate the remaining terms based on  $\phi$ . Recall that  $\mathbf{A}_I$  has been defined in Eq. (3.39) as

$$\mathbf{A}_I \phi_t = \mathbf{NM}^{-1} \int_{S_B} -\phi_t \mathbf{N} ds,$$

and the previous section showed in Eq. (3.54) that

$$\int_{S_B} f(s) ds = \mathbf{I}_V \mathbf{D}_0 \vec{f}.$$

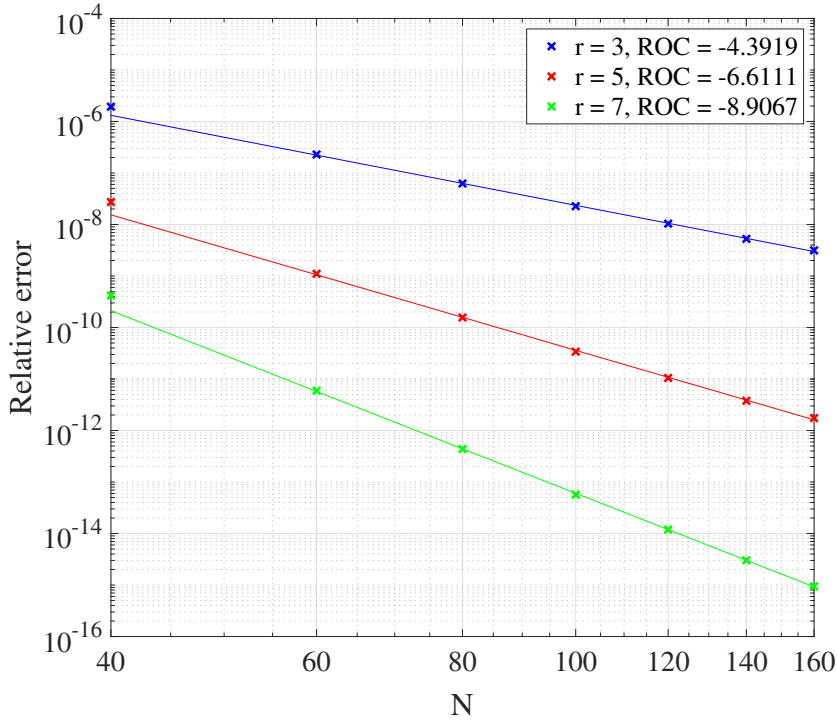


**Figure 3.17:** Convergence of integration by matrix-vector product in 2D, for various stencil sizes.

The next step is to include the generalized normal vector  $\mathbf{N}$  and body inertia tensor  $\mathbf{M}$ . While  $\mathbf{M}$  refers to the body center of mass, and is the same for all body points,  $\mathbf{N}$  refers to each body point;  $\mathbf{N} = \mathbf{N}_i$  for  $i = 1, 2, \dots, n_p$ . In the general case  $\mathbf{N}$  will have six components at each body point: the translatory surge, heave, and sway; and the rotational roll, yaw, and pitch. This results in six integrals, one for each component. In practice, the components of the generalized normal vector are included in the integrand by modifying the interpolation matrix. Each row of coefficients (corresponding to a given body point) is multiplied by the corresponding generalized normal component at that body point. Combining Eq. (3.39) with Eq. (3.54) and expanding:

$$\mathbf{A}_I \phi_t = \begin{bmatrix} n_x & n_y & n_z & \omega_x & \omega_y & \omega_z \end{bmatrix} \begin{bmatrix} m & 0 & 0 & 0 & 0 & 0 \\ 0 & m & 0 & 0 & 0 & 0 \\ 0 & 0 & m & 0 & 0 & 0 \\ 0 & 0 & 0 & I_{xx} & I_{xy} & I_{xz} \\ 0 & 0 & 0 & I_{yx} & I_{yy} & I_{yz} \\ 0 & 0 & 0 & I_{zx} & I_{zy} & I_{zz} \end{bmatrix}^{-1} \begin{bmatrix} \mathbf{I}_V \mathbf{D}_0 \cdot n_x \\ \mathbf{I}_V \mathbf{D}_0 \cdot n_y \\ \mathbf{I}_V \mathbf{D}_0 \cdot n_z \\ \mathbf{I}_V \mathbf{D}_0 \cdot \omega_x \\ \mathbf{I}_V \mathbf{D}_0 \cdot \omega_y \\ \mathbf{I}_V \mathbf{D}_0 \cdot \omega_z \end{bmatrix} \phi_t. \quad (3.56)$$

Here  $m$  is the body mass, and  $I_{ij}$  denotes the moments of inertia. Given a domain of  $N_x \times N_y$  points, and a body with  $n_p$  points along its surface, the products  $\mathbf{I}_V \mathbf{D}_0 \cdot n_x$ ,  $\mathbf{I}_V \mathbf{D}_0 \cdot n_y$  etc. each produce a row vector of dimensions  $1 \times N_x N_y$ . The remaining operations result in a row vector of dimensions  $1 \times N_x N_y$  for each body point. As the body points are defined by the normal projection of each ghost point onto the body surface, the sparse  $N_x N_y \times N_x N_y$  matrix  $\mathbf{A}_I$  is built by inserting each row of  $1 \times N_x N_y$  coefficients into the corresponding ghost point row. Finally, the matrix  $\mathbf{A}_I$  is subtracted from the original system matrix  $\mathbf{A}_N$ , producing an implicit operator that imposes Tanizawa's body

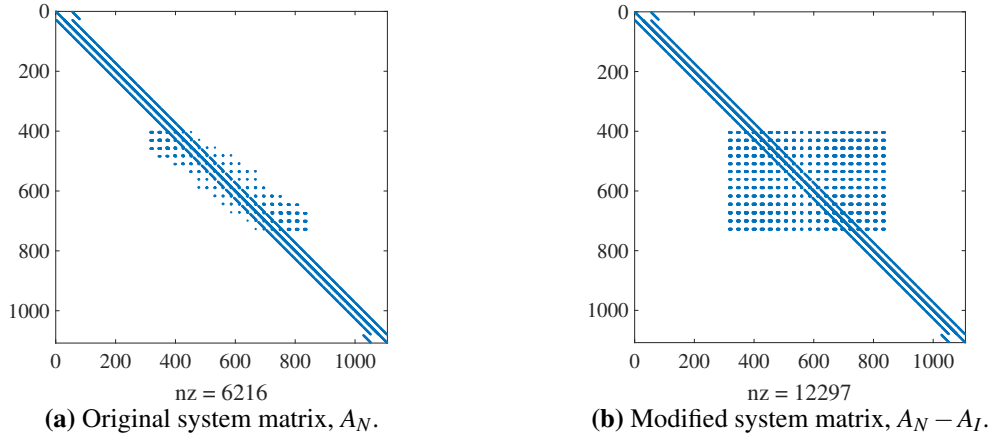


**Figure 3.18:** System matrix before and after modification for implicit integration.

boundary condition for the acceleration potential. The structure of the final matrix is shown in Figure 3.18, for a small problem.

### Right-hand side terms

The remaining terms in Eq. (3.36) can all be evaluated from the known body position, velocity, angular velocity, and velocity potential. The integral term,

$$\mathbf{NM}^{-1} \left\{ \int_{S_B} \left( -Z - \frac{1}{2}(\nabla\phi)^2 \right) \mathbf{N} ds + \mathbf{F}^g - \boldsymbol{\beta} \right\}, \quad (3.57)$$

is evaluated using the same procedure as with the implicit term, namely integration by matrix-vector product. The  $q$  term is calculated from Eq. (3.33). The final term presents some problems when the gradient of the velocity potential is very small, as the solution becomes very sensitive to truncation errors in the derivative operators. Expanding the term gives

$$\frac{\partial}{\partial n} \left( \frac{1}{2}(\nabla\phi)^2 \right) = \frac{1}{2} \left[ \frac{\partial}{\partial x} \left( \left( \frac{\partial\phi}{\partial x} \right)^2 + \left( \frac{\partial\phi}{\partial y} \right)^2 \right) \cdot n_x + \frac{\partial}{\partial y} \left( \left( \frac{\partial\phi}{\partial x} \right)^2 + \left( \frac{\partial\phi}{\partial y} \right)^2 \right) \cdot n_y \right] \quad (3.58)$$

$$\frac{\partial}{\partial n} \left( \frac{1}{2}(\nabla\phi)^2 \right) = \frac{1}{2} \left[ \frac{\partial}{\partial x} (\phi_x^2 + \phi_y^2) \cdot n_x + \frac{\partial}{\partial y} (\phi_x^2 + \phi_y^2) \cdot n_y \right]. \quad (3.59)$$

To remedy this, the procedure outlined in Appendix A of Tanizawa (1995) is implemented, and the end result is included here for clarity. Essentially the gradient of the velocity potential is recast into partial tangential derivatives:

$$\frac{\partial}{\partial n} \left( \frac{1}{2}(\nabla\phi)^2 \right) = -k_n(\nabla\phi)^2 + \frac{\partial\phi}{\partial n} \left( -\frac{\partial^2\phi}{\partial s^2} \right) + \frac{\partial\phi}{\partial s} \frac{\partial}{\partial s} \left( \frac{\partial\phi}{\partial n} \right). \quad (3.60)$$

Here  $k_n$  is the normal curvature of the body, as before, and  $\partial/\partial s$  denotes the partial derivative in the tangential direction. The difference between using the tangential and normal formulations is illustrated in Figures 3.19 and 3.20, for a submerged surging dipole with a stencil size of  $r = 3$ .

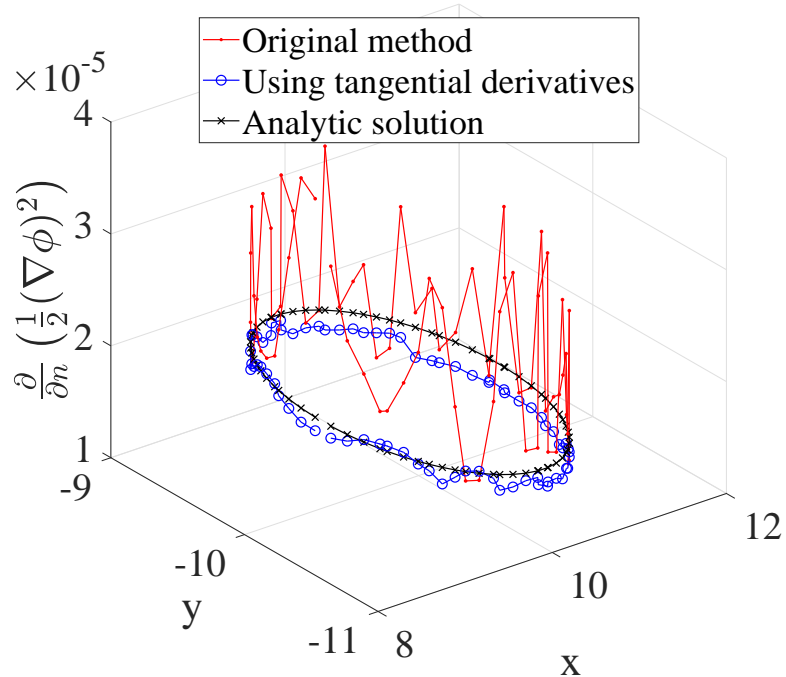


**Figure 3.19:** Normal and tangential formulations for evaluating  $\frac{\partial}{\partial n} \left( \frac{1}{2} (\nabla \phi)^2 \right)$ .

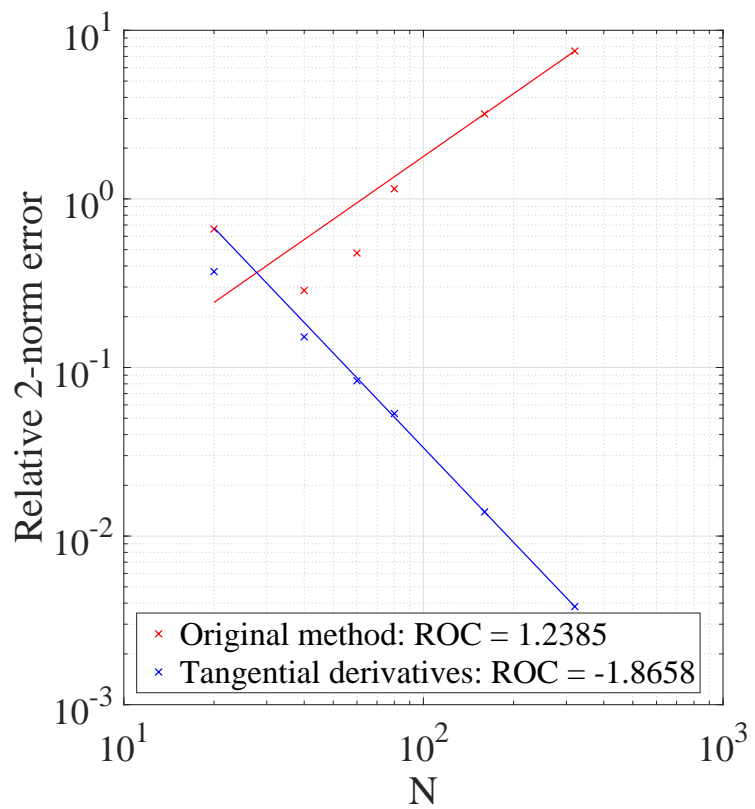


**Figure 3.20:** Convergence of  $\frac{\partial}{\partial n} \left( \frac{1}{2} (\nabla \phi)^2 \right)$ .

## 4 | Stable waves of constant form using harmonic optimisation

Parts of the work described in this chapter appear in the following article submitted to the journal Applied Ocean Research:

“*Nonlinear Wave Generation Using a Heaving Wedge*” Jacob B. H. Hicks, Harry B. Bingham, Robert W. Read, Allan P. Engsig-Karup.

### 4.1 Solver validation

As described previously, the OW3D solver has already been validated against various test cases for forced motion of heaving cylinders and wedges (Kontos (2016)). To further confirm this validation, specifically in the context of wave generation, numerical simulations are compared with both theoretical and experimental data concerning wavemaker theory. The first-order wavemaker theory of Wu (1988) is used when considering a heaving wedge wavemaker, and the second-order wavemaker theory of Schäffer (1996) is used when considering a surging paddle wavemaker. Numerical simulations for both a heaving wedge and surging paddle are subsequently compared against experimental data obtained at DTU.

#### 4.1.1 Comparison with Wu’s first-order wavemaker theory

The first-order theory of Wu (1988) uses a Boundary Collocation Method (BCM) to calculate the transfer function for heaving-wedge wavemaker motion. Figure 4.1 shows this transfer function, as a function of the dimensionless wave number  $kh$ . A series of small amplitude waves at various wave numbers are simulated, with each case having a steepness of  $H/L = 1\%$ . For a given far-field wave amplitude, the wavemaker stroke is calculated from the first-order transfer function shown in Figure 4.1. The error is then calculated by comparing the numerical far-field wave amplitude with its theoretical counterpart.

$$\xi = \frac{a_N - a_T}{a_T}, \quad (4.1)$$

where subscripts  $N$  and  $T$  refer to numerical and theoretical wave amplitudes, respectively. The results of these simulations are collected in Table 4.1. All but the shortest waves have relative errors of less than 1%.

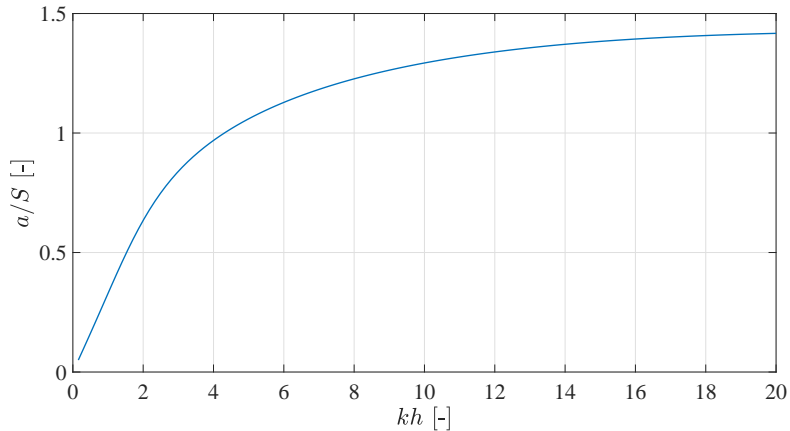


**Figure 4.1:** The first-order transfer function of Wu (1988), as a function of the dimensionless wave number  $kh$ .

$kh$	[ - ]	1.96	2.60	3.26	4.56	5.86	6.50	7.14	7.80
$T$	[ s ]	1.18	1.01	0.90	0.76	0.67	0.63	0.60	0.58
$\xi$	[ - ]	0.0039	0.0063	0.0070	0.0044	0.0039	0.0055	0.0080	0.011

**Table 4.1:** Comparison with first-order wavemaker theory:  $kh$  denotes dimensional wave number;  $T$  denotes wave period;  $\xi$  denotes relative error. All waves have steepness  $H/L = 1\%$ .

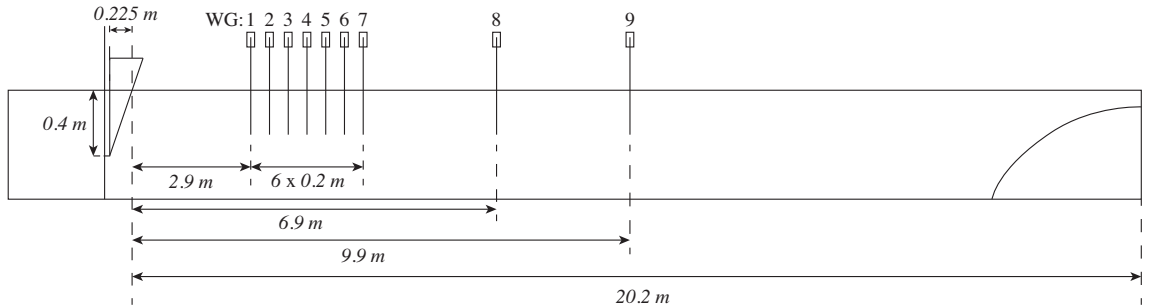


**Figure 4.2:** Experimental setup for wedge wavemaker experiments. WG denotes wave gauge.

#### 4.1.2 Comparison with experimental data

The previous section showed that OW3D is capable of modelling the wave fields generated by first- and second-order wavemaker control signals, with simulations comparing favourably to theoretical solutions. In this section, numerical simulations of wave generation by a heaving wedge wavemaker are compared to experimental data obtained at DTU.

A schematic of the experimental setup is shown in Figure 4.2. In its mean position the wedge has a draft of 0.4 m, with a beam of  $b = 0.225$  m at the still water line. The water depth is set to  $h = 0.65$  m. The mean draft of the wedge ensures that it remains partially submerged for all wave cases. The parallel-wire resistance wave gauges shown in Figure 4.2 are used to measure the free surface elevation at various points in the tank. A beach at the far end of the wave tank absorbs propagating waves and reduces reflection. As a further precaution, experiments are terminated before the energy of the generated wave could return to the final wave gauge. This time limit is

$kh$	[ - ]	1.90	2.21	2.33	2.33	2.41	2.72	3.98
$H/L$	[ % ]	2.39	2.41	3.48	6.00	2.40	7.99	3.96
$T$	[ s ]	1.20	1.10	1.07	1.07	1.05	0.99	0.81
$\xi_2$	[ - ]	0.052	0.023	0.019	0.051	0.040	0.045	0.046
$\xi_{RMS}$	[ - ]	0.040	0.011	0.035	0.034	0.014	0.023	0.070

**Table 4.2:** Experimental comparison for heaving wedge wavemaker.  $\xi_2$  denotes relative 2-norm error with respect to experimentally measured amplitudes.  $\xi_{RMS}$  denotes Root Mean Square error with respect to experimentally measured free surface elevation.

calculated based on the group velocity, and may be expressed as

$$\begin{aligned} t_{MAX} &= \frac{x}{V_G} \\ &= \frac{20.2 \text{ m} + (20.2 - 9.9) \text{ m}}{V_G} = \frac{30.5 \text{ m}}{V_G}, \end{aligned} \quad (4.2)$$

where  $V_G$  is the group velocity of the propagating wave, given by

$$V_G = \left( \frac{1}{2} + \frac{kh}{\sinh(2kh)} \right) V_P, \quad (4.3)$$

and  $V_P = \omega/k$  is the phase velocity.

The experimental cases are collected in Table 4.2, comprising a series of waves in the intermediate to deep water regimes with varying degrees of nonlinearity. Two error metrics are considered; namely comparison of the fundamental harmonic amplitudes at each wave gauge, and direct comparison to the free surface elevation. The error in the former is described by

$$\xi = \frac{\|a_N - a_E\|_2}{\|a_E\|_2}, \quad (4.4)$$

where the subscripts  $N$  and  $E$  refer to the numerical and experimental fundamental wave amplitude measured at each wave gauge, respectively, and  $\|- \|_2$  refers to the 2-norm. When comparing numerical and experimental free surface elevations directly, the error is described by

$$\xi_{RMS} = \frac{1}{H_E} \sqrt{\frac{1}{T_s} \int_0^{T_s} (\eta_N(t) - \eta_E(t))^2 dt}, \quad (4.5)$$

where  $H_E$  is the measured experimental wave height, and  $T_s$  is the sampling window. This is the Root Mean Square (RMS) error relative to the desired wave height.

Both error metrics are generally below 5%, indicating that the OW3D solver is capable of capturing both linear and nonlinear aspects of waves generated by a moving boundary.

## 4.2 Optimization procedure

With favourable comparisons to both theoretical and experimental data for wave generation, the next step is to implement an optimization procedure that can be applied to any type of wavemaker. The general process for achieving a given wave field is as follows:

1. A desired wave field is specified, being characterized by a wavelength, steepness, and number of harmonic components.

2. The harmonic wave amplitudes describing the wave field are calculated based on the Stream Function theory of Fenton (1988).
3. An initial estimate of wavemaker stroke amplitudes is made using an appropriate transfer function.
4. The numerical simulation is carried out, and measured harmonic amplitudes are compared to the desired amplitudes.
5. The wavemaker stroke is updated by the optimization algorithm, and the process is repeated until convergence is achieved.

### 4.2.1 Amplitude optimization

Denoting the desired wave field as

$$\eta(t) = \sum_{i=1}^N a_i \cos(\omega_i t), \quad (4.6)$$

where  $a_i$  are the harmonic amplitudes calculated from Stream Function theory, an initial estimate for the wavemaker stroke is found by

$$X(t) = \sum_{i=1}^N \left( \frac{s}{a} \right)_i a_i \cos(\omega_i t), \quad (4.7)$$

where the fraction  $(s/a)_i$  denotes the transfer function corresponding to the  $i$ -th harmonic. The optimization routine then proceeds by a simple defect correction scheme, where the  $i$ -th harmonic stroke amplitude is updated by

$$s_i^{n+1} = s_i^n + \alpha \left( \frac{s}{a} \right)_i |a_i^{SF} - a_i^{max}|. \quad (4.8)$$

Here the superscript  $n$  denotes the iteration level,  $\alpha$  is a sign function,  $a_i^{SF}$  is the desired stream function  $i$ -th harmonic amplitude, and  $a_i^{max}$  is the maximum value of the generated wave amplitude in the test section. The sign function  $\alpha$  is given by  $\alpha = \text{sign}(a_i^{SF} - \bar{a}_i)$ , where  $\bar{a}_i$  is the average value of the  $i$ -th harmonic amplitude across the test section. The procedure is conceptually similar to that described in Hansen and Svendsen (1975), but is based on a Numerical Wave Tank (NWT) as opposed to an experimental one and can in principle be applied to an arbitrary number of harmonic components.

The optimization procedure is initially applied to a heaving wedge wavemaker, using two harmonic components. The wavemaker control signal is therefore given by

$$X(t) = s_1 \cos(\omega t) + s_2 \cos(2\omega t), \quad (4.9)$$

where the goal of the amplitude optimization procedure is to modify  $s_1$  and  $s_2$  such that spurious free wave components are suppressed. The control signal may thus be considered to be second-order, with a superharmonic second-order component. The algorithm given by Eq. (4.8) is applied to waves in the intermediate to deep water regime, as described in Table 4.3.

The results of the optimization procedure are shown in Figure 4.3, which shows the relative mean error in the first and second harmonic amplitudes for each case. Here the error in the  $i$ -th harmonic amplitude is calculated as

$$\xi_i = \frac{\bar{a}_i - a_i^{SF}}{a_i^{SF}}, \quad (4.10)$$

Wave number <i>kh</i> [-]	Wave height <i>H</i> [m]	Wave period <i>T</i> [s]	Wave steepness <i>H/L</i> [-]
2.04	0.060	1.15	0.03
2.04	0.080	1.14	0.04
2.04	0.120	1.13	0.06
2.33	0.052	1.06	0.03
2.33	0.070	1.06	0.04
2.33	0.088	1.06	0.05
2.33	0.105	1.05	0.06
2.33	0.123	1.04	0.07
2.72	0.045	0.98	0.03
2.72	0.060	0.98	0.04
2.72	0.075	0.97	0.05
2.72	0.090	0.97	0.06
3.27	0.037	0.89	0.03
3.27	0.050	0.89	0.04
3.27	0.063	0.88	0.05
3.27	0.075	0.88	0.06
4.08	0.030	0.80	0.03
4.08	0.040	0.79	0.04
4.08	0.050	0.79	0.05
4.08	0.060	0.79	0.06
4.08	0.070	0.78	0.07
5.45	0.022	0.69	0.03
5.45	0.030	0.69	0.04
5.45	0.038	0.68	0.05
5.45	0.045	0.68	0.06
5.45	0.053	0.68	0.07
8.17	0.015	0.56	0.03
8.17	0.020	0.56	0.04
8.17	0.025	0.56	0.05
8.17	0.030	0.56	0.06
8.17	0.035	0.55	0.07

**Table 4.3:** Optimization cases for heaving wedge wavemaker.

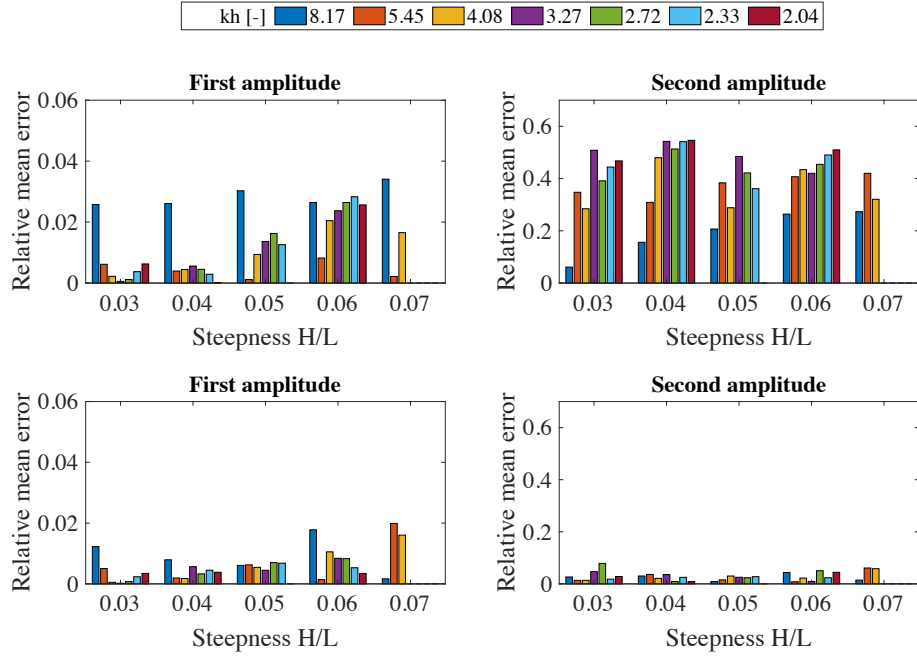


**Figure 4.3:** Relative mean errors before (above) and after (below) optimization. Arranged by wave steepness and coloured by dimensionless dispersion parameter  $kh$ .

where  $\bar{a}$  denotes the mean of the measured numerical wave amplitudes across the test section, and the superscript  $SF$  denotes the target amplitudes calculated from Stream Function theory. As shown in the figure, this mean error is below 2% in all cases for the first harmonic component, and below 10% for the second harmonic. ‘‘Before optimization’’ refers to waves produced by the initial wavemaker control signal, based solely on the first-order transfer function of Wu (1988).

Figure 4.4 shows the degree of variation of each harmonic amplitude across the test section. The variation in the test section is quantified as

$$\kappa_i = \frac{a_i^{max} - \bar{a}_i}{\bar{a}_i}, \quad (4.11)$$

where  $a_i^{max}$  is the maximum value of the  $i$ -th harmonic in the test section. As discussed previously, a perfectly stable wave will show zero variation in its harmonic amplitudes. While this is not exactly the case here, the optimization procedure significantly reduces the degree of variation in both harmonic components. This is visualized in Figure 4.5, which shows the result of a harmonic analysis across the full computational domain for increasing wave steepness, before and after amplitude optimization.

The RMS error in the free surface elevation is evaluated as described in Eq. (4.5), and is shown in Figure 4.6. As can be expected, the low steepness cases show a relatively small error even before optimization, as these are close to linear. After optimization, however, the errors are reduced to approximately 5% for all cases.

The general trend in the optimized stroke amplitudes is that the first harmonic increases slightly, while the second harmonic decreases significantly. The degree of increase and decrease, respectively, is larger as wave steepness increases.

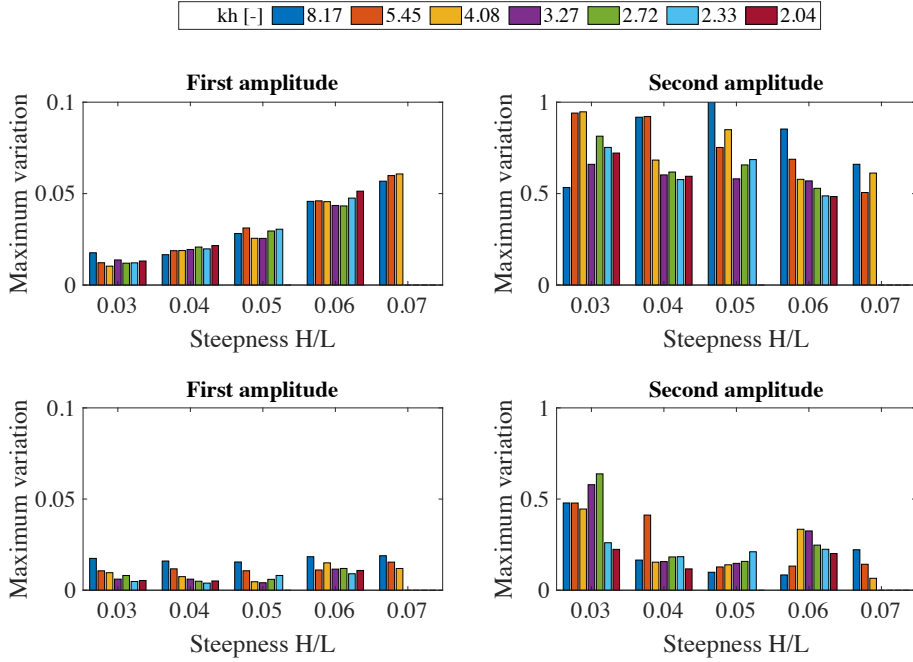


**Figure 4.4:** Amplitude variation across test section before (above) and after (below) optimization. Arranged by wave steepness and coloured by dimensionless dispersion parameter  $kh$ .

Finally, the effect of the optimization procedure is shown in Figure 4.7, which compares the free surface elevation at three locations in the numerical wave tank before and after amplitude optimization. The effect of spurious free waves is clear in Figure 4.7a, as the free surface elevation varies considerably between locations. After just two optimization iterations the situation is much improved, as shown in Figure 4.7b.

In conclusion, the results presented in this section have shown that a relatively simple defect correction scheme, applied solely to the second harmonic amplitude, can quickly improve the quality of waves generated by a heaving wedge wavemaker. Both the relative error with respect to the target harmonic amplitudes, and the variation of the harmonic amplitudes across the test section, are significantly reduced.

## 4.2.2 Phase optimization

The wavemaker stroke is initially made up of harmonics with no phase difference. However, as the second-order transfer function developed by Schäffer (1996) is complex, it contains both magnitude and phase information concerning the second-order addition to the control signal. The harmonic wavemaker stroke presented in Eq. (4.9) may easily be extended to include phase components, as

$$X(t) = \sum_{i=1}^N \left( \frac{s}{a} \right)_i a_i \cos(\omega_i t + \delta_i), \quad (4.12)$$

where  $\delta_i$  represents the phase of the  $i$ -th harmonic relative to the first harmonic. The combined effect of amplitude and phase variations is investigated for several cases with a heaving wedge wavemaker, covering waves in the intermediate and deep water regimes, and weak to “medium”

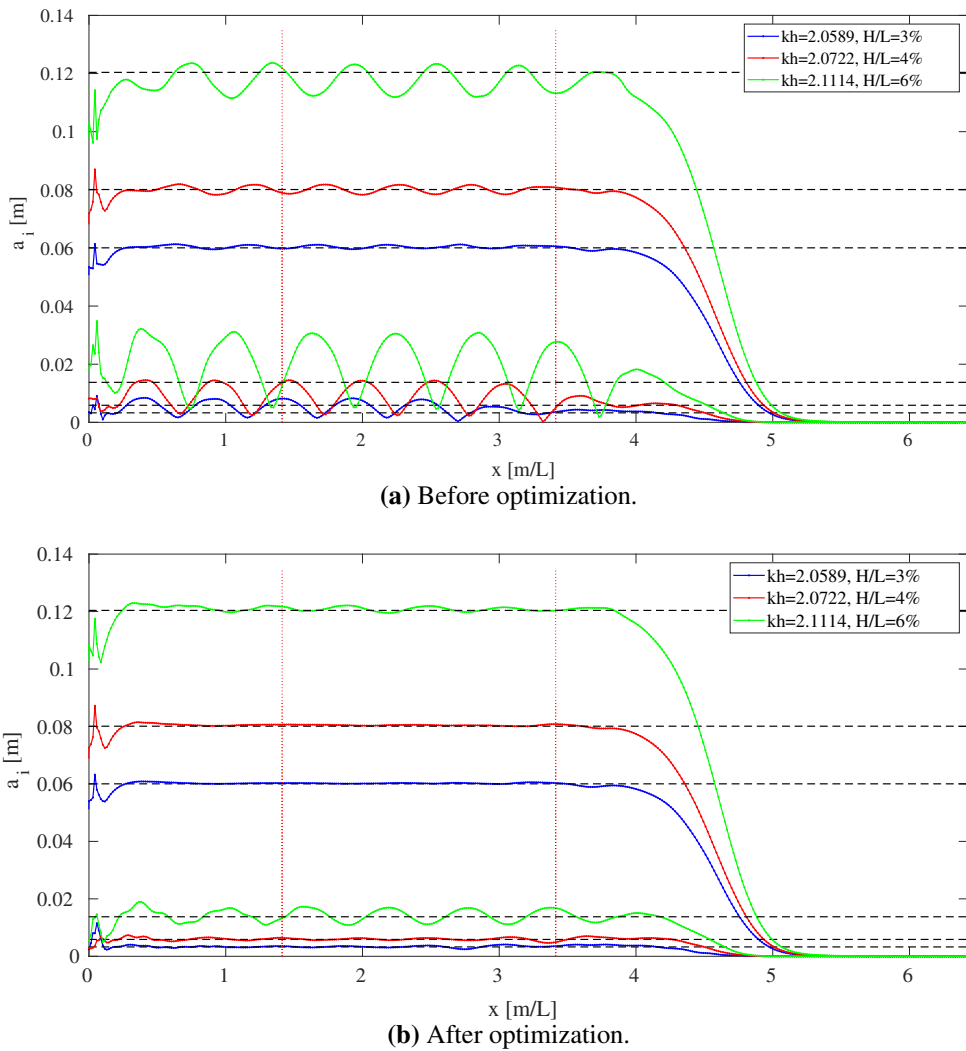


**Figure 4.5:** Harmonic analysis of waves generated before and after amplitude optimization.

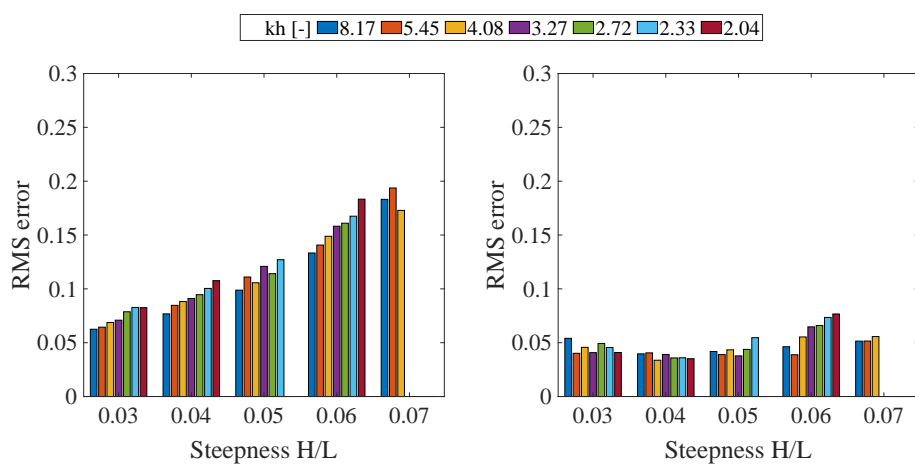


**Figure 4.6:** Relative Root Mean Square (RMS) error in numerical free surface elevation before (left) and after (right) optimization. Arranged by wave steepness and coloured by dimensionless dispersion parameter  $kh$ .

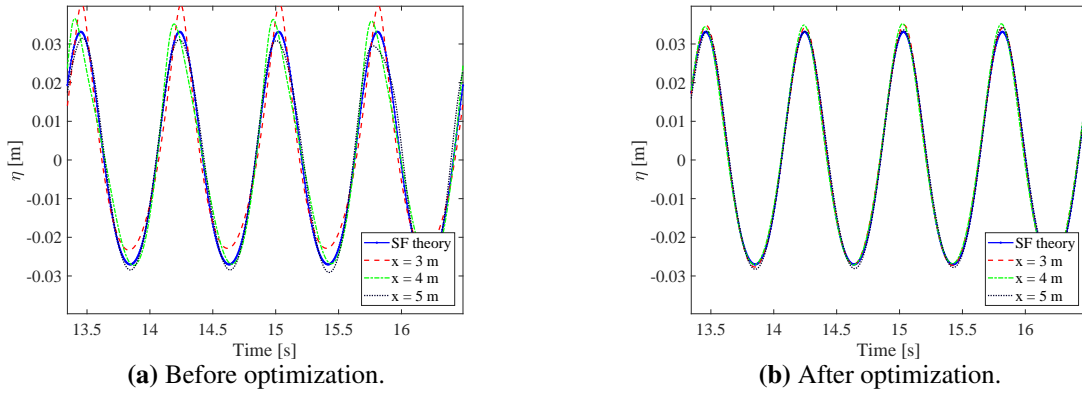


**Figure 4.7:** Free surface elevation at various locations, with and without optimization. Target wave has dimensionless dispersion parameter  $kh = 4.08$  and steepness  $H/L = 6\%$ .

nonlinearity. For each case, the error metrics of interest are the mean error in the harmonic amplitudes across the test section, and the degree of variation in these amplitudes. As before, these are evaluated by Eq. (4.10) and Eq. (4.11). As for the amplitude optimization cases already described in Section 4.2.1, an initial estimate of the wavemaker stroke is calculated based on the first-order transfer function of Bi  sel and Suquet (1951a,b). The magnitude of the second harmonic component,  $s_2$  is then varied between 10-100% of its original value, and the phase of the second harmonic component is varied between 0 and  $2\pi$ . To facilitate comparisons between cases, the amplitudes are subsequently normalized by the maximum value in each case.

Figure 4.8 shows the relative mean errors in the first and second harmonics for a wave of length  $L = 1.75$  m. While the trend in the first harmonic error surface is similar across steepness, the error in the second harmonic appears to change between  $H/L = 4\%$  and  $H/L = 5\%$ . This may be due to nonlinear effects.

Similarly, Figure 4.9 shows the maximum relative variation across the test section in the first and second harmonic amplitudes. Here the trends are consistent across steepness for both harmonics. However, the position of minimum variation does not coincide with the position of minimum error.

Figure 4.10 shows the error surfaces for various values of the dimensionless dispersion parameter  $kh$ , given a constant wave steepness of  $H/L = 4\%$ . Here the key difference appears to be when moving from intermediate to deep water - the shape of the error surface changes significantly between  $kh = 4.08$  and  $kh = 2.72$ .

Finally, Figure 4.11 shows the maximum relative variation across the test section of the first and second harmonic amplitudes. Again the position of minimum variation changes significantly when moving from deep to intermediate water depths - in deep water, the second harmonic amplitude should decrease slightly to reduce variation, while in intermediate water depths, it should decrease significantly.

Ultimately, this analysis has shown that the position of minimum error and/or minimum variation changes both in terms of the dispersion parameter and steepness of the wave being generated. Unfortunately this precludes the possibility of building a surrogate model that could be used across many test cases. Furthermore, as the wave steepness increases, there does not appear to be a global

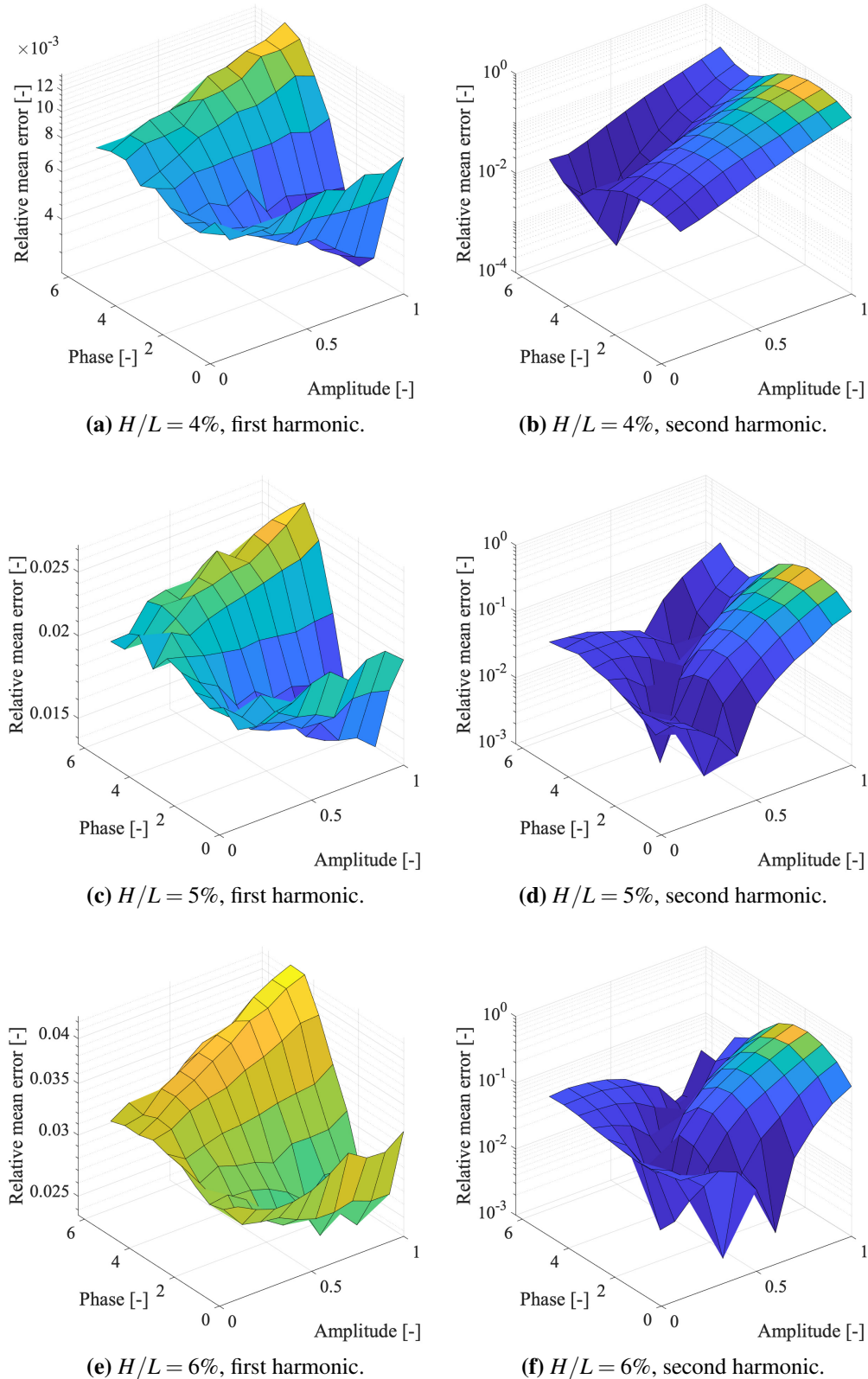


**Figure 4.8:** Relative mean error in first and second harmonics as function of second harmonic amplitude and phase, for waves of  $kh = 2.33$ .

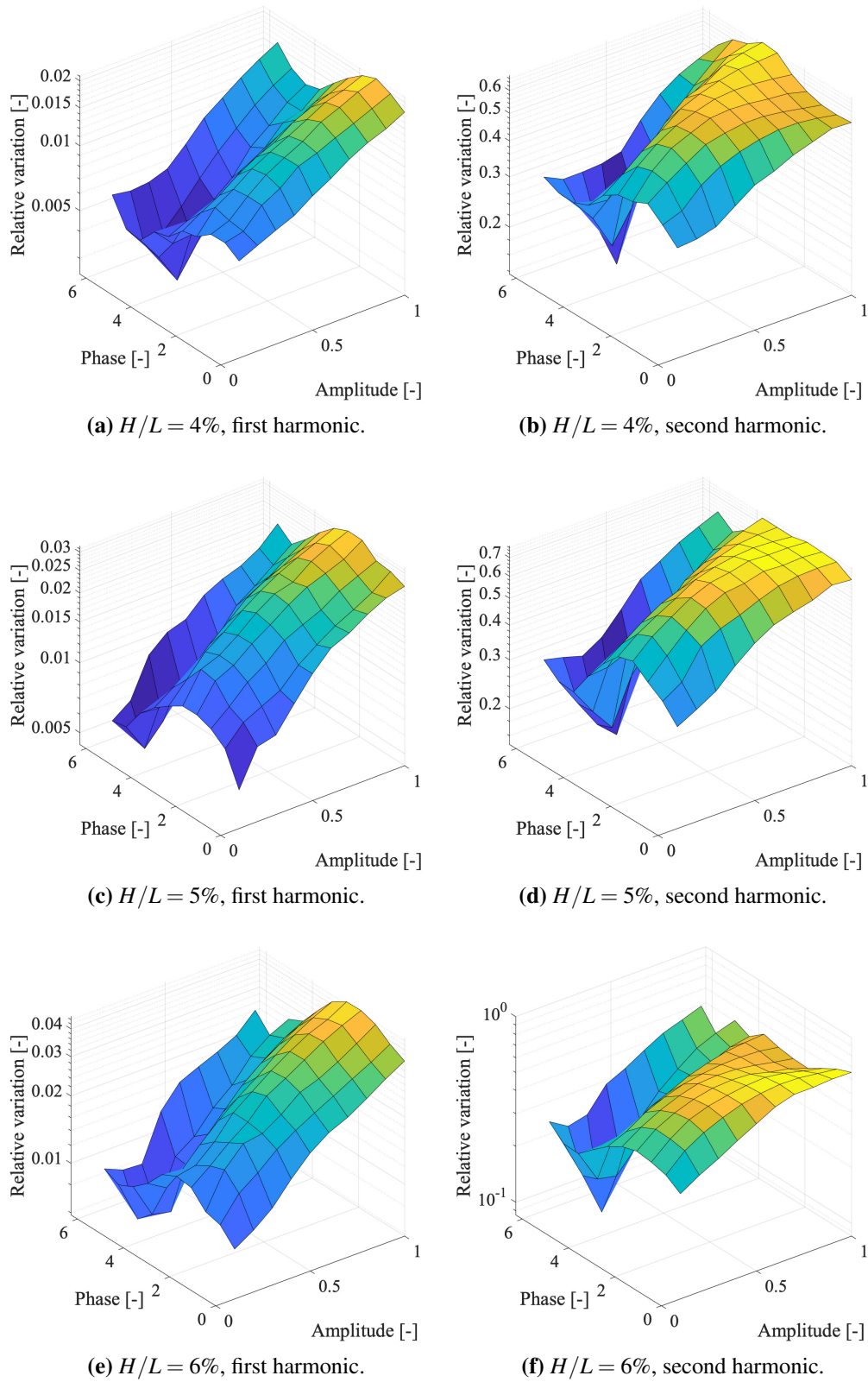


**Figure 4.9:** Maximum relative variation in first and second harmonics as function of second harmonic amplitude and phase, for waves of  $kh = 2.33$ .

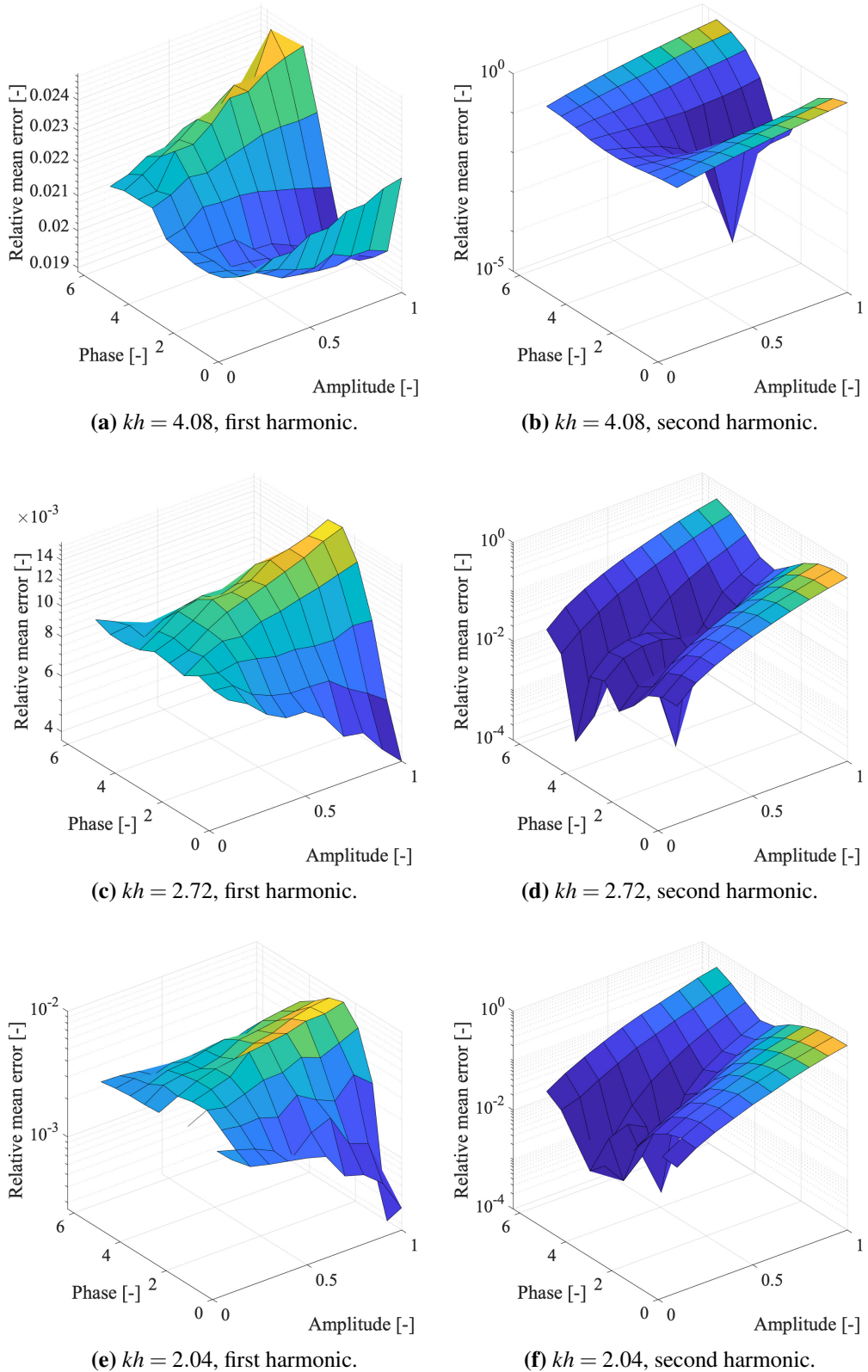


**Figure 4.10:** Relative mean error in first and second harmonics as function of second harmonic amplitude and phase, for waves of steepness  $H/L = 4\%$ .

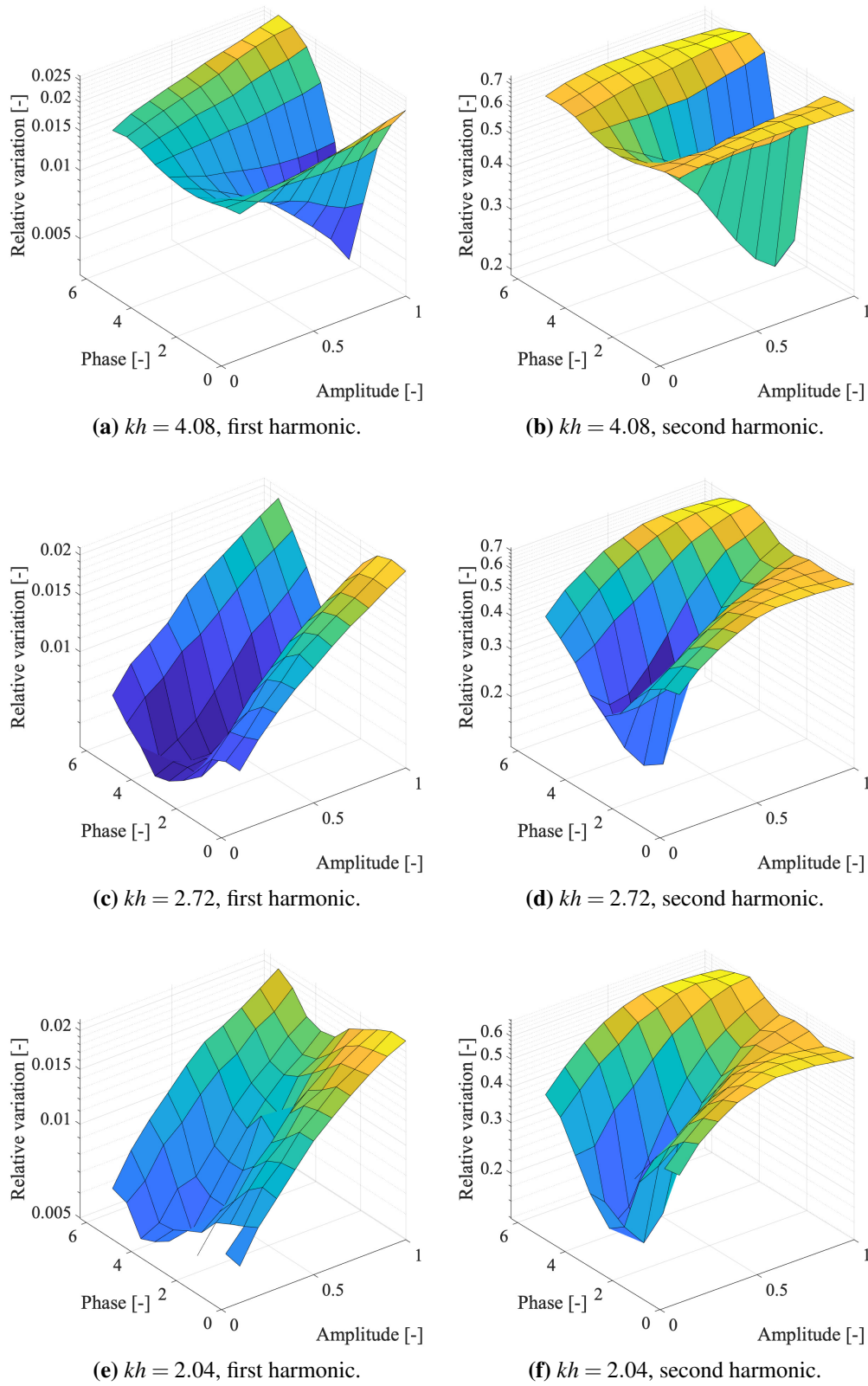


**Figure 4.11:** Maximum relative variation in first and second harmonics as function of second harmonic amplitude and phase, for waves of steepness  $H/L = 4\%$ .

minimum for the mean error in the second harmonic amplitudes (see e.g. Figure 4.8f), but rather a trough. This, combined with the apparent sensitivity of the errors to small changes in amplitude or phase, could limit the optimization process to very small steps.

# 5 | Nonlinear wave-structure interaction

This chapter presents various test cases of nonlinear wave-structure interaction, for both forced and free motion. These correspond to the explicit and implicit solution of the body boundary condition, respectively.

## 5.1 Small-amplitude motion of a heaving cylinder

The small-amplitude forced motion of a heaving circular cylinder is simulated in order to test the implementation of the integration matrices described in Section 3.6.2. Two cases are considered: shallow water and deep water. In both cases, the cylinder radius is set to  $R = 1$ . The water depth is  $h = 2R$  in the shallow water case, and  $h = 6R$  in the deep water case. Following the work presented in Read and Bingham (2012), the cylinder is moved in a Gaussian profile. This allows the force response at a large range of frequencies to be assessed simultaneously. The movement profile is determined by first specifying a minimum wavelength to be resolved, given by  $L_{min} = 2\Delta x_{max}$ , where  $\Delta x_{max}$  is the maximum grid spacing. The maximum frequency corresponding to this wavelength is found through the dispersion relation

$$\begin{aligned} f_{max} &= \frac{1}{2\pi} \sqrt{gk \tanh(kh)} \\ &= \frac{1}{2\pi} \sqrt{g \frac{2\pi}{L_{min}} \tanh\left(\frac{2\pi}{L_{min}} h\right)}. \end{aligned} \quad (5.1)$$

The amplitude of the body displacement is defined in the frequency domain as a normalized Gaussian function centered at the origin,

$$c(f) = \frac{1}{\sqrt{2\pi}s} e^{-f^2/(2s^2)}, \quad (5.2)$$

where  $s$  is the standard deviation in the frequency domain. This is defined by

$$s = \sqrt{-\frac{f_{max}^2}{2\ln(p)}}, \quad (5.3)$$

where the variable  $p$  represents the magnitude of  $c(f_{max})$  relative to  $c(0)$ . In this work, this is set to  $p = 1 \times 10^{-4}$ . The movement profile in the time domain is found by taking the inverse Fourier transform of Eq. (5.2), giving

$$\xi(t) = e^{-2\pi^2 s^2 t^2} = e^{-t^2/(2\sigma^2)}, \quad (5.4)$$

where  $\sigma$  is the standard deviation in the time domain, given by

$$\sigma = \frac{1}{2\pi s}. \quad (5.5)$$

In order to ensure that the movement profile is zero at  $t = 0$ , it may be offset by

$$\xi(t) = e^{-2\pi^2 s^2 (t-t_0)^2}, \quad (5.6)$$

where

$$t_0 = 8\sigma = \frac{4}{\pi s}. \quad (5.7)$$

The movement profile given by Eq. (5.4) was developed for linear simulations in Read and Bingham (2012), where the body remains stationary and the motion is represented by a time-varying Neumann boundary condition on the body surface. As the current work is fully-nonlinear, Eq. (5.4) is scaled by a factor  $\alpha = 0.05$ . This both ensures that the body remains partially submerged throughout the simulations, and that the simulations are quasi-linear; i.e. the results may be compared to linear analytical solutions. The final form of the movement profile in the time domain is thus

$$\xi(t) = \alpha e^{-2\pi^2 s^2 (t - \frac{4}{\pi s})^2}. \quad (5.8)$$

Simulations are carried out for a period of  $t_s = 6t_0$ , to ensure that the full force response is captured. The numerical domain length is set as  $L = 2.25v_{max}t_s + 2R$ , where  $v_{max} = \sqrt{gh}$ . With the cylinder positioned at  $x_0 = L/2$ , this ensures that sampling is completed before the fastest wave component returns to the body. The time step is defined by

$$\Delta t = C \frac{\Delta x}{v_{max}}, \quad (5.9)$$

where the Courant number is set to  $C = 0.5$ . Figure 5.1 shows the normalized movement and force response in both shallow and deep water.

The frequency-dependent added mass and damping are evaluated as the ratio of the Fourier-transformed force and movement signals, as

$$a_{ij}(\omega) = \Re \left[ \frac{f\{F_j(t)\}}{f\{\xi_j(t)\}} \right] / \omega^2 \quad (5.10)$$

$$b_{ij}(\omega) = -\Im \left[ \frac{f\{F_j(t)\}}{f\{\xi_j(t)\}} \right] / \omega, \quad (5.11)$$

where  $f\{\cdot\}$  represents the Fourier transform. These values are subsequently made non-dimensional by

$$\mu_{ij} = \frac{a_{ij}}{\frac{1}{2}\pi\rho R^2}, \quad i, j = 1, 3, 5, \quad (5.12)$$

$$v_{ij} = \frac{b_{ij}}{\frac{1}{2}\pi\rho\omega R^2}, \quad i, j = 1, 3, 5 \quad (5.13)$$

Figure 5.2 shows a comparison of the numerical and analytical solutions for both shallow and deep water. In this figure, the shallow water results are compared to the analytical solution of Bai (1977), and the deep water results are compared to the analytical solution of Porter (2008). The numerical solution shows good agreement with the analytical solutions within their respective areas of validity.

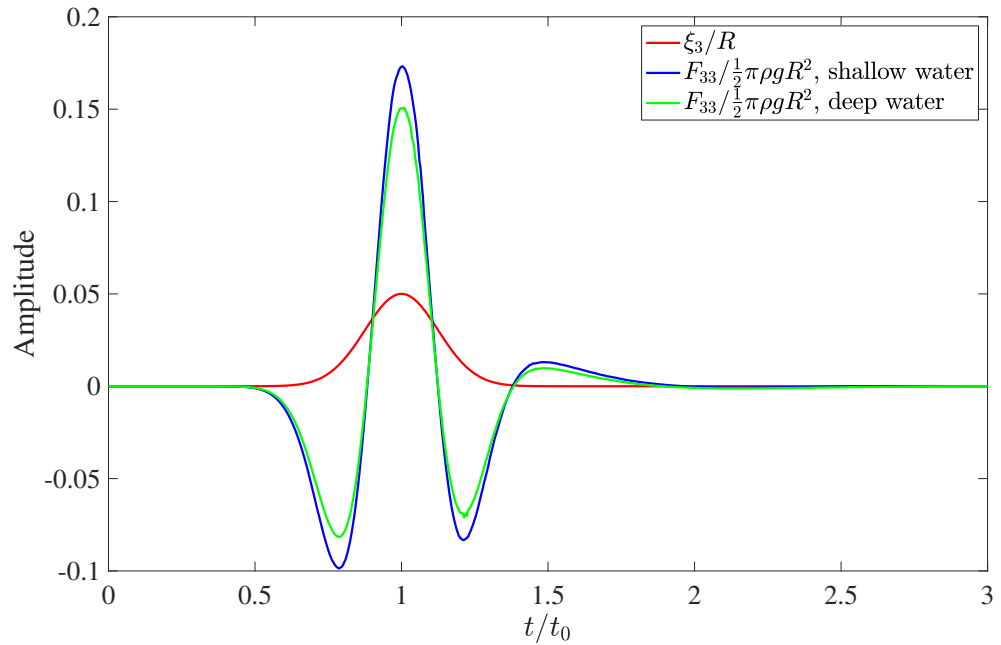


**Figure 5.1:** Gaussian movement profile and force response in shallow ( $h = 2R$ ) and deep ( $h = 6R$ ) water.

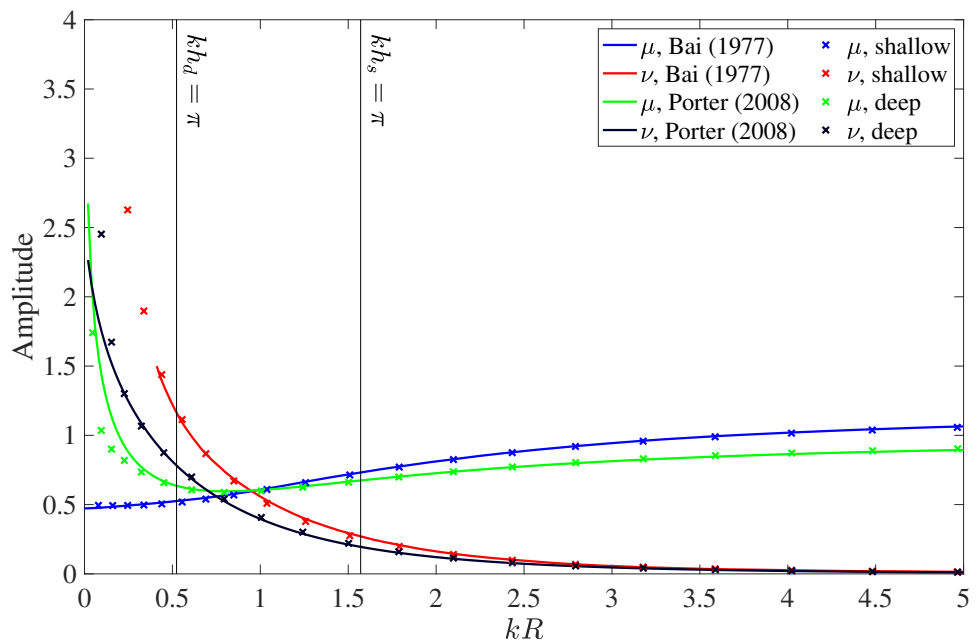


**Figure 5.2:** Comparison of numerical and analytical solutions for small-amplitude motion of a heaving cylinder. Vertical lines indicate limits of validity for shallow- and deep-water analytical solutions.

### 5.1.1 Comparison of force signals

Previous work with the OW3D solver by Kontos (2016) evaluated wave loads in forced-motion cases by splitting the dynamic pressure into two terms - one containing the time derivative of the velocity potential, and the other containing its gradient. The latter term was evaluated at each time step during the simulations, based on the current solution. The former was evaluated at the end of the simulations, using finite-difference stencils of the same order as those used for spatial derivatives. As the position of the body points change throughout the simulations, while the body moves through the domain, the time derivative of the velocity potential becomes

$$\frac{\partial \phi}{\partial t} = \frac{d\phi}{dt} - \frac{dx}{dt} \frac{\partial \phi}{\partial x} - \frac{dy}{dt} \frac{\partial \phi}{\partial y} - \frac{dz}{dt} \frac{\partial \phi}{\partial z}. \quad (5.14)$$

As described in Kontos (2016), this procedure ultimately led to spurious oscillations in the force signal, thought to be due to changing truncation errors between time steps. This section presents a comparison of the previous and current methods for evaluating the force on a heaving circular cylinder, for various quasi-linear and nonlinear cases. Figure 5.3 shows simulations of increasing nonlinearity, where the motion amplitude increases from  $A = 0.001R$  to  $A = 0.1R$ . The effect of the numerical oscillations in the previous method become more significant as the nonlinearity increases. Figure 5.4 shows a similar comparison, where this time the motion amplitude is kept fixed at  $A = 0.001R$  (i.e. a quasi-linear case), but different nondimensional wave numbers are compared. Again, numerical oscillations in the previous method become more significant as shorter waves are simulated.

## 5.2 Submerged surging dipole

The full implicit implementation is tested on a surging dipole in an infinite fluid. The velocity potential is given by

$$\phi(x, z) = \frac{\mu}{2\pi} \frac{x - x_0}{(x - x_0)^2 + (z - z_0)^2}, \quad (5.15)$$

where  $(x_0, y_0)$  are the coordinates of the centre of the dipole. The dipole moment  $\mu$  is defined by

$$\mu = -2R^2\pi u, \quad (5.16)$$

where  $R$  is the radius, and the horizontal dipole velocity is

$$u = -A\omega \sin(\omega t). \quad (5.17)$$

The analytic solution of  $\phi_t$  is thus

$$\phi_t(x, z) = R^2 A \omega^2 \cos(\omega t) \frac{x - x_0}{(x - x_0)^2 + (z - z_0)^2}. \quad (5.18)$$

To test the operators developed in Section 3.6.2, each term in Eq. (3.36) is evaluated explicitly before solving the problem implicitly using the method outlined above. The convergence of the explicit evaluation of each term, and of the implicit solution, is shown in Figure 5.5.

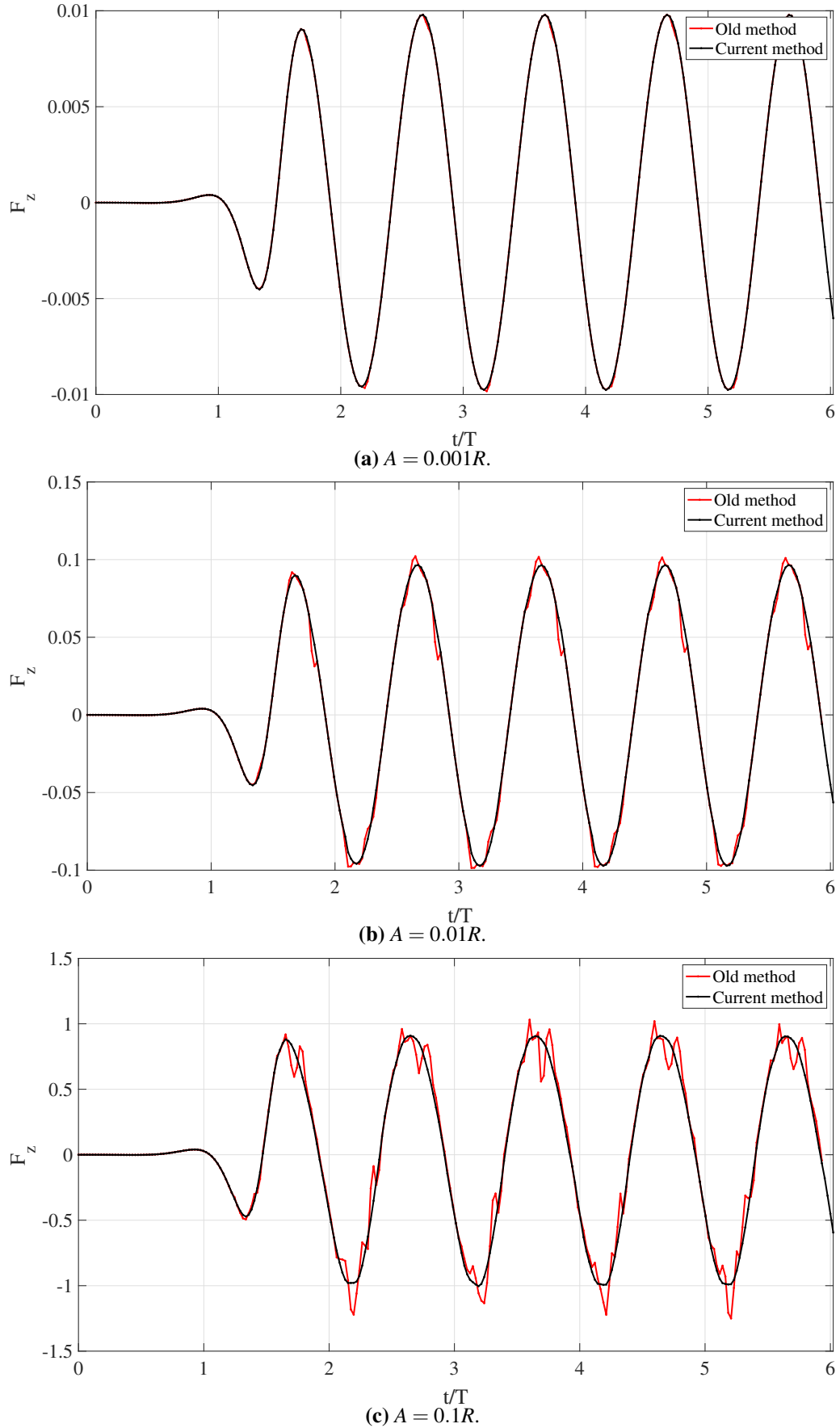


**Figure 5.3:** Comparison of calculated wave force on heaving circular cylinder, for water depth  $h = 2R$  and nondimensional wave number  $kR = 0.60$ .

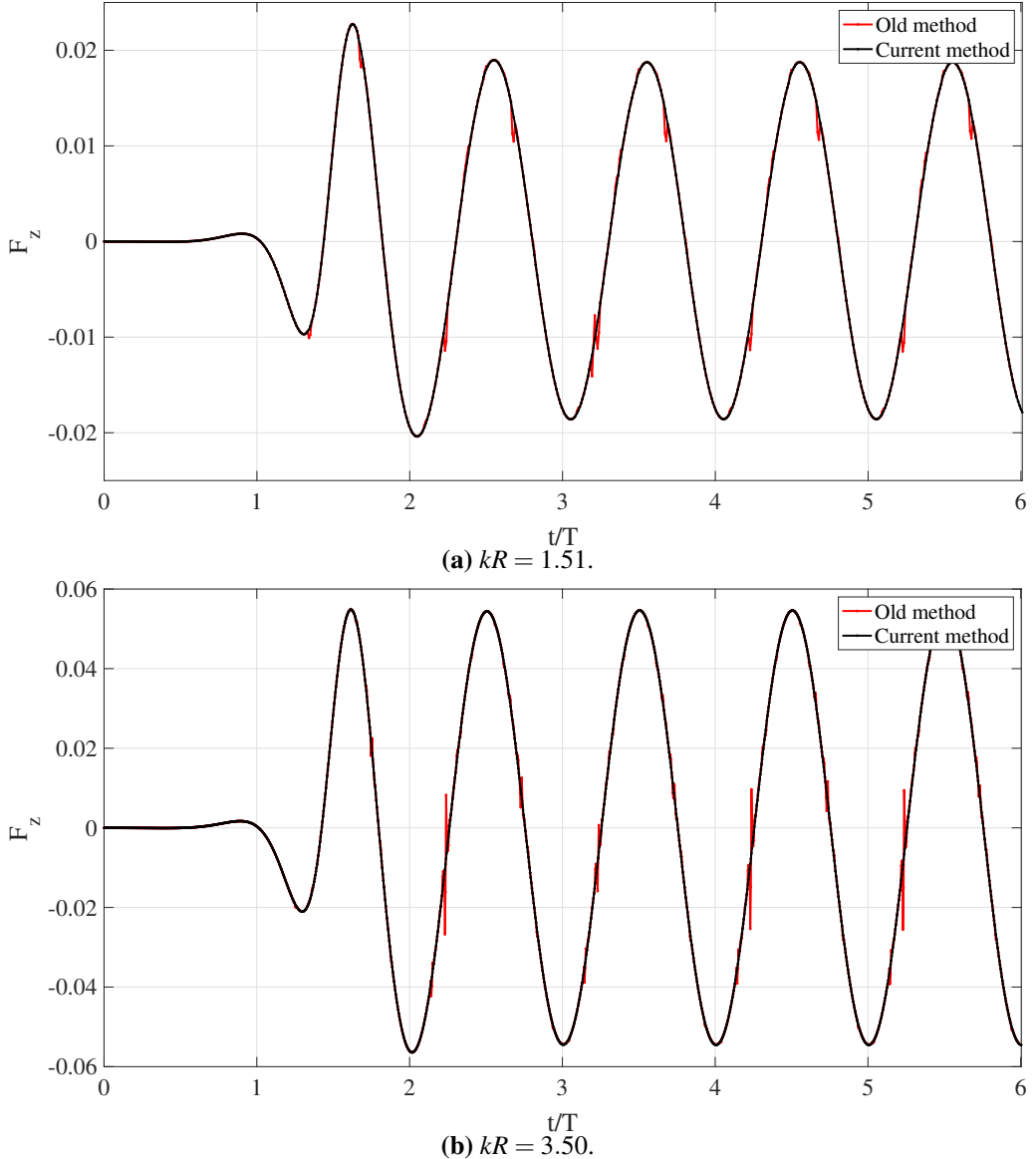


**Figure 5.4:** Comparison of calculated wave force on heaving circular cylinder, for water depth  $h = 2R$  and amplitude  $A = 0.001R$ .

### 5.3 Cylinder at rest on the free surface

Having established that the implicit solver is working correctly, the next step is to verify that a freely-floating body initially at rest on a quiescent free surface will remain stationary. The initial conditions for such a test are simply that the free surface and velocity potential are zero throughout the domain. The body is a 2D cylinder of radius  $R = 1$  and mass  $m = \pi/2$ , with the cylinder center set at  $(x_0, z_0) = (0, 0)$ . The water density and gravitational acceleration are set to  $\rho = g = 1$ . Two conditions are tested: the convergence of the horizontal and vertical velocities after one time step; and the time evolution of the cylinder's position. For the former, the time step must be held constant across discretizations, and is chosen based on the finest discretization. Figure 5.6 shows the convergence of the horizontal and vertical velocities, both of which should converge towards zero. Figure 5.7 shows the time evolution of the cylinder position, for three different stencil sizes.

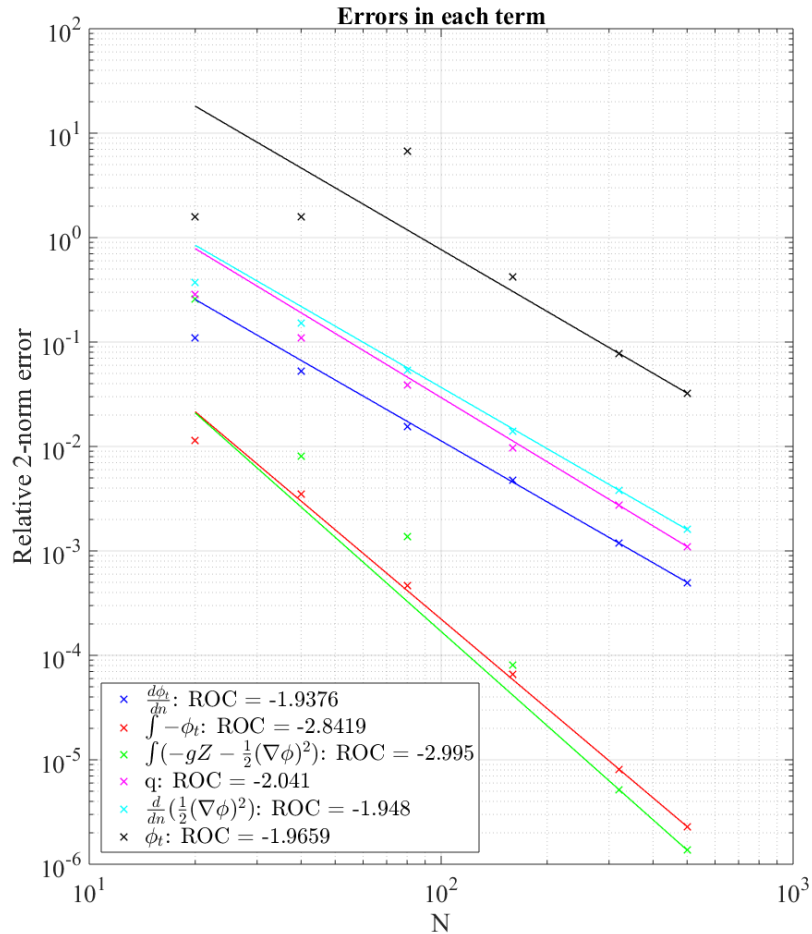


**Figure 5.5:** Convergence of explicit operators.

While a small degree of initial oscillation in the cylinder vertical position may be expected due to differences between the analytical and numerical mass, the growing oscillations in the time series indicate a weak numerical instability. Although the high-order ( $r = 7$ ) results appear to be stable, running this simulation for a period of 100 seconds shows that the numerical instability is still present. This is shown in Figure 5.8. However, applying an 11-point, 9th-order Savitzky-Golay filter (Savitzky and Golay (1964)) to the free-surface variables at each time step appears to mitigate the instability by removing a small amount of energy from the fluid. This is shown in Figure 5.9.

## 5.4 Free-surface decay test

The final case is a decay test, where the 2D cylinder from the previous example is now raised some distance above the quiescent free surface and released. Here the time evolution of the cylinder vertical position is compared with the experimental data of Ito (1977). The domain length is set such that the longest waves will not return to the cylinder before the end of the simulation. Given a maximum wave speed of  $v_{max} = \sqrt{gh}$ , and a simulation time of  $t_s$ , the domain length is set as  $L = 2R + 2v_{max}t_s$ , with  $R$  the cylinder radius. The cylinder is thus placed at the domain midpoint,

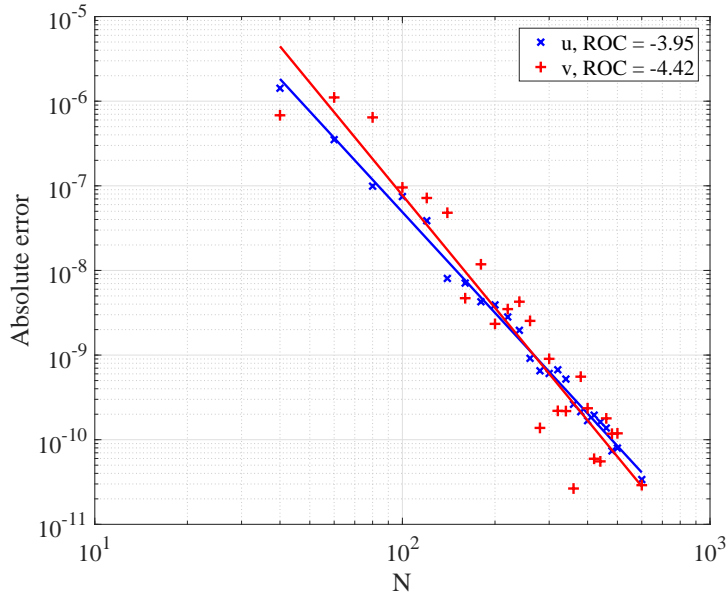


**Figure 5.6:** Convergence of horizontal and vertical velocities for a cylinder at rest on a quiescent free surface.

$x_0 = L/2$ . The initial displacement of the cylinder is set to  $z_0 = 0.1R$ , with a water depth of  $h = 10R$ . This is somewhat smaller than the displacements used by Ito (1977) (who uses  $z_0 = 0.33R$ ,  $0.5R$ , and  $0.66R$ ) but, as the experimental data is normalized by the initial displacement, the general characteristics of the motion may still be compared. This comparison is shown in Figure 5.10. Following the results of Section 5.3, an 11-point, 9th-order Savitzky-Golay filter has been applied to the free-surface variables at every time step. As shown in Figure 5.10, the numerical simulation shows good agreement with the experimental data over the initial oscillation. This indicates that the application of a smoothing filter to the free-surface variables can reduce the effect of the weak numerical instability, and allow for simulation of free-body problems at flexible order.

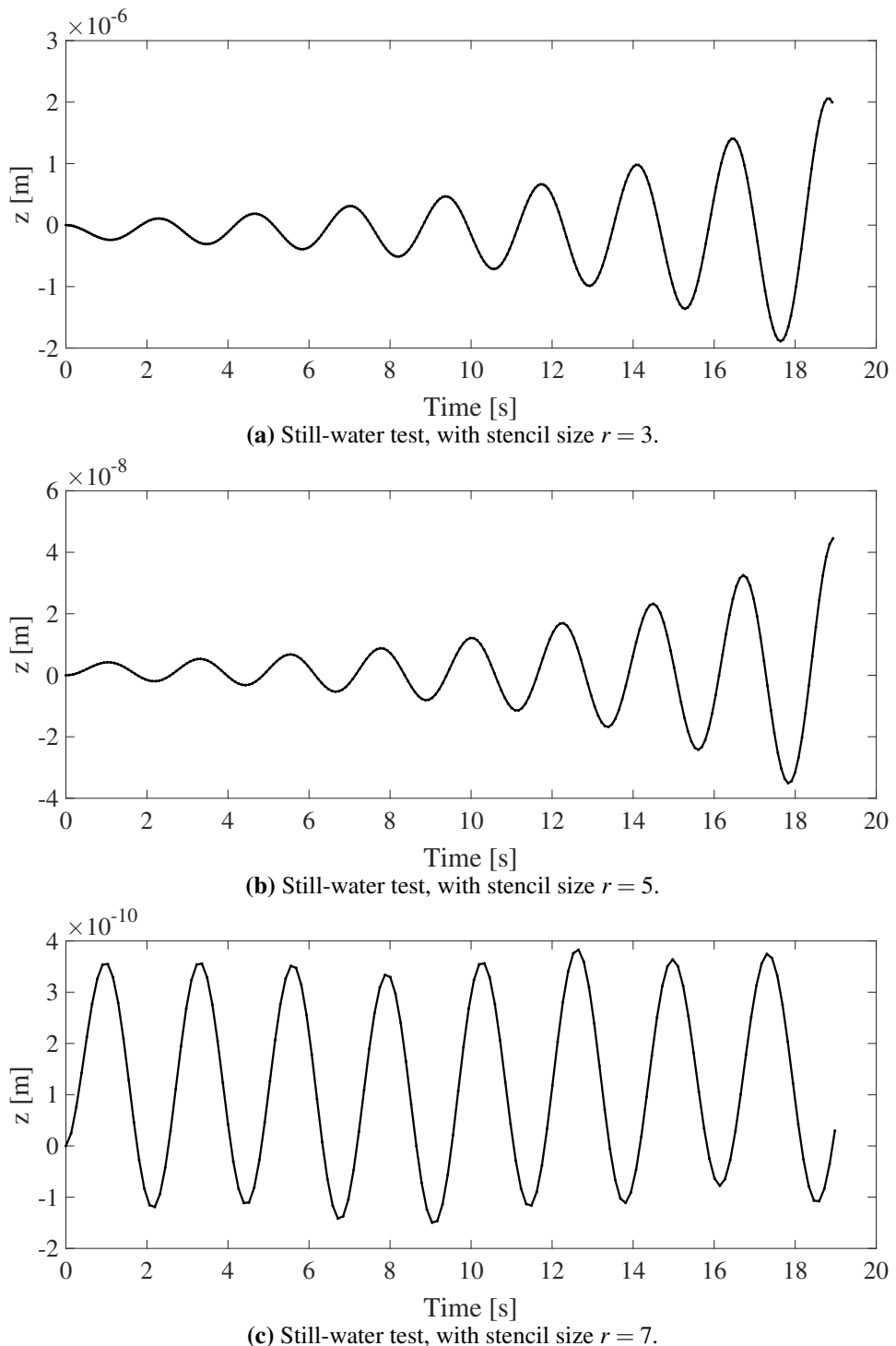


**Figure 5.7:** Time evolution of cylinder position, for a cylinder initially at rest on a quiescent free surface.

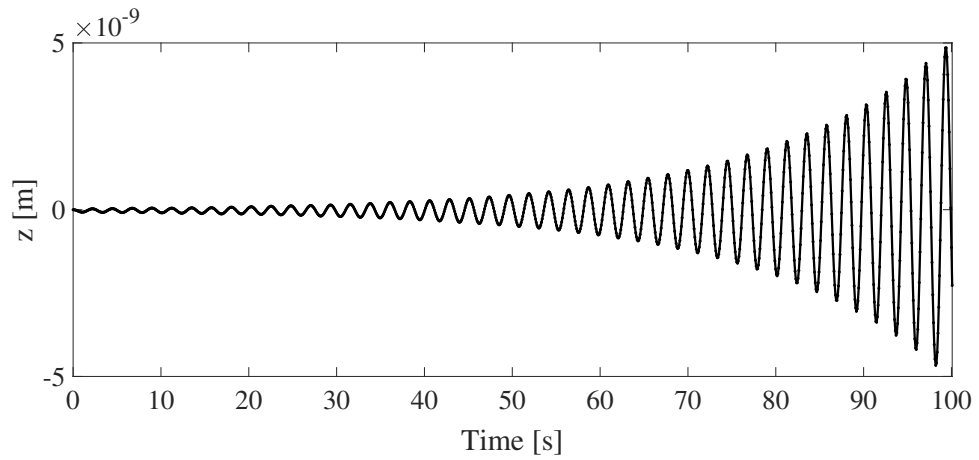


**Figure 5.8:** Time evolution of cylinder position over many periods, for a cylinder initially at rest on a quiescent free surface. Stencil size is  $r = 7$ .

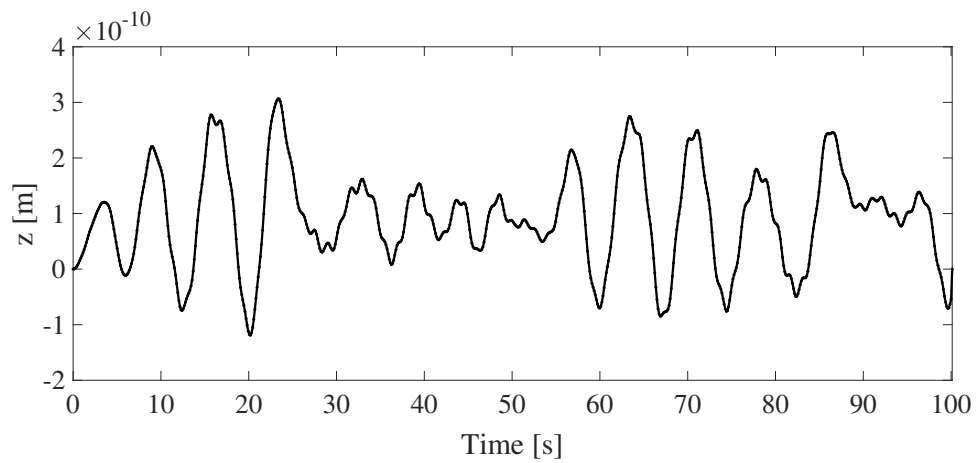


**Figure 5.9:** Time evolution of cylinder position over many periods, with a high-order Savitzky-Golay filter applied every time step. Stencil size is  $r = 7$ .

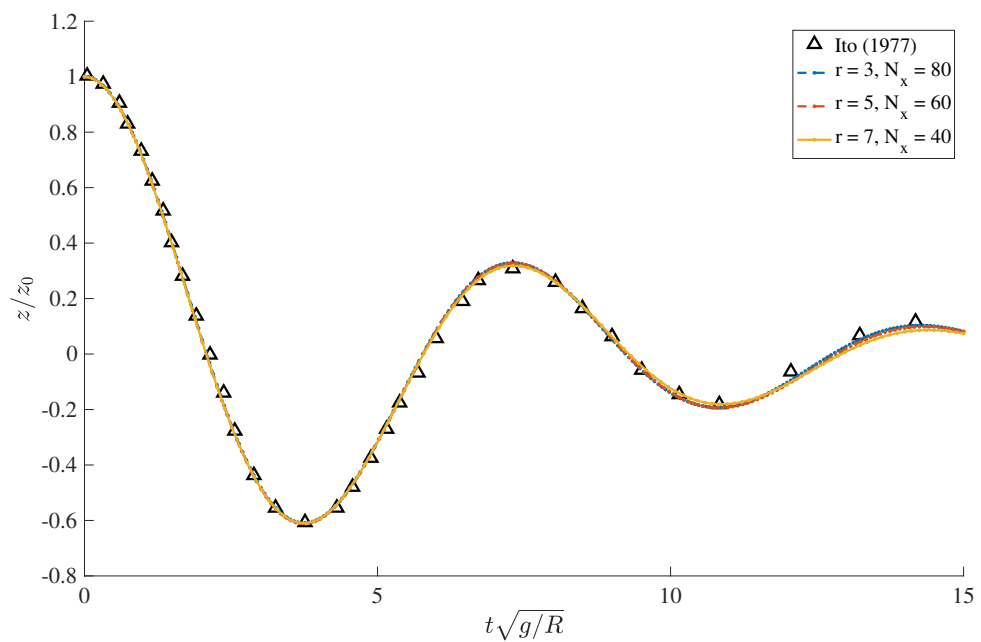


**Figure 5.10:** Free decay of a circular cylinder for various stencil sizes.

## 6 | Summary and perspectives

In this research, the fully nonlinear, finite-difference based potential flow solver OW3D has been extended in two areas and subsequently applied to wave generation and wave-structure interaction problems.

First, body-free-surface intersection point tracking has been introduced to deal with challenges arising from using an IBM in conjunction with a  $\sigma$ -transformation of the vertical coordinate, and a multi-stage time-stepping method. Tracking the body-free-surface intersection point improves the generation of the artificial interior free surface by providing a better estimation of the intersection point location and derivatives, which are used as boundary conditions when generating the artificial interior free surface. Furthermore, this improves the interpolation of values to new free-surface points that emerge from the body between Runge-Kutta stages. Finally, the calculation of the force on the body is also improved, by maintaining consistent limits for the integration over the wetted surface. Simulations using the intersection point have been carried out for a surging piston wavemaker and a heaving cylinder. The former compared favourably with both first- and second-order theoretical solutions, as well as with experimental data. Simulations with a heaving cylinder showed that the point gradually detaches from the body surface. This is thought to be due to a limitation in the implementation, which updates the intersection point position based on the local body tangent. While this is sufficient for small body motions and/or local curvatures, in the general case it is an insufficient condition to ensure that the intersection point remains on the body surface. Initial tests with filtering and artificial re-attachment indicate that this may alleviate the problem, but a more general solution could be to recast the intersection point updating equation from a Cartesian to a curvilinear coordinate system. Ultimately, problems relating to the artificial interior free surface continue to be a weakness of the solver in general. Implementation of a wave-breaking model would be beneficial, but may not be enough to overcome the challenges in maintaining  $C^2$ -continuity while simulating large body motions and/or complex geometries.

Second, a method for evaluating nonlinear wave loads has been developed for use with the IBM, based on solving a boundary value problem for the time derivative of the velocity potential at each time step. This provides a coupling between the body and fluid motions at each time step. This has eliminated spurious oscillations in the calculated force, which have been reported in previous work and were thought to stem from the IBM. Comparison with previous implementations at various wave numbers and motion amplitudes shows significant improvement, especially as non-linearity increases. Quasi-linear numerical simulations show favourable agreement with analytical solutions for deep- and shallow-water cases. The implementation also allows for free-body motions to be simulated by direct solution of the implicit body boundary condition. However, initial testing of a cylinder at rest on a quiescent free surface indicates that there is a weak instability

related to solving the implicit body boundary condition. A linear stability analysis of the temporal problem would be a first step in solving this. Applying a high-order Savitzky-Golay filter to the free surface variables at every time step appears to mitigate the instability when using high-order stencils. This allows for favourable comparison against experimental measurements for the free decay of a circular cylinder.

Finally, the OW3D solver has been applied to the problem of wave generation by a moving boundary, and an optimization procedure has been developed that can produce stable wave fields accurate up to second-order. Numerical simulations of a heaving wedge wavemaker compared favourably with experiments carried out at DTU, for waves in intermediate- and deep-water regimes. The optimization procedure was applied to a heaving wedge wavemaker, for waves in intermediate and deep water and steepness up to 50% of the theoretical maximum. Initially, only optimization of harmonic stroke amplitudes was considered. In all cases the relative mean errors in the first harmonic amplitude were reduced to below 2%, and to below 10% in the second harmonic amplitude. Measuring the free-surface elevation at various points in the numerical wave tank showed a significant reduction in variation following the optimization procedure, indicating a stable wave field. Investigation of phase optimization suggests that the optimal combination of amplitude and phase may change with wave steepness - a factor that is not included in current second-order wavemaker theory. The apparent sensitivity of the error, and possible lack of a global minimum, make combined amplitude and phase optimization a challenging task.

# References

- A. M. Abdelrazek and I. Kimura. Comparison between SPH and MPS methods for numerical simulations of free surface flow problems. *Journal of Japan Society of Civil Engineers*, 70: 67–72, 2014.
- M. Amini Afshar. *Predicting the added resistance of slow ships in waves*. PhD thesis, Technical University of Denmark, 2014.
- C. Ai and S. Jin. Non-hydrostatic finite volume model for non-linear waves interacting with structures. *Computers & Fluids*, 39:2090–2100, 2010.
- M. Amini-Ashfar, H. B. Bingham, W. D. Henshaw, , and R. W. Read. A nonlinear potential-flow model for wave-structure interaction using high-order finite differences on overlapping grids. In *34th International Workshop on Water Waves and Floating Bodies*, 2019.
- S. N. Atluri and T. Zhu. A new meshless local Petrov-Galerkin (MLPG) approach in computational mechanics. *Computational Mechanics*, 22:117–127, 1998.
- K. J. Bai. The added mass of two-dimensional cylinders heaving in water of finite depth. *Journal of Fluid Mechanics*, 81:85–105, 1977.
- J. T. Batina. Unsteady Euler airfoil solutions using unstructured dynamic meshes. *AIAA*, 28: 1381–1388, 1989.
- T. B. Benjamin and J. E. Feir. The disintegration of wave trains on deep water. Part 1. Theory. *Journal of Fluid Mechanics*, 27:417–430, 1967.
- T. B. Benjamin and K. Hasselmann. Instability of Periodic wavetrains in Nonlinear Dispersive Systems [and Discussion]. In *Proceedings of the Royal Society of London. Series A, Mathematical and Physical Sciences*, 1967.
- P. J. F. Berkvens. *Floating Bodies Interacting with water waves*. PhD thesis, University of Twente, The Netherlands, 1998.
- P. A. Berthelsen and O. M. Faltinsen. A local directional ghost cell approach for incompressible viscous flow problems with irregular boundaries. *Journal of Computational Physics*, 227:4354–4397, 2008.
- F. Biésel and F. Suquet. Les appareils génératrices de hole en laboratoire. *La Houille Blanche*, 2: 147–165, 1951a.

- F. Bi  sel and F. Suquet. Les appariels g  n  rateurs de hole en laboratoire. *La Houille Blanche*, 4: 475–496, 1951b.
- H. Bihs, A. Kamath, M. A. Chella, and   . Arntsen. Wave-structure interaction of focussed waves in REEF3D. In *35th International Conference on Ocean, Offshore and Arctic Engineering*, 2016.
- H. B. Bingham and H. Zhang. On the accuracy of finite-difference solutions for nonlinear water waves. *Journal of Engineering Mathematics*, 58:211–228, 2007.
- H. B. Bingham, A. P. Engsig-Karup, and O. Lindberg. A high-order finite difference method for nonlinear wave-structure interaction. In *22nd International Workshop for Water Waves and Floating Bodies*, 2007.
- U. Bosi, A. P. Engsig-Karup, C. Eskilsson, and M. Ricchiuto. A spectral/hp element depth-integrated model for nonlinear wave-body interaction. *Computer Methods in Applied Mechanics and Engineering*, 348:222–249, 2019.
- H. Braess and P. Wriggers. Arbitrary Lagrangian Eulerian finite element analysis of free surface flow. *Computer Methods in Applied Mechanics and Engineering*, 190:95–109, 2000.
- L. L. Broderick and J. W. Leonard. Nonlinear water-wave structure interaction. *Computers and Structures*, 44:837–842, 1992.
- Y. Cao, R. F. Beck, and W. W. Schultz. Nonlinear computation of wave loads and motions of floating bodies in incident waves. In *9th International Workshop on Water Waves and Floating Bodies*, 1994.
- F. Casadei and J. P. Halleux. An algorithm for permanent fluid-structure interaction in explicit transient dynamics. *Computers Methods in Applied Mechanics and Engineering*, 128:231–289, 1995.
- F. Casadei, J. P. Halleux, A. Sala, and F. Chille. Transient fluid-structure interaction algorithms for large industrial applications. *Computers Methods in Applied Mechanics and Engineering*, 190:3081–3110, 2001.
- R. K. C. Chan and R. L. Street. A computer study of finite-amplitude water waves. *Journal of Computational Physics*, 6:68–94, 1970.
- M. Christou. *Fully nonlinear computations of waves and wave-structure interaction*. PhD thesis, Department of Civil and Environmental Engineering, Imperial College London, 2009.
- M. H. Chung. Cartesian cut cell approach for simulating incompressible flows with rigid bodies of arbitrary shape. *Computers & Fluids*, 35:607–623, 2006.
- M. H. Chung. An adaptive cartesian cut-cell/level-set method to simulate incompressible two-phase flows with embedded moving solid boundaries. *Computers & Fluids*, 71:469–486, 2013.

- R. Cointe. *Quelques aspects de la simulation numérique d'un canal à houle*. PhD thesis, École Nationale des Ponts et Chaussées, 1989.
- R. Cointe, P. Geyer, B. King, B. Molin, and M. Tanoni. Nonlinear and linear motions of a rectangle barge in a perfect fluid. In *18th Symposium on Naval Hydrodynamics*, 1991.
- M. Costabel. Principles of boundary element methods, 1986.
- R. A. Dalrymple and B. D. Rogers. Numerical modeling of water waves with the SPH method. *Coastal Engineering*, 53:141–147, 2006.
- A. Decoene and J. F. Gerbeau. Sigma transformation and ALE formulation for three-dimensional free surface flows. *International Journal for Numerical Methods in Fluids*, 59:357–386, 2008.
- E. Dombre, J. C. Harris, M. Benoit, D. Violeau, and C. Peyrard. A 3D parallel boundary element method on unstructured triangular grids for fully nonlinear wave-body interactions. *Ocean Engineering*, 171:505–518, 2019.
- D. G. Dommermuth and D. K. P. Yue. A high-order spectral method for the study of nonlinear gravity waves. *Journal of Fluid Mechanics*, 184:267–288, 1987.
- J. Donea, A. Huerta, J. Ph. Ponthot, and A. Rodriguez-Ferran. *Arbitrary Lagrangian-Eulerian Methods*. John Wiley & Sons, 2004.
- F. Duarte, R. Gormaz, and S. Natesan. Arbitrary Lagrangian-Eulerian method for Navier-Stokes equations with moving boundaries. *Computer Methods in Applied Mechanics and Engineering*, 193:4819–4836, 2004.
- G. Ducrozet, H. B. Bingham, A. P. Engsig-Karup, and P. Ferrant. High-order finite difference solutions for 3D nonlinear wave-structure interaction. In *9th International Conference on Hydrodynamics*, 2010.
- G. Ducrozet, A. P. Engsig-Karup, H. B. Bingham, and P. Ferrant. A non-linear wave decomposition model for efficient wave-structure interaction. Part A: Formulation, validations and analysis. *Journal of Computational Physics*, 257:863–883, 2014.
- B. Duz, T. Bunnik, G. Kapsenberg, and G. Vaz. Numerical simulation of nonlinear free surface water waves - coupling of a potential flow solver to a URANS/VOF code. In *35th International Conference of Ocean, Offshore and Arctic Engineering*, 2016.
- D. Ellix and K. Arumugam. An Experimental Study of Waves Generated by an Oscillating Wedge. *Journal of Hydraulic Research*, 22:5:299–313, 1984.
- A. P. Engsig-Karup and W. Laskowski. Efficient p-multigrid spectral element model for water waves and marine offshore structures. *arXiv e-prints*, art. arXiv:2009.00705, August 2020.
- A. P. Engsig-Karup, H. B. Bingham, and O. Lindberg. An efficient flexible-order model for 2D nonlinear water waves. *Journal of Computational Physics*, 228:2100–2118, 2009.

- A. P. Engsig-Karup, M. G. Madsen, and S. L. Glimberg. A massively parallel GPU-accelerated model for analysis of fully nonlinear free surface waves. *International Journal for Numerical Methods in Fluids*, 70:20–36, 2012.
- A. P. Engsig-Karup, C. Eskilsson, and D. Bigoni. A stabilised nodal spectral element method for fully nonlinear water waves. *Journal of Computational Physics*, 318:1–21, 2016.
- A. P. Engsig-Karup, C. Monteserin, and C. Eskilsson. A stabilised nodal spectral element method for fully nonlinear water waves Part 2: wave-body interaction. *Journal of Computational Physics*, 2017.
- A. P. Engsig-Karup, C. Monteserin, and C. Eskilsson. A Mixed Eulerian-Lagrangian Spectral Element Method for Nonlinear Wave Interaction with Fixed Structures. *Water Waves*, 1:315–342, 2019.
- J. D. Fenton. The numerical solution of steady water wave problems. *Computers and Geosciences*, 14:357–368, 1988.
- P. Ferrant, D. L. Touze, and K. Pelletier. Non-linear time-domain models for irregular wave diffraction about offshore structures. *International Journal for Numerical Methods in Fluids*, 43:1257–1277, 2003.
- R. E. Flick and R. T. Guza. Paddle Generated Waves in Laboratory Channels. *Journal of the Waterway, Port, Coastal, and Ocean Division*, 106(WW1):79–97, 1980.
- P. Fontanet. Théorie de la génération de la houle cylindrique par un batteur plan. *La Houille Blanche*, 1:3–31, 1961a.
- P. Fontanet. Les appariels génératrices de houle en laboratoire. *La Houille Blanche*, 2:174–197, 1961b.
- B. Fornberg. Calculation of weights in finite-difference formulas. *SIAM Review*, 40:685–691, 1998.
- W. Froude. The rolling of ships. *Transactions of the Institution of Naval Architects*, 2:180–229, 1861.
- D. R. Fuhrman and H. B. Bingham. Numerical solutions of fully non-linear and highly dispersive Boussinesq equations in two horizontal dimensions. *International Journal for Numerical Methods in Fluids*, 44:231–255, 2004.
- S. Glimberg, A. P. Engsig-Karup, and L. Olson. A massively scaleable distributed multigrid framework for nonlinear marine hydrodynamics. *International Journal of High Performance Computing Applications*, 2018.
- S. L. Glimberg. *Designing scientific software for heterogeneous computing with application to large-scale water waves simulations*. PhD thesis, Technical University of Denmark, 2013.

- M. Greenhow and W. M. Lin. Nonlinear Free Surface Effects: Experiments and Theory. Technical Report 83–19, MIT, Dept. of Ocean Engineering, 1983.
- E. Guerber, M. Benoit, S. T. Grilli, and C. Buvat. A fully nonlinear implicit model for wave interactions with submerged structures in forced or free motion. *Engineering Analysis with Boundary Elements*, 36:1151–1163, 2012.
- J. Buhr Hansen and Ib. A. Svendsen. Laboratory Generation of Waves of Constant Form. In *14th Conference on Coastal Engineering*, pages 321–339, 1975.
- F. C. W. Hanssen. *Non-Linear Wave-Body Interaction in Severe Waves*. PhD thesis, Norwegian University of Science and Technology, 2019.
- F. C. W. Hanssen, M. Greco, and Y. Shao. The Harmonic Polynomial Cell Method for Moving Bodies Immersed in a Cartesian Background Grid. In *34th International Conference on Ocean, Offshore and Arctic Engineering*, 2015.
- F. H. Harlow and J. E. Welch. Numerical calculation of time-dependent viscous incompressible flow of fluid with free surface. *The Physics of Fluids*, 8:2182–2189, 1965.
- J. C. Harris, E. Dombre, M. Benoit, and S. T. Grilli. A comparison of methods in fully nonlinear boundary element numerical wave tank development. In *DGA Techniques Hydrodynamiques*, 2014.
- J. C. Harris, C. M. O'Reilly, A. Mivehchi, K. Kuznetsov, C. F. Janssen, S. T. Grilli, and J. M. Dahl. Hybrid modeling of wave structure interaction with overlapping viscous-inviscid domains. In *33rd International Workshop on Water Waves and Floating Bodies*, 2018.
- H. Hashimoto, K. Kawamura, and M. Sueyoshi. A numerical simulation method for transient behavior of damaged ships associated with flooding. *Ocean Engineering*, 143:282–294, 2017.
- T. H. Havelock. Forced surface-waves on water. *The London, Edinburgh, and Dublin Philosophical Magazine and Journal of Science*, 8:51:569–576, 1929.
- G. He and M. Kashiwagi. Higher-order BEM for radiation forces of a modified Wigley hull with forward speed. In *23rd International Offshore and Polar Engineering Conference*, 2013.
- G. He and M. Kashiwagi. Radiation-problem solutions using a time-domain iterative HOBEM. *International Journal of Offshore and Polar Engineering*, 24:81–89, 2014a.
- G. He and M. Kashiwagi. Time-domain analysis of steady ship-wave problem using higher-order BEM. *International Journal of Offshore and Polar Engineering*, 24:1–10, 2014b.
- G. He, T. Isshiki, and M. Kashiwagi. Prediction of radiation forces by means of a CIP-based cartesian grid method. In *21st International Offshore and Polar Engineering Conference*, 2011.
- P. D. Hieu and K. Tanimoto. Verification of a VOF-based two-phase flow model for wave breaking and wave-structure interactions. *Ocean Engineering*, 33:1565–1588, 2006.

- C. W. Hirt and B. D. Nichols. Volume of Fluid (VOF) method for the dynamics of free boundaries. *Journal of Computational Physics*, 39:201–225, 1981.
- C. W. Hirt, A. A. Amsden, and J. L. Cook. An arbitrary Lagrangian-Eulerian computing method for all flow speeds. *Journal of Computational Physics*, 135:203–216, 1997.
- C. Hu, M. Kashiwagi, and T. Momoki. Numerical simulation of non-linear free surface wave generation by CIP method and its applications. In *13th International Offshore and Polar Engineering Conference*, 2003.
- C. Hu, O. Faltinsen, and M. Kashiwagi. 3-D numerical simulation of freely moving floating body by CIP method. In *15th International Offshore and Polar Engineering Conference*, 2005.
- C. Hu, M. Kashiwagi, and A. Kitadai. Numerical simulation of strongly nonlinear wave-body interactions with experimental validation. In *16th International Offshore and Polar Engineering Conference*, 2006.
- C. Hu, M. Kashiwagi, M. Sueyoshi, and I. Nakagiri. Numerical simulation of strongly nonlinear wave-ship interaction by CIP/cartesian grid method. In *18th International Offshore and Polar Engineering Conference*, 2008.
- C. Hu, M. Sueyoshi, and M. Kashiwagi. Numerical simulation of strongly nonlinear wave-ship interaction by CIP-based cartesian grid method. *International Journal of Offshore and Polar Engineering*, 20:81–87, 2010.
- R. T. Hudspeth and W. Sulisz. Stokes Drift in Two-Dimensional Wave Flumes. *Journal of Fluid Mechanics*, 230:209–229, 1991.
- T. J. R. Hughes, W. K. Liu, and T. K. Zimmermann. Lagrangian-Eulerian finite element formulation for incompressible viscous flows. *Computer Methods in Applied Mechanics and Engineering*, 29:329–349, 1981.
- A. S. Iglesias, L. P. Rojas, and R. Z. Rodriguez. Simulation of anti-roll tanks and sloshing type problems with smoothed particle hydrodynamics. *Ocean Engineering*, 31:1169–1192, 2004.
- A. Iserles. *A first course in the numerical analysis of differential equations*. Cambridge University Press, 2 edition, 2009.
- S. Ito. Study of the Transient Heave Oscillation of a Floating Cylinder. Master’s thesis, Massachusetts Institute of Technology, 1977.
- A. Kang, P. Lin, Y. J. Lee, , and B. Zhu. Numerical simulation of wave interaction with vertical circular cylinders of different submergences using immersed boundary method. *Computers and Fluids*, 106:41–53, 2014.
- M. Kashiwagi. Full-nonlinear simulations of hydrodynamics forces on a heaving two-dimensional body. *Journal of the Society of Naval Architects of Japan*, 180:373–381, 1996.

- M. Kashiwagi. A time-domain nonlinear simulation method for wave-induced motions of a floating body. *Journal of the Society of Naval Architects of Japan*, 184:139–148, 1998.
- M. Kashiwagi. Non-linear simulations of wave-induced motions of a floating body by means of the mixed Eulerian-Lagrangian method. In *Proceedings of the Institution of Mechanical Engineers, Part C: Journal of Mechanical Engineering*, 2000.
- M. Kashiwagi, A. Mizokami, H. Yasukawa, and Y. Fukushima. Prediction of wave pressure and loads on actual ships by the enhanced unified theory. In *23rd Symposium on Naval Hydrodynamics*, pages 368–384, 2000.
- C. H. Kim, A. H. Clement, and K. Tanizawa. Recent research and development of numerical wave tanks - a review. *International Journal of Offshore and Polar Engineering*, 9, 1999.
- J. Kim, D. Kim, and H. Choi. An immersed-boundary finite-volume method for simulations of flow in complex geometries. *Journal of Computational Physics*, 171:132–150, 2001.
- K. M. T. Kleefsman, G. Fekken, A. E. P. Veldman, and B. Iwanowski. An improved volume-of-fluid method for wave impact problems. In *14th International Offshore and Polar Engineering Conference*, 2004.
- K. M. T. Kleefsman, G. Fekken, A. E. P. Veldman, B. Iwanowski, and B. Buchner. A Volume-of-fluid based simulation method for wave impact problems. *Journal of Computational Physics*, 206:363–393, 2005.
- S. Kontos. *Robust numerical methods for nonlinear wave-structure interaction in a moving frame of reference*. PhD thesis, Technical University of Denmark, 2016.
- S. Kontos, H. B. Bingham, O. Lindberg, and A. P. Engsig-Karup. A robust WENO scheme for nonlinear waves in a moving reference frame. *Journal of Hydrodynamics*, 28:482–488, 2016.
- W. Koo and M.-H. Kim. Freely floating-body simulation by a 2D fully nonlinear numerical wave tank. *Ocean Engineering*, 31:2011–2046, 2004.
- W. Koo and M.-H. Kim. Fully nonlinear wave-body interactions with surface-piercing bodies. *Ocean Engineering*, 34:1000–1012, 2006.
- S. Koshizuka, A. Nobe, and Y. Oka. Numerical analysis of breaking waves using the moving particle semi-implicit method. *International Journal for Numerical Methods in Fluids*, 26: 751–769, 1998.
- J. H. Kyoung, S. Y. Hong, and B. W. Kim. Finite element method for time domain analysis on hydroelastic response of VLFS with fully nonlinear free surface conditions. In *16th International Offshore and Polar Engineering Conference*, 2006.
- W. Laskowski, H. B. Bingham, and A. P. Engsig-Karup. Modelling of Wave-structure Interaction for Cylindrical Structures using a Spectral Element Multigrid Method. In *34th International Workshop on Water Waves and Floating Bodies*, 2019.

- J. Lee, J. Kim, H. Choi, and K.-S. Yang. Sources of spurious force oscillations from an immersed boundary method for moving-body problems. *Journal of Computational Physics*, 230:2677–2695, 2011.
- L. Letournel, G. Ducrozet, A. Babair, and P. Ferrant. Proof of the equivalence of Tanizawa-Berkvens' and Cointe-van Daalen's formulations for the time derivative of the velocity potential for non-linear potential flow solvers. *Applied Ocean Research*, 63:184–199, 2017.
- R. W. Lewis, Y. Zheng, and D. T. Gethin. Three-dimensional unstructured mesh generation: Part 3. Volume meshes. *Computers Methods in Applied Mechanics and Engineering*, 134:285–310, 1996.
- B. Li and C. A. Fleming. A three dimensional multigrid model for fully nonlinear water waves. *Coastal Engineering*, 30:235–258, 1997.
- C.-C. Liao, Y.-W. Chang, C.-A. Lin, and J. M. McDonough. Simulating flows with moving rigid boundary using immersed-boundary method. *Computers & Fluids*, 39:152–167, 2010.
- P. Lin. A multiple-layer  $\sigma$ -coordinate model for simulation of wave-structure interaction. *Computers and Fluids*, 35:147–167, 2005.
- W. M. Lin. *Nonlinear Motion of The Free Surface Near A Moving Body*. PhD thesis, Massachusetts Institute of Technology, 1984.
- W. M. Lin, J. N. Newman, and D. K. Yue. Nonlinear forced motions of floating bodies. In *15th Symposium on Naval Hydrodynamics*, 1984.
- O. Lindberg, H. B. Bingham, and A. P. Engsig-Karup. Towards real time simulation of ship-ship interaction - Part III: Immersed body boundary condition and double body ship-ship interaction. In *29th International Workshop on Water Waves and Floating Bodies*, 2014.
- Y. Liu, M. Xue, and D. K. P. Yue. Computations of fully nonlinear three-dimensional wave-wave and wave-body interactions. Part 2: Nonlinear waves and forces on a body. *Journal of Fluid Mechanics*, 438:41–66, 2001.
- M. S. Longuet-Higgins and E. D. Cokelet. The deformation of steep surface waves on water I. A numerical method of computation. *Proceedings of the Royal Society of London A: Mathematical, Physical and Engineering Sciences*, 350:1–26, 1976.
- H. Luo, H. Dai, P. J. S. A. Ferreira de Sousa, and B. Yin. On the numerical oscillation of the direct-forcing immersed-boundary method for moving boundaries. *Computers & Fluids*, 56:61–76, 2012.
- R. Luquet, G. Ducrozet, L. Gentz, P. Ferrant, and B. Alessandrini. Applications of the SWENSE method to seakeeping simulations in irregular waves. In *9th International Conference on Numerical Ship Hydrodynamics*, 2007.
- Q. W. Ma and S. Yan. Quasi ALE finite element method for nonlinear water waves. *Journal of Computational Physics*, 212:52–72, 2006.

- Q. W. Ma and S. Yan. QALE-FEM for numerical modelling of non-linear interaction between 3D moored floating bodies and steep waves. *International Journal for Numerical Methods in Engineering*, 78:713–756, 2009a.
- Q. W. Ma and S. Yan. QALE-FEM for numerical modelling of non-linear interaction between 3D moored floating bodies and steep waves. *International Journal for Numerical Methods in Engineering*, 78:221–226, 2009b.
- S. Ma, F. C. W. Hanssen, M. A. Siddiqui, M. Greco, and O. M. Faltinsen. Local and global properties of the harmonic polynomial cell method: In-depth analysis in two dimensions. *International Journal for Numerical Methods in Engineering*, 113:681–718, 2018.
- O. S. Madsen. Waves Generated by a Piston Type Wavemaker. In *12th Conference on Coastal Engineering*, 1970.
- O. S. Madsen. On the Generation of Long Waves. *Journal of Geophysical Research*, 36:8672–8683, 1971.
- S. R. Masterton and C. Swan. On the accurate and efficient calibration of a 3D wave basin. *Ocean Engineering*, 35:763–773, 2008.
- J. J. Monaghan. Smoothed particle hydrodynamics. *Reports on Progress in Physics*, 68:1703–1759, 2005.
- J. J. Monaghan and A. Kos. Solitary waves on a cretan beach. *Journal of Waterway, Port, Coastal, and Ocean Engineering*, 215, 1999.
- W. I. Moubayed and A. N. Williams. Second-order Bichromatic Waves Produced by a Generic Planar Wavemaker in a Two-Dimensional Wave Flume. *Journal of Fluids and Structures*, 8:73–92, 1994.
- J. N. Newman. The theory of ship motions. *Advances in Applied Mechanics*, 18:221–283, 1978.
- J. N. Newman. *Marine Hydrodynamics, 40th Anniversary Edition*. The MIT Press, 2017.
- J. N. Newman and P. Sclavounos. The unified theory of ship motions. In *13th Symposium on Naval Hydrodynamics*, pages 373–394, 1980.
- Y. Nishi, C. Hu, and M. Kashiwagi. Multigrid technique for numerical simulations of water impact phenomena. *International Journal of Offshore and Polar Engineering*, 16:283–289, 2006.
- G. Oger, M. Doring, B. Alessandrini, and P. Ferrant. An improved SPH method: Towards higher order convergence. *Journal of Computational Physics*, 225:1472–1492, 2007.
- S. Osher and J. A. Sethian. Fronts propagating with curvature-dependent speed - algorithms based on Hamilton-Jacobi formulations. *Journal of Computational Physics*, 79:12–49, 1988.
- D. Pan and T.-T. Shen. Computation of incompressible flows with immersed bodies by a simple ghost cell method. *International Journal for Numerical Methods in Fluids*, 60:1378–1401, 2009.

- J. C. Park, M. H. Kim, and H. Miyata. Fully non-linear free-surface simulations by a 3D viscous numerical wave tank. *International Journal for Numerical Methods in Fluids*, 29:685–703, 1999.
- J. C. Park, M. H. Kim, and H. Miyata. Three-dimensional numerical wave tank simulations on fully nonlinear wave-current-body interactions. *Journal of Marine Science and Technology*, 6:70–82, 2001.
- J. C. Park, M. H. Kim, H. Miyata, and H. H. Chun. Fully nonlinear numerical wave tank (NWT) simulations and wave run-up prediction around 3-D structures. *Ocean Engineering*, 30:1969–1996, 2003.
- J. E. Pilliod and E. G. Puckett. Second-order accurate volume-of-fluid algorithms for tracking material interfaces. *Journal of Computational Physics*, 199:465–502, 2004.
- R. Porter. The solution to water wave scattering and radiation problems involving semi-immersed circular cylinders. Technical report, University of Bristol, 2008.
- R. W. Read and H. B. Bingham. An overset grid approach to linear wave-structure interaction. In *31st International Conference on Ocean, Offshore and Arctic Engineering*, 2012.
- I. Robertson and S. Sherwin. Free-surface flow simulation using hp/spectral elements. *Journal of Computational Physics*, 155:26–53, 1999.
- E. Rouy and A. Tourin. A viscosity solutions approach to shape-from-shading. *SIAM Journal on Numerical Analysis*, 29:867–884, 1992.
- N. Salvesen, E. O. Tuck, and O. Faltinsen. Ship motions and sea loads. *Transactions of the Society of Naval Architects and Marine Engineers*, 78:250–287, 1970.
- C. M. Sanchez, A. P. Engsig-Karup, and C. Eskilsson. Nonlinear wave-body interaction using a mixed-eulerian-lagrangian spectral element model. In *37th International Conference on Ocean, Offshore and Arctic Engineering*, 2018.
- Y. Sato and B. Niceno. A conservative local interface sharpening scheme for the constrained interpolation profile method. *International Journal for Numerical Methods in Fluids*, 70:441–467, 2012.
- A. Savitzky and M. J. E. Golay. Smoothing and Differentiation of Data by Simplified Least Squares Procedures. *Analytical Chemistry*, 36:1627–1639, 1964.
- N. Sayma. *Computational Fluid Dynamics*. DONG energy, 2013.
- R. Scardovelli and S. Zaleski. Direct numerical simulation of free-surface and interfacial flow. *Annual Review Fluid Mechanics*, 31:567–603, 1999.
- H. A. Schäffer. Second-order wavemaker theory for irregular waves. *Ocean Engineering*, 23:47–88, 1996.

- H. A. Schäffer and C. M. Steenberg. Second-order wavemaker theory for multidirectional waves. *Ocean Engineering*, 30:1203–1231, 2003.
- P. D. Sclavounos. The diffraction of free-surface waves by a slender ship. *Journal of Ship Research*, 28 (1):29–47, 1984.
- H. Segur, D. Henderson, J. Carter, J. Hammack, C. M. Li, D. Pheiff, and K. Socha. Stabilizing the Benjamin-Feir instability. *Journal of Fluid Mechanics*, 539:229–271, 2005.
- J. A. Sethian and P. Smereka. Level set methods for fluid interfaces. *Annual Review Fluid Mechanics*, 35:341–372, 2003.
- Y. Shao and O. M. Faltinsen. A harmonic polynomial cell (HPC) method for 3D Laplace equation with application in marine hydrodynamics. *Journal of Computational Physics*, 274:312–332, 2014.
- Y. Shirakura, K. Tanizawa, and S. Naito. Development of 3-d fully nonlinear numerical wave tank to simulate floating bodies interacting with water waves. In *10th International Offshore and Polar Engineering Conference*, 2000.
- J. Skourup and H. A. Schäffer. Wave generation and active absorption in a numerical wave flume. In *7th International Offshore and Polar Engineering Conference*, 1997.
- A. Soulaimani and Y. Saad. An arbitrary Lagrangian-Eulerian finite element method for solving three-dimensional free surface flows. *Computer Methods in Applied Mechanics and Engineering*, 162:79–106, 1998.
- M. Souli and J. P. Zolesio. Arbitrary Lagrangian-Eulerian and free surface methods in fluid mechanics. *Computer Methods in Applied Mechanics and Engineering*, 191:451–466, 2001.
- G. G. Stokes. On the theory of oscillatory waves. *Transactions of the Cambridge Philosophical Society*, 8:441–455, 1847.
- M. Sueyoshi, M. Kashiwagi, and S. Naito. Numerical simulation of wave-induced nonlinear motions of a two-dimensional floating body by the moving particle semi-implicit method. *Journal of Marine Science and Technology*, 13:85–94, 2008.
- M. Sussman and E. Fatemi. An efficient, interface preserving level set re-distancing algorithm and its application to interfacial incompressible fluid flow. *SIAM Journal on Scientific Computing*, 20:1165–1191, 1999.
- M. Sussman and E. G. Puckett. A coupled level set and volume-of-fluid method for computing 3D and axisymmetric incompressible two-phase flows. *Journal of Computational Physics*, 162:301–337, 2000.
- M. Sussman, P. Smereka, and S. Osher. A level set approach for computing solutions to incompressible two-phase flow. *Journal of Computational Physics*, 114:146–159, 1994.

- M. Sussman, A. S. Almgren, J. B. Bell, P. Colella, L. H. Howell, and M. L. Welcome. An adaptive level set approach for incompressible two-phase flows. *Journal of Computational Physics*, 148: 81–124, 1999.
- H. Takewaki and T. Yabe. The cubic-interpolated pseudo particle (CIP) method: application to nonlinear and multi-dimensional hyperbolic equations. *Journal of Computational Physics*, 70: 355–372, 1987.
- H. Takewaki, A. Nishiguchi, and T. Yabe. Cubic interpolated pseudo-particle method (CIP) for solving hyperbolic-type equations. *Journal of Computational Physics*, 61:261–268, 1985.
- K. Tanizawa. A nonlinear simulation method of 3D body motions in waves. *Journal of the Society of Naval Architects of Japan*, 178:179–191, 1995.
- K. Tanizawa. Long Time Fully Nonlinear Simulation of Floating Body Motions with Artificial Damping Zone. *Journal of the Society of Naval Architects of Japan*, 180:311–319, 1996.
- K. Tanizawa. An Application of Fully Nonlinear Numerical Wave Tank to the Study on Chaotic Roll Motions. In *8th International Offshore and Polar Engineering Conference*, 1998.
- K. Tanizawa and M. Minami. Development of a 3D-NWT for simulation of running ship motions in waves. In *16th International Workshop on Water Waves and Floating Bodies*, 2001.
- K. Tanizawa and H. Sawada. A Numerical method for Nonlinear Simulation of 2-D Body Motions in Waves by means of B. E. M. *Journal of the Society of Naval Architects of Japan*, 168:179–191, 1990.
- W. T. Tsai and D. K. P. Yue. Computation of nonlinear free-surface flows. *Annual Review Fluid Mechanics*, 1996.
- F. Ursell. On the Heaving Motion of a Circular Cylinder on the Surface of a Fluid. *Quarterly Journal of Mechanics and Applied Mathematics*, 2:215–231, 1949.
- F. Ursell, R. G. Dean, and Y. S. Yu. Forced small-amplitude water waves: a comparison of theory and experiment. *Journal of Fluid Mechanics*, 7:33–52, 1960.
- E. F. G. van Dalen. *Numerical and Theoretical Studies of Water Waves and Floating Bodies*. PhD thesis, University of Twente, The Netherlands, 1993.
- T. Verbrugghe, B. Devolder, J. M. Dominguez, A. Kortenhaus, and P. Troch. Feasibility study of applying SPH in a coupled simulation tool for wave energy converter arrays. In *12th European Wave and Tidal Energy Conference*, 2017.
- T. Vinje and P. Brevig. Nonlinear Ship Motions. In *3rd International Conference on Numerical Ship Hydrodynamics*, 1981.
- M. Vinokur. On one-dimensional stretching functions for finite-difference calculations. *Journal of Computational Physics*, 50:215–234, 1983.

- A. Vire, J. SPinneken, M. D. Piggott, C. C. Pain, and S. C. Kramer. Modelling of waves and wave-structure interactions using non-linear numerical models. In *11th World Congress on Computational Mechanics*, 2013.
- P. Wang, Y. Yao, and P. Tulin. An efficient numerical tank for non-linear water waves, based on the multi-subdomain approach with BEM. *International Journal for Numerical Methods in Fluids*, 20:1315–1336, 1995.
- S. Wang. Plunger-type Wavemakers: Theory and Experiment. *Journal of Hydraulic Research*, 12:3:357–388, 1974.
- W. Wang, H. Bihs, A. Kamath, and Ø. A. Arntset. Multi-directional irregular wave modelling with CFD. In *4th International Conference in Ocean Engineering*, 2018.
- J. Westphalen, D. M. Greaves, C. J. L. Williams, A. C. Hunt-Raby, and J. Zang. Focused waves and wave-structure interaction in a numerical wave tank. *Ocean Engineering*, 45:9–21, 2012.
- C. S. Wu, D. L. Young, and C. L. Chiu. Simulation of wave-structure interaction by hybrid cartesian/immersed boundary and arbitrary Lagrangian-Eulerian finite-element method. *Journal of Computational Physics*, 254:155–183, 2013.
- G. X. Wu and R. Eatock Taylor. Time stepping solutions of the two-dimensional nonlinear wave radiation problem. *Ocean Engineering*, 22:785–798, 1995.
- G. X. Wu and R. Eatock Taylor. Transient motion of a floating body in steep waves. In *11th International Workshop on Water Waves and Floating Bodies*, 1996.
- G. X. Wu and R. Eatock Taylor. The coupled finite element and boundary element analysis of nonlinear interactions between waves and bodies. *Ocean Engineering*, 30:387–400, 2003.
- Y. C. Wu. Plunger-type wavemaker theory. *Journal of Hydraulic Research*, 26:4:483–491, 1988.
- H. Xu, C. D. Cantwell, C. Monteserin, C. Eskilsson, A. P. Engsig-Karup, and S. J. Sherwin. Spectral/hp element methods: Recent developments, application, and perspectives. *Journal of Hydrodynamics*, 30:1–22, 2018.
- M. Xue, H. Xu, Y. Liu, and D. K. P. Yue. Computations of fully nonlinear three-dimensional wave-wave and wave-body interactions. Part 1: Dynamics of steep three-dimensional waves. *Journal of Fluid Mechanics*, 438:11–39, 2001.
- T. Yabe, F. Xiao, and T. Utsumi. The constrained interpolation profile method for multiphase analysis. *Journal of Computational Physics*, 169:556–593, 2001.
- H. Yan and Y. Liu. An efficient high-order boundary element method for nonlinear wave-wave and wave-body interactions. *Journal of Computational Physics*, 230:402–424, 2011.
- S. Yan. *Numerical simulation of nonlinear response of moored floating structures to steep waves*. PhD thesis, School of Engineering and Mathematical Sciences, City University, London, U.K., 2006.

- S. Yan and Q. W. Ma. Numerical simulation of fully nonlinear interaction between steep waves and 2D floating bodies using the QALE-FEM method. *Journal of Computational Physics*, 221: 666–692, 2007a.
- S. Yan and Q. W. Ma. Effects of an arbitrary sea bed on responses of moored floating structures to steep waves. In *17th International Offshore and Polar Engineering Conference*, 2007b.
- Z. Yang, S. Liu, H. B. Bingham, and J. Li. Second-order theory for coupling 2D numerical and physical wave tanks: Derivation, evaluation and experimental validation. *Coastal Engineering*, 71:37–51, 2013.
- Z. Yang, S. Liu, H. B. Bingham, and J. Li. Second-order coupling of numerical and physical wave tanks for 2D irregular waves. Part I: Formulation, implementation and numerical properties. *Coastal Engineering*, 92:48–60, 2014a.
- Z. Yang, S. Liu, H. B. Bingham, and J. Li. Second-order coupling of numerical and physical wave tanks for 2D irregular waves. Part II: Experimental validation in two-dimensions. *Coastal Engineering*, 92:61–74, 2014b.
- V. E. Zakharov. Stability of periodic waves of finite amplitude on the surface of a deep fluid. *Journal of Applied Mechanics and Technical Physics*, 9:190–194, 1968.
- H. Zhang and H. A. Schäffer. Approximate Stream Function wavemaker theory for highly nonlinear waves in wave flumes. *Ocean Engineering*, 34:1290–1302, 2007.
- J. Zhang and M. Kashiwagi. Application of ALE to nonlinear wave radiation by a non-wall-sided structure. *Journal of the Japan Society of Naval Architects and Ocean Engineers*, 25:109–121, 2017a.
- J. Zhang and M. Kashiwagi. Application of ALE to nonlinear wave diffraction by a non-wall-sided structure. In *27th International Ocean and Polar Engineering Conference*, 2017b.
- X. Zhang, N. M. Sudharsan, R. Ajaykumar, and K. Kumar. Simulation of free-surface flow in a tank using the Navier-Stokes model and unstructured finite volume method. *Proceedings of the Institution of Mechanical Engineers, Part C: Journal of Mechanical Engineering Science*, 219: 251–266, 2005.
- O. C. Zienkiewicz, R. L. Taylor, and J. Z. Zhu. *The finite element method: its basis and fundamentals*. Elsevier, 2013.

# A | Appendix A - Matrix integration with permutation

Starting with the computationally-adjacent ordering of body points

$$c = \begin{bmatrix} c_1 & c_2 & c_3 & c_4 & c_5 \end{bmatrix} \quad (\text{A.1})$$

These are sorted to physical adjacency

$$c_s = \begin{bmatrix} c_2 & c_4 & c_1 & c_5 & c_3 \end{bmatrix} \quad (\text{A.2})$$

with the permutation index

$$i_s = \begin{bmatrix} 3 & 1 & 5 & 2 & 4 \end{bmatrix} \quad (\text{A.3})$$

The integration matrix is built based on the sorted  $c_s$ , so the integration becomes

$$\begin{bmatrix} b_1 & b_2 & b_3 \\ b_4 & b_5 & b_6 \\ b_7 & b_8 & b_9 \\ b_{10} & b_{11} & b_{12} \\ b_{13} & b_{14} & b_{15} \end{bmatrix} \begin{bmatrix} c_2 \\ c_4 \\ c_1 \\ c_5 \\ c_3 \end{bmatrix} = \begin{bmatrix} b_1c_2 + b_2c_4 + b_3c_1 \\ b_4c_2 + b_5c_4 + b_6c_1 \\ b_7c_4 + b_8c_1 + b_9c_5 \\ b_{10}c_1 + b_{11}c_5 + b_{12}c_3 \\ b_{13}c_1 + b_{14}c_5 + b_{15}c_3 \end{bmatrix} \quad (\text{A.4})$$

When this is multiplied by the unit vector we have

$$\begin{aligned} c_1(b_3 + b_6 + b_8 + b_{10} + b_{13}) + c_2(b_1 + b_4) + c_3(b_{12} + b_{15}) + \dots \\ c_4(b_2 + b_5 + b_7) + c_5(b_9 + b_{11} + b_{14}) \end{aligned} \quad (\text{A.5})$$

So if we start by multiplying the integration matrix with the unit vector we have

$$\begin{bmatrix} b_1 + b_4 & b_2 + b_5 + b_7 & b_3 + b_6 + b_8 + b_{10} + b_{13} & b_9 + b_{11} + b_{14} & b_{12} + b_{15} \end{bmatrix} \begin{bmatrix} c_2 \\ c_4 \\ c_1 \\ c_5 \\ c_3 \end{bmatrix} \quad (\text{A.6})$$

which requires the permutation

$$i_s = \begin{bmatrix} 3 & 1 & 5 & 2 & 4 \end{bmatrix} \quad (\text{A.7})$$

in order to be used with the original  $c$ .

## B | Appendix B - Second-order transfer function

Schäffer (1996) second-order transfer function definitions.

$$\begin{aligned} \mathcal{F}^\pm = E^\pm & \left\{ \mp \frac{g}{2\omega_n} \sum_{j=0}^{\infty} c_{jn} \frac{k_{jn}^2}{k_{jn}^2 - (K_0^\pm)^2} (\omega_n^2 - (\omega_n \pm \omega_m)^2 + M_2(k_{jn}, K_0^\pm)) + \widehat{lmjn}^{-: *} \right. \\ & \left. + \sum_{j=0}^{\infty} \sum_{l=0}^{\infty} c_{jn} c_{lm}^{-: *} \frac{k_{jn} \pm k_{lm}^{-: *}}{(k_{jn} \pm k_{lm}^{-: *})^2 - (K_0^\pm)^2} H_{jnlm}^\pm \right\}, \end{aligned} \quad (\text{B.1})$$

where

$$E^\pm = \frac{\delta_{nm}(K_0^\pm)^2 h}{c_{0n} c_{0M} (\omega_n \pm \omega_m)^3 (1 + M_1(K_0^\pm))} \quad (\text{B.2})$$

and

$$M_1(K_0^\pm) \equiv \frac{1}{h+l} \frac{g}{(\omega_n + \omega_m)^2} \left( \frac{\cosh(K_0^\pm d)}{\cosh(K_0^\pm h)} - 1 \right). \quad (\text{B.3})$$

In the preceding three equations the subscripts  $n$  and  $m$  refer to the two wave components comprising the second-order spectrum, which contains both superharmonic and subharmonic interaction terms (sum and difference frequencies, respectively). Schäffer (1996) introduces two shorthand notations:  $\widehat{lmjn}$  is defined as “the preceding term permuting  $l$  and  $j$  as well as  $m$  and  $n$ ”; and the symbol  $- : *$  is defined by

$$Z^{-: *} = \begin{cases} Z & \text{for superharmonics} \\ Z^* & \text{for subharmonics,} \end{cases} \quad (\text{B.4})$$

where  $*$  denotes complex conjugation. The term  $c_j$  is the first-order transfer function given by

$$c_j = \left( \frac{\omega^2 h}{g} - \frac{h}{h+l} \right) \frac{1}{D_j(k_j)} + \frac{h}{h+l} \frac{1}{D_j(k_j)} \frac{\cosh(k_j d)}{\cosh(k_j h)}, \quad (\text{B.5})$$

where  $k_{jn}, k_{jm}$  are the imaginary solutions to the dispersion relation  $\omega^2 = gk_j \tanh(k_j h)$ , corresponding to  $\omega_n$  and  $\omega_m$  respectively. Finally,  $h$  denotes the still water depth,  $z = -(h+l)$  gives the wavemaker centre of rotation, and  $d \geq 0$  is the elevation of the hinge over the bottom. A piston wavemaker will thus be characterized by  $l = \infty$  and  $d = 0$ .

# C | Appendix C - Numerical frameworks and techniques

Whatever method is used to solve the partial differential equations (PDEs) that describe a system, the following requirements must be satisfied:

1. Consistency
2. Stability
3. Convergence

## Consistency

For a numerical discretization to be consistent, it should tend to the differential equation which it is related to as  $\Delta x$  and  $\Delta t$  tend to zero. One way of checking consistency is to use a Taylor series expansion of all terms, with the higher order terms retained. This expansion is then substituted into the discretized equation and the resulting equation is checked for consistency (i.e. that it tends to the original differential equation as  $\Delta x$  and  $\Delta t$  tend to zero).

## Stability

Stability is the tendency of any perturbations in the solution of the discretized system of equations to decay. A particular method is stable if the cumulative effect of round-off errors produced in the application of the numerical algorithm is negligible, or does not build up continuously at every time step. The three most common methods of stability analysis are the method of equivalent differential equations, the matrix method, and the von-Neumann method (see Hirsch 1988). An alternative interpretation is to assume that the initial conditions are represented by a Fourier series. Each harmonic in the Fourier series will decay or grow depending on the discretized equation, which typically leads to a specific expression for the growth or decay factor for each mode. If one mode can grow without bounds, the solution will be unstable (see Fletcher 1991).

## Convergence

Convergence means that the numerical solution should approach the exact solution of the differential equation at any point in the domain when  $\delta x$  and  $\delta t$  approach zero. That is to say, the error in the solution should be reduced as the discretization parameters are refined. This is often difficult to prove as analytic solutions are not known. For steady problems, the residual (difference between solution at successive iterations) is required to approach zero. This only means that the solution to the system of discretized algebraic equations has been obtained, which is not necessarily the exact solution. An alternative way of assessing convergence is grid independence, or mesh

convergence: successive solutions are obtained on finer and finer grids until the solution variance from one grid to the next approaches a prescribed tolerance.

## C.1 Numerical methods

### C.1.1 Finite difference

#### Selected papers

Vinokur (1983), Hirt et al. (1997), Fornberg (1998), Fuhrman and Bingham (2004), Kleefsman et al. (2004, 2005), Bingham and Zhang (2007), Bingham et al. (2007), Engsig-Karup et al. (2009), Ducrozet et al. (2010, 2014), Kang et al. (2014), Kontos (2016); Kontos et al. (2016), Bihs et al. (2016), Amini-Ashfar et al. (2019), Wang et al. (2018).

#### Theory

Approximates derivatives in a differential equation using a truncated Taylor series

$$f(x + \Delta x) = f(x) + \Delta x f'(x) + \Delta x^2 \frac{f''(x)}{2!} + \Delta x^{n-1} \frac{f^{n-1}(x)}{(n-1)!} + O(\Delta x^n) \quad (\text{C.1})$$

For geometries with boundaries that do not coincide with a structured grid, a body-fitted grid may be generated in the physical plane and then mapped to a regular grid in the computational plane.

#### Accuracy

The error in a finite difference scheme may be reduced by refining the grid, or by reducing the truncation error (i.e. increasing the stencil size and thereby including more terms in the Taylor series expansion).

#### Advantages

- Relatively simple to implement.
- Can achieve  $O(N)$  computational effort.

#### Disadvantages

- Requires a logically structured grid (although curvilinear coordinate system may also be used).
- Not straightforward to introduce complex geometries.

### C.1.2 Finite element

#### Selected papers

Zienkiewicz et al. (2013), Broderick and Leonard (1992), Kyoung et al. (2006), Westphalen et al. (2012), Vire et al. (2013).

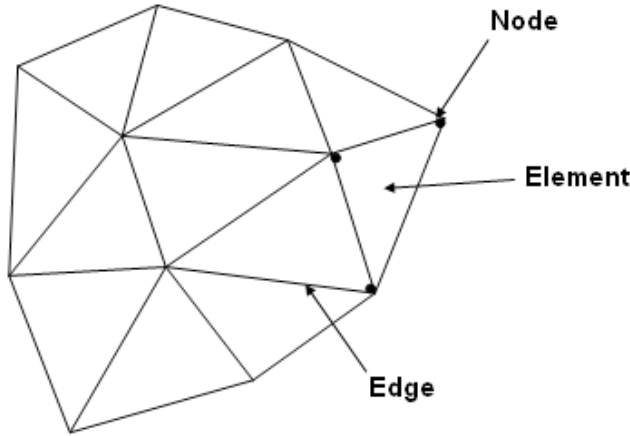


**Figure C.1:** Typical two-dimensional finite element mesh Sayma (2013).

### Theory

Based on the "Method of Weighted Residuals". Taking the steady state convection-diffusion equation as an example:

$$u \frac{\partial T}{\partial x} - \alpha \frac{\partial^2 T}{\partial x^2} = 0, \quad (\text{C.2})$$

we can express this in symbolic form as

$$Q(T) = 0 \quad (\text{C.3})$$

We seek an approximate solution  $T'$  using a trial function of some form. This will not satisfy (C.3), so a residual appears:

$$Q(T') = R \quad (\text{C.4})$$

The "Weighted Residual Method" is therefore based on the concept of introducing a weighting function and then requiring that the integral of the weighted residual vanishes over the whole solution domain.

$$\int_{\Omega} W Q(T') d\Omega = 0. \quad (\text{C.5})$$

For example, if the trial function is a polynomial with a number of unknown coefficients, then by selecting a succession of trial functions and integrating, a number of equations can be created which can be solved simultaneously to obtain the coefficients of the polynomial, thus resulting in the solution. This implies that the finite element method can be used to obtain analytic solutions to differential equations provided suitable trial and weighting functions can be found. Different techniques to define the trial and weighting functions are, for example, the Sub-domain Method, the Collocation Method, the Least-Square Method, and the Galerkin Method.

### Galerkin method

The Galerkin method assumes that the trial and weighting functions are the same. The first step is to assume local trial functions over the solution domain (in one dimension these can be line segment between grid points). The trial functions are then interpolation (or shape) functions which assume the shape of the variation of the field variable between the grid points comprising

the cell (the simplest of which being linear shape functions that assume the field variable has a linear variation between grid points). The solution could then be expressed as  $T'(x) = T_i N_i(x)$ , where  $N_i$  is the interpolation function at node  $i$  and  $T_i$  is the sought solution. Choosing a series of weighting functions that have the value of  $W^i$  at node  $i$  and zero elsewhere leads to an expression of the discrete weighted residual form by substituting into (C.5)

$$\int_{\Omega} \lim W^i Q(T_i N_i(x)) d\Omega = 0. \quad (\text{C.6})$$

Integrating at all domain cells produces a system of algebraic equations of the form  $K \cdot T_i = r$ , which can be solved for the coefficients  $T_i$  representing the field function at the nodal points. The matrix  $K$  is the Jacobian or Mass matrix, and  $r$  contains boundary conditions and source terms as appropriate.

### Advantages

- Naturally allows for handling arbitrary complex geometries as it can be easily applied using irregular grids of various shapes.
- Provides a set of functions that give the variation of the differential equations between grid points, where finite difference provides information for the values at grid points only.
- Weak formulation (of integral form of governing equations) when using linear shape functions: second derivative of linear function is zero, so integration by parts must be used<sup>1</sup>.

### Disadvantages

- Slightly more complex to implement than finite difference.
- Potentially high storage requirements for system matrix of unstructured grids.
- Generally limited to second-order accuracy.

### C.1.3 Spectral method

#### Selected papers

Dommermuth and Yue (1987), Robertson and Sherwin (1999), Engsig-Karup et al. (2016), Engsig-Karup et al. (2017), Sanchez et al. (2018), Xu et al. (2018).

#### Theory

The fundamental idea behind spectral methods is to approximate solutions of PDEs by finite series of orthogonal (basis) functions such as the complex exponentials (for smooth, periodic problems), Chebyshev or Legendre polynomials (for smooth, non-periodic problems). The approximations can be *modal*, where the fundamental unknowns are the coefficients of the orthogonal expansion functions (modes), or *nodal*, where the solution is represented in terms of grid point values by way of an interpolant. Nodal approximations are tied to the introduction of a quadrature rule. To handle complex geometries the domain of interest can be divided into smaller subdomains that can

---

<sup>1</sup>see Computational Fluid Dynamics - Naser Sayma.

be mapped individually onto the square. The nodal Galerkin method can then be used with these subdomains.<sup>2</sup>

### Advantages

- Can display spectral (exponential) convergence for suitably smooth basis functions.
- Can handle complex geometries via multidomain methods (which can also eliminate discontinuous coefficients or solutions by appropriate arrangement of subdomains).
- Both single and multidomain methods allow for parallelisation.

### Disadvantages

- May require de-aliasing, due to PDE aliasing (relating to quasi-linear and nonlinear terms), geometrical aliasing (due to deformed/curved elements), and interface-flux aliasing (in the case of discontinuous methods). However, this is not specific to spectral methods.
- Requires mild spectral filtering to secure robustness for marginally resolved flows.

## C.1.4 Finite volume

### Selected papers

Hirt and Nichols (1981), Kim et al. (2001), Kleefsman et al. (2005), Zhang et al. (2005), Chung (2006, 2013), Ai and Jin (2010), Westphalen et al. (2012).

### Theory

The finite volume method be viewed as a special case of Weighted Residual Method, where the weighting function takes the form  $W^i = 1$ . A number of weighted residual equations are generated by dividing the solution domain into subdomains called 'control volumes' and setting the weighting function to be unity over the control volumes one at a time, and zero elsewhere. This implies that the residual over each volume must become zero. The finite volume formulation is based on the fact that the variation of any quantity within a volume depends entirely on the surface values of the fluxes. The solution domain is discretized into small volumes, and the integral form of the conservation laws for each volume is written separately. Global conservation can then be recovered by adding up the fluxes of the sub-volumes. For a control volume  $\Omega$  with surface boundary  $\Gamma$ , the integral form of the continuity equation is

$$\frac{\partial}{\partial t} \int_{\Omega} \rho d\Omega + \oint_{\Gamma} \rho \vec{U} d\Gamma, \quad (\text{C.7})$$

where  $\vec{U} = \vec{u} + \vec{v} + \vec{w}$ . Similarly, the integral formulation of the  $x$ -momentum equation is

$$\frac{\partial}{\partial t} \int_{\Omega} \rho d\Omega + \oint_{\Gamma} \left( \rho \vec{U} + p - \tau \right) d\Gamma, \quad (\text{C.8})$$

---

<sup>2</sup>From "Implementing Spectral Methods for PDEs", Kopriva 2009 & "Spectral Methods", Canuto et al. 2008

where  $\tau$  is the viscous flux given by

$$\tau = \mu \left( \frac{\partial u}{\partial x} + \frac{\partial u}{\partial y} + \frac{\partial u}{\partial z} \right) \quad (\text{C.9})$$

### Note on numerical diffusion

Central difference schemes are unstable for advection/convection problems, and need to be replaced by upwind schemes. In a finite volume framework, the advection term of the steady state heat equation in one dimension may be described by

$$(\rho u \theta)_e - (\rho u \theta)_w, \quad (\text{C.10})$$

where  $\rho$  is the density,  $u$  the convective velocity, and  $\theta$  any flow variable, such as velocity in a given direction or temperature. For a positive value of  $u$ , the upwind version of (C.10) becomes

$$(\rho u)_e \theta_P - (\rho u)_w \theta_W. \quad (\text{C.11})$$

Assuming, without loss of generality, that  $(\rho u) = 2$ , (C.11) becomes

$$2\theta_P - 2\theta_W = \theta_P + \theta_P - \theta_W - \theta_W. \quad (\text{C.12})$$

Adding and subtracting  $\theta_E$  from the right hand side:

$$2\theta_P - 2\theta_W = \theta_P + \theta_P - \theta_W - \theta_W + \theta_E - \theta_E. \quad (\text{C.13})$$

Now regrouping the terms on the right hand side we have

$$(\theta_E - \theta_W) - (\theta_E + \theta_W - 2\theta_P). \quad (\text{C.14})$$

The first term is proportional to a central difference second order scheme of the first derivative of the field variable, while the second term is proportional to the second derivative of the field variable. Hence the first order upwind scheme for the advection term seems to be a discretization of the term

$$\frac{d\theta}{dx} + \alpha \frac{d^2\theta}{dx^2}. \quad (\text{C.15})$$

An unstable central difference scheme has thus been stabilized by the addition of a diffusion term. The diffusion term is not physical, but rather numerical. The second conclusion is that the reason behind the dissipation of the solution when a first order one-sided scheme was used is the implicitly added numerical dissipation. The early schemes of this type (i.e. adding a small amount of numerical dissipation sufficient to stabilize the scheme) are called Lax-Windroff schemes (see Hirsch 1990).

### Advantages

- Complex geometries can be handled easily.

### Disadvantages

- Many cells needed when field variable changes quickly with the space coordinate.

### C.1.5 Boundary element

#### Selected papers

Costabel (1986), Cao et al. (1994), Wu and Taylor (1995), Wang et al. (1995), Tsai and Yue (1996), Kashiwagi (2000), Xue et al. (2001), Ferrant et al. (2003), Skourup and Schäffer (1997), Christou (2009), Ma and Yan (2009a), Kim et al. (1999), Yan and Liu (2011), He and Kashiwagi (2013, 2014a,b), Harris et al. (2014).

#### Theory

A typical boundary element method has the following steps/parts:

- Mathematical model (convenient to choose homogeneous differential equation with inhomogeneous boundary data - for example Laplace equation with Dirichlet boundary conditions)
- Represent the solution of the PDE in the domain by means of boundary potentials; i.e. using Green's identities
- Insert the representation formulas into the boundary conditions to get boundary integral equations
- Define boundary elements
- Develop discrete equations by e.g. collocation, Galerkin, or least-squares
- Solve the linear system (which is typically not sparse)

#### Advantages

- Only the boundary of the domain needs to be discretized; this means that the problem dimensionality is reduced by one unit (as compared to finite element methods for example).
- The solution in the interior is approximated with a rather high convergence rate, and the same rate of convergence holds for all derivatives of any order of the solution in the domain.
- Complex geometries are not a problem.

#### Disadvantages

- Requires explicit knowledge of a fundamental solution to the differential equation.
- If the boundary is not smooth but has corners and edges, then the solution of the boundary value problem has singularities at the boundary. Kashiwagi (1998) proposed solving an acceleration potential simultaneously with the velocity potential, by introducing double points at body-free-surface intersections. The acceleration potential at the double node is assumed to be single-valued, but its normal derivative can be different on the body/free-surface.
- According to Tsai and Yue (1996) and Shao and Faltinsen (2014), the computational burden is dominated by the evaluations of the boundary-integration influence coefficients, requiring  $O(N^2)$  storage and  $O(N^2)$  solution effort. Kim et al. (1999) mention an improvement by Korsmeyer et al. (1996), that reduces the asymptotic computational effort to  $O(N \log N)$ . The Fast Multipole Method has also been implemented, which could bring computational cost down to  $O(N)$  (see Harris et al. (2014) and Shao and Faltinsen (2014)).

### C.1.6 Smooth Particle Hydrodynamics

#### Selected papers

Monaghan and Kos (1999), Iglesias et al. (2004), Monaghan (2005), Dalrymple and Rogers (2006), Oger et al. (2007), Abdelrazek and Kimura (2014), Verbrugghe et al. (2017).

#### Theory

A gridless/meshless method that models solids and fluids via Lagrangian particles. Each particle has a position, velocity, and mass, and is governed by the Navier-Stokes or Euler equations. The SPH equations are obtained from the continuum equations of fluid dynamics by interpolating from a set of points that may be disordered. The interpolation is based on the theory of integral interpolants using interpolation kernels that approximate a delta function. The interpolants are analytic functions that can be differentiated without the use of grids. If the points are fixed in position, the equations are identical to finite difference equations, with different forms depending on the interpolation kernel. The SPH equations describe the motion of the interpolating points, which can be thought of as particles. The resolution of the method is determined by changing the width of the kernel, with the error being approximately inversely proportional to the number of particles covered by the kernel. A correction must be included when calculating the rate of change of particle position to ensure a stable free surface.

#### Advantages

- Can model wave breaking.
- Can model both fluid and solids; hence wave-structure interaction.

#### Disadvantages

- Prohibitive computational cost for large problems due to number of particles required for sufficient resolution (although an efficient parallel implementation can offset this).
- Free-surface flows exhibit stability problems.
- Lack of convergence for free-surface flows.

### C.1.7 Moving Particle Semi-Implicit

#### Selected papers

Koshizuka et al. (1998), Sueyoshi et al. (2008), Abdelrazek and Kimura (2014), Hashimoto et al. (2017).

## Theory

Governing equations are expressed by conservation laws of mass and momentum:

$$\frac{\partial \rho}{\partial t} = 0 \quad (\text{C.16})$$

$$\frac{D\mathbf{u}}{Dt} = -\frac{1}{\rho} \nabla P + \mathbf{f}. \quad (\text{C.17})$$

Particles interact with their neighbours covered by a weight function  $w(r)$ , where  $r$  is a distance between two particles. Interactions are restricted to a finite distance (i.e. finite number of neighbouring particles). Gradients are then modelled using a weight function over said distance. The Laplacian operator is modelled in a transient diffusion problem; part of a quantity  $\phi$  retained by a particle  $i$  is distributed to neighbouring particles  $j$  using the weight function. The model is therefore conservative. Density is modelled by the particle number density (i.e. the number of particles in a unit volume). A flowchart of the calculation algorithm is shown in Figure C.2.

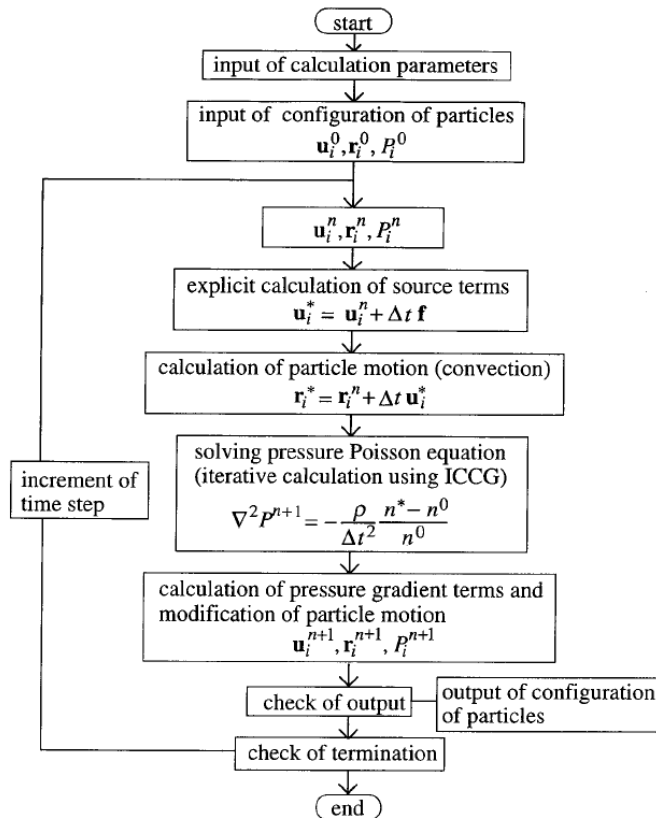


**Figure C.2:** Algorithm of original MPS method (Koshizuka et al. (1998)).

## Advantages

- Can model wave breaking and green water.
- Can model both fluid and solids.

## Disadvantages

- Must generate neighbour/distance list for all particles at every time step at  $O(N^2)$  cost ( $N$  particles). This can be reduced to  $O(N^{1.5}M^{0.5})$ , where  $M$  is average number of neighbouring particles covered by weight function.
- Iteration of solution also requires  $O(N^{1.5}M^{0.5})$  computational work.
- Free surface (and pressure distribution in fluid) can be unstable, requiring special treatment or tuning.

### C.1.8 CCUP: CIP-Combined and Unified Procedure

#### Selected papers

Yabe et al. (2001), Hu et al. (2003), Hu et al. (2005), Nishi et al. (2006), Hu et al. (2006), Nishi et al. (2006), Hu et al. (2008) Hu et al. (2010), He et al. (2011),

#### Theory

The hydrodynamic equations are written as

$$\frac{\partial \rho}{\partial t} + u_i \frac{\partial \rho}{\partial x_i} = -\rho \frac{\partial u_i}{\partial x_i} \quad (\text{C.18})$$

$$\frac{\partial u_i}{\partial t} + u_j \frac{\partial u_i}{\partial x_j} = \frac{1}{\rho} \frac{\partial \sigma_{ij}}{\partial x_j} + F_i \quad (\text{C.19})$$

$$\frac{\partial p}{\partial t} + u_i \frac{\partial p}{\partial x_i} = -\rho C_S^2 \frac{\partial u_i}{\partial x_i}, \quad (\text{C.20})$$

where  $C_S$  is the speed of sound and  $\sigma_{ij}$  is the total stress. The CCUP method solves the pressure by

$$\frac{\partial}{\partial x_i} \left( \frac{1}{\rho} \frac{\partial p}{\partial x_i} \right) = \frac{p - p'}{\rho C_S^2 \Delta t^2} + \frac{1}{\Delta t} \frac{\partial u'_i}{\partial x_i}, \quad (\text{C.21})$$

which is valid for fluid, gas, and solid phases. This means that boundary conditions for pressure at the interfaces between different phases are not necessary. The governing equations are solved by a fractional step approach: advection is solved first, then diffusion is calculated, and then pressure is solved. The advection calculation proceeds by the CIP (Constrained Interpolation Profile) method, where the basic idea is that, for a given value  $f$ , the advection equation of  $f$  and the advection equation of its spatial gradient  $q_i = \partial f / \partial x_i$  are calculated by a constrained polynomial interpolation method.

Moving body boundaries and the free surface boundary are distinguished by a density function  $\phi_m$ ,  $m = 1, 2, 3$  for liquid, gas, and solid phases, respectively:

$$\frac{\partial \phi_m}{\partial t} + u_i \frac{\partial \phi_m}{\partial x_i} = 0, \quad (\text{C.22})$$

which is solved with the CIP scheme. Rigid moving bodies are not solved in this way but rather treated in a Lagrangian manner, so the solid boundary position can be obtained accurately and  $\phi_3$  follows directly.

## Advantages

- Pressure-based algorithm that can treat multiphase flow field by one set of governing equations.
- Hydrodynamic forces can be easily computed.
- Green water can be modelled.
- Complex structures can be modelled (ISOPE 2008).

## Disadvantages

- Based on CIP, so also requires sharpness enhancement technique at phase interface.
- Interface smearing due to numerical diffusion in advection terms.
- High computational cost at high resolution (see ISOPE 2010 paper).

## C.2 Interface capturing

### C.2.1 VOF (Volume of Fluid)

#### Selected papers

Hirt and Nichols (1981), Scardovelli and Zaleski (1999), Sussman and Puckett (2000), Pilliod and Puckett (2004), Kleefsman et al. (2004, 2005), Lin (2005), Hieu and Tanimoto (2006), Duz et al. (2016).

#### Theory

Used in Eulerian representations, a function  $F$  is defined whose value is unity at any point occupied by fluid and zero otherwise. In two dimensions, the time dependence of  $F$  is governed by

$$\frac{\partial F}{\partial t} + u \frac{\partial F}{\partial x} + v \frac{\partial F}{\partial y} = 0. \quad (\text{C.23})$$

The normal direction to the boundary lies in the direction in which the value of  $F$  changes most rapidly so, when the normal direction and value of  $F$  in a boundary cell are known, a line cutting the cell can be constructed that approximates the interface there. A free surface cell is defined as having a non-zero value of  $F$  and having at least one neighbouring cell with a zero value of  $F$ . This is shown in Figure C.3. When (C.23) is integrated over a computational cell, the changes in  $F$  in a cell reduce to fluxes of  $F$  across the cell faces. In Hirt and Nichols (1981)'s initial method to preserve the sharp definition of free surfaces, information about  $F$  downstream as well as upstream of a flux boundary are used to establish a crude interface shape, which is then used to compute the flux. This is called a donor-acceptor flux approximation. Kleefsman et al. (2004, 2005) improved this by using a combination of conservation of mass in surface cells and extrapolation from the direction of the fluid.

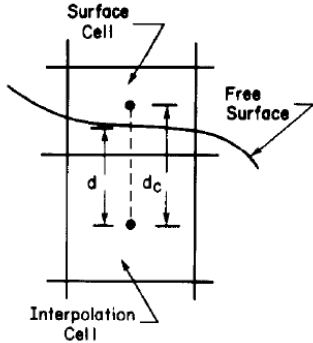


**Figure C.3:** Definition of quantities used in defining free surface pressure boundary condition (Hirt and Nichols (1981)).

### Advantages

- Preserve mass as a direct consequence of the development of an advection algorithm based on a discrete representation of the conservation law<sup>3</sup>.
- Can model breakup/reconnection of the free surface.
- Relatively simple to extend from 2D to 3D.

### Disadvantages

- Reconstruction of the free surface from volume fractions is not simple.
- Curvature of the free surface is difficult to calculate.

## C.2.2 Level-set

**Note:** the level set of a differentiable function  $f$  is defined as the set of points where the function takes on a given constant value. For example, the level set of the function  $f(x, y, z) = x^2 + y^2 + z^2$  corresponding to the value  $c$  is the sphere  $x^2 + y^2 + z^2 = c$  located at  $(0, 0, 0)$  and with radius  $\sqrt{c}$ .

### Selected papers

Osher and Sethian (1988), Rouy and Tourin (1992), Sussman et al. (1994), Sussman and Fatemi (1999), Sussman et al. (1999), Sussman and Puckett (2000), Sethian and Smereka (2003).

### Theory

The interface between two phases is not explicitly tracked, but implicitly "captured" by being identified as the zero level set of a smooth function  $\phi$ . The front location never has to be computed: it is embedded as a particular level set in a fixed domain PDE. In Bihs et al. (2016), the level set function is defined as

$$\phi(\vec{x}, t) = \begin{cases} > 0 & \text{if } \vec{x} \in \text{phase 1} \\ = 0 & \text{if } \vec{x} \in \Gamma \\ < 0 & \text{if } \vec{x} \in \text{phase 2} \end{cases} \quad (\text{C.24})$$

---

<sup>3</sup>see Scardovelli & Zaleski 1999

where  $\Gamma$  is the free surface. The interface can then be moved under an externally generated velocity field by solving the convection equation

$$\frac{\partial \phi}{\partial t} + u_j \frac{\partial \phi}{\partial x_j} = 0. \quad (\text{C.25})$$

To ensure that  $\phi$  remains a signed distance function (i.e.  $|\nabla \phi| = 1$ ), it is reinitialized after each time step. The reinitialization procedure is defined in Rouy and Tourin (1992) and shown in Sussman et al. (1994).

### Advantages

- Explicit location of phase interfaces does not have to be calculated.
- Does not add numerical diffusion.

### Disadvantages

- Formally second-order accurate (see Sussman et al. (1994)).
- Requires reinitialization of level set function after each time step (at approximately  $O(N \log N)$  cost) to stop accumulation of errors (see Sussman and Fatemi (1999)).
- Mass conservation is not formally ensured (see Sethian and Smereka (2003)).

### C.2.3 CIP (Constrained Interpolation Profile)

#### Selected papers

Takewaki et al. (1985), Takewaki and Yabe (1987), Yabe et al. (2001), Sato and Niceno (2012).

#### Theory

A general multiphase solver that is a kind of semi-Lagrangian scheme using a primitive Euler representation. Originally used cubic polynomials, but now uses arbitrary order polynomials to improve mass conservation. The basic idea is that, for a given value  $f$ , the advection equation of  $f$  and the advection equation of its spatial gradient  $q_i = \partial f / \partial x_i$  are calculated by a constrained polynomial interpolation method.

### Advantages

- Low numerical diffusivity.
- Newest version guarantees mass conservation even in the framework of a semi-Lagrangian scheme.
- Subcell resolution of solution.

### Disadvantages

- Interface thickness is not controlled, so there is smearing.
- Requires an interface tracking or sharpening technique (corresponding to the reconstruction in the VOF method).

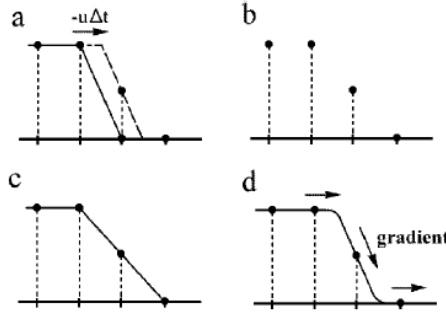


**Figure C.4:** The principle of the CIP method. (a) The solid line is the initial profile and the dashed line is an exact solution after advection, shown in (b) as discretized points. (c) When (b) is linearly interpolated, numerical diffusion appears. (d) In the CIP, the spartial derivative also propagates and the profile inside a grid cell is retrieved (Yabe et al. (2001)).

#### C.2.4 Marker-and-Cell

##### Selected papers

Harlow and Welch (1965), Chan and Street (1970), Park et al. (1999, 2001, 2003)

##### Theory

Uses a distribution of marker particles to define fluid regions, and (originally) sets free surface pressures at the centers of cells defined to contain the surface. To prevent numerical instability, the free surface pressure boundary condition is modified so it is satisfied exactly at the free surface. Used in conjunction with the Navier-Stokes equations; the markers are time-stepped by using local velocities.

##### Advantages

- Allows overturning waves.

##### Disadvantages

- Cells involving markers need complicated treatment.

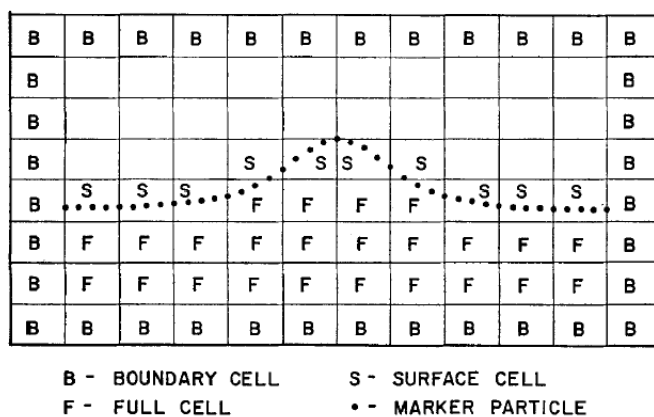


**Figure C.5:** The Marker-and-Cell setup Chan and Street (1970).

### C.2.5 Mixed Eulerian Lagrangian method

#### Selected papers

Longuet-Higgins and Cokelet (1976), Dommermuth and Yue (1987), Kashiwagi (1996, 1998, 2000), Xue et al. (2001); Liu et al. (2001), Harris et al. (2014), Engsig-Karup et al. (2017); Sanchez et al. (2018).

#### Theory

Based on the assumption that, up to the point of breaking, the diffusion of vorticity into the interior of a free surface flow may be quite slow, and so it is a good approximation to neglect viscosity and assume the motion irrotational. Within a closed boundary the velocity potential is therefore determined by its value on the boundary itself, and the time evolution of the flow is uniquely determined by the pressure applied at the moving surface (through Bernoulli's equation). The MEL method then expresses the kinematic and dynamic free surface boundary conditions in terms of the rates of change of the velocity potential  $\phi$  and of the coordinates following a fixed particle

$$\frac{D\mathbf{x}}{Dt} = \nabla\phi, \quad \text{in } \Omega \quad (\text{C.26})$$

$$\frac{D\eta}{Dt} = w, \quad \text{on } \Gamma \quad (\text{C.27})$$

$$\frac{D\phi}{Dt} = \frac{1}{2}\nabla\phi \cdot \nabla\phi - gz - p, \quad \text{on } \Gamma \quad (\text{C.28})$$

where  $w$  is the vertical velocity at the free surface, and  $\Gamma$  denotes the free surface. The material derivative connects the Eulerian and Lagrangian reference frames through

$$\frac{D}{Dt} = \frac{\partial}{\partial t} + \mathbf{V} \cdot \nabla, \quad (\text{C.29})$$

where  $\mathbf{V}$  is a velocity vector for the moving frame of reference that can be chosen arbitrarily. If  $\mathbf{V} = 0$  we obtain an Eulerian frame of reference and if  $\mathbf{V} = \nabla\phi$  we obtain a Lagrangian frame of reference Engsig-Karup et al. (2017).

#### Advantages

- Allows large deformations of the free surface (up to the point of reconnection of the overturning surface).

#### Disadvantages

- Free surface points can enter/exit an immersed body arbitrarily; an additional constraint is required such that fluid particles move tangentially along the body boundary.
- Free surface points tend to cluster in regions of high flow gradients, requiring regridding to avoid a break down in simulations (see Liu et al. (2001); Dommermuth and Yue (1987)).

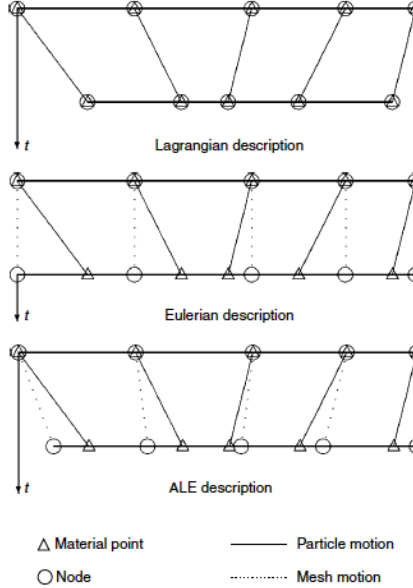


**Figure C.6:** One-dimensional example of Lagrangian, Eulerian and ALE mesh and particle motion Donea et al. (2004).

### C.2.6 Arbitrary Lagrangian Eulerian method

#### Selected papers

Hughes et al. (1981), Casadei and Halleux (1995), Hirt et al. (1997), Soulaimani and Saad (1998), Braess and Wriggers (2000), Souli and Zolesio (2001), Casadei et al. (2001), Duarte et al. (2004), Donea et al. (2004), Decoene and Gerbeau (2008), Wu et al. (2013), Zhang and Kashiwagi (2017a,b).

#### Theory

Unlike the pure Lagrangian and Eulerian descriptions, ALE allows the computational domain to be animated with its proper motion; it is possible to track the (large) free boundary motion while maintaining a fairly regular (i.e. well-resolved) mesh. Three frames are introduced: a material frame (Lagrangian; following the particles; can be thought of as the domain occupied at time  $t = 0$  by the material particles which occupy the spatial domain at time  $t$ ), a spatial frame (Eulerian; this is the domain on which the fluid problem is posed; is generally in motion due to moving boundaries), and a time-independent reference frame. The pure Eulerian description is therefore obtained when the spatial domain coincides with the reference domain, and the pure Lagrangian description is obtained when the material domain coincides with the reference domain. The fundamental ALE relation between material time derivatives, referential time derivatives, and spatial gradient can be expressed as (Donea et al. (2004))

$$\frac{\partial f}{\partial t}|_X = \frac{\partial f}{\partial t}|_\chi + \frac{\partial f}{\partial x} \cdot c = \frac{\partial f}{\partial t}|_\chi + c \cdot \nabla f, \quad (\text{C.30})$$

and shows that the time derivative of the physical quantity  $f$  for a given particle  $X$ , that is, its material derivative, is its local derivative (with the reference coordinate  $\chi$  held fixed) plus a convective term taking into account the relative velocity  $c$  between the material and the mesh (i.e.

$c = v - v^{\text{mesh}}$ ). The choice of  $v^{\text{mesh}}$  constitutes one of the major problems of the ALE description. Souli and Zolesio (2001) propose a set of PDEs to govern the displacement field of the mesh, with appropriate boundary conditions: *fixed boundary conditions* where the mesh displacement is zero; *moving boundary conditions* where the mesh displacement is prescribed; *free surface boundary conditions* where the normal mesh velocity at the free surface is set equal to the normal fluid velocity ( $(v - v^{\text{mesh}} \cdot \vec{n}) = 0$ ). In the fluid the divergence of the mesh displacement field is set to zero. This method can work for prescribed (i.e. forced) motion of boundaries, but not free motion.

### Advantages

- The free surface can be precisely tracked without necessarily remeshing, thereby avoiding the projection errors inherent to remeshing and saving computational time.

### Disadvantages

- Governing equations are more complex to account for the moving velocities of the meshes (i.e. we now have to solve both fluid and mesh equations).
- Surface-piercing structures require some sort of sliding treatment of boundary points, which can adjust their position according to the body geometry. Zhang and Kashiwagi (2017a,b) suggest implementing curved paths analogous to the body's local geometry.

## C.2.7 Quasi Arbitrary Lagrangian Eulerian method

### Selected papers

Ma and Yan (2006); Yan and Ma (2007a); Ma and Yan (2009a).

### Theory

Similar to the ALE approach, the main idea is that the complex mesh is generated only once and is subsequently moved to conform to the motions of the free surface and structure surface. An important point is that the velocities of the moving mesh do not need to be considered in the governing equations. Instead, the spring analogy method is used, where the nodes in a mesh are considered to be connected by springs (Batina (1989)). The whole mesh is then deformed like a spring system. Nodal displacements are determined by

$$\Delta \vec{r}_i = \sum_{j=1}^{N_i} k_{ij} \Delta \vec{r}_j / \sum_{j=1}^{N_i} k_{ij}, \quad (\text{C.31})$$

where  $\Delta \vec{r}_i$  is the displacement at node  $I$ ,  $k_{ij}$  is the spring stiffness, and  $N_i$  is the number of nodes that are connected with node  $I$ . This can be interpreted such that the resultant spring forces acting on node  $I$  by all springs remain zero after all nodes are displaced. The value of the spring stiffness is usually chosen to be inversely proportional to the distance between two nodes; Ma and Yan (2006) originally choose

$$k_{ij} = \frac{1}{l_{ij}^2} e^{\gamma[1+(z_i+z_j)/2d]}, \quad (\text{C.32})$$

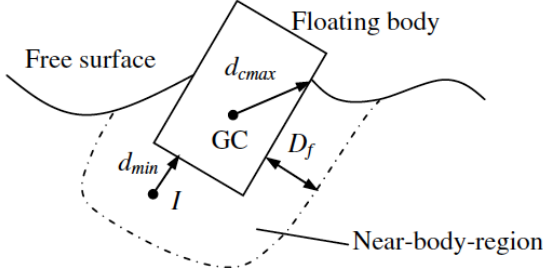


**Figure C.7:** Region near floating body (GC: gravitational centre), Yan and Ma (2007a).

where  $l_{ij}$  is the distance between nodes  $I$  and  $J$ ,  $z_i$  and  $z_j$  are the vertical coordinates of nodes  $I$  and  $J$ ,  $d$  is the water depth and  $\gamma$  is a coefficient that should be assigned a larger value if springs are required to be stiffer at the free surface. To include freely floating bodies this spring stiffness is replaced by Yan and Ma (2007a)

$$k_{ij} = \frac{1}{l_{ij}^2} e^{\gamma_f [1 + (z_i + z_j)/2d]} e^{\gamma_b (\hat{w}_i + \hat{w}_j)/2}, \quad (\text{C.33})$$

where  $\gamma_f$  is the same as  $\gamma$  previously, and  $\gamma_b$  plays the same role as  $\gamma_f$  but is used to adjust the spring stiffness near the body surface. Both are again considered constant ( $\gamma_f = \gamma_b = 1.7$ ). Finally  $\hat{w}$  is a weight function defined by

$$\hat{w} = \begin{cases} 0, & d_f > D_f, \\ 1 - d_f/D_f, & d_f \leq D_f, \end{cases} \quad (\text{C.34})$$

where  $d_f$  is the minimum distance from the node concerned to the body surface as shown in Figure C.7;  $D_f$  is the distance between the body surface and the boundary of the near-body-region, defined as  $D_f = \varepsilon d_{c\max}$ , where  $d_{c\max}$  is the maximum distance from the gravitational centre to the wetted body surface and depends on the relative position of the floating body to the free surface. They suggest  $\varepsilon = 1.5$ . For 3D applications the spring stiffness is further updated, this time by evaluating  $\gamma_b$  by a weight function, and an additional factor is included to govern the quality index of elements close to the body (see Yan (2006); Lewis et al. (1996)).

Special care must be taken with nodes on the free surface to avoid excessive clustering/spreading; Ma and Yan (2006) suggest relocating at some time steps (e.g. every 40 time steps), where free surface nodes are grouped into those on curved waterlines and those not on waterlines (but still on the free surface). Waterline nodes are redistributed by requiring that the weighted arc-segment lengths between successive nodes are constant; i.e.  $\bar{w}_i \Delta s_i = C_s$ . The spring analogy is used for the remaining free surface nodes. To ensure that they remain on the free surface, the  $x$  and  $y$  values are calculated by the spring analogy, and  $z$  is calculated by interpolation. Two interpolating methods are suggested: find which element each new node belongs to by using the coordinate  $x$  and  $y$  of the new nodes and then estimate the values of  $z$  using the shape function defined on this element; or use Moving Least Squares (MLS, see Atluri and Zhu (1998)), where  $z$  is determined using the information at a group of old nodes in such a way that the error is minimized. Ma and Yan (2006) use the latter due to its accuracy, despite a higher computational cost.

**Advantages**

- No remeshing.
- Velocities of moving mesh do not need to be considered in the governing equations.
- Complex geometries can be modelled.

**Disadvantages**

- Redistribution of waterline nodes (i.e. body-free surface intersections) is required occasionally, with associated computational cost and possible introduction of error.
- Requires the use of "tuning" parameters  $\gamma, \varepsilon$ .

**DTU Mechanical Engineering**  
**Section of Fluid Mechanics, Coastal and Maritime Engineering**  
Technical University of Denmark

Nils Koppels Allé, Bld. 403  
DK-2800 Kgs. Lyngby  
Denmark  
Tlf.: +45 4525 1360  
Fax: +45 4525 1961

[www.mek.dtu.dk](http://www.mek.dtu.dk)

December 2020

ISBN: 978-87-7475-633-0

**DCAMM**  
**Danish Center for Applied Mathematics  
and Mechanics**

Nils Koppels Allé, Bld. 404  
DK-2800 Kgs. Lyngby  
Denmark  
Phone (+45) 4525 4250  
Fax (+45) 4525 1961

[www.dcamm.dk](http://www.dcamm.dk)

DCAMM Special Report No. S284

ISSN: 0903-1685